Iowa State University
Digital Repository

2016

Evaluation of an optimal aerocapture guidance algorithm for human Mars missions

Kyle Dean Webb
Iowa State University

Evaluation of an optimal aerocapture guidance algorithm for human Mars missions

by

Kyle Webb

A thesis submitted to the graduate faculty

in partial fulfillment of the requirements for the degree of

MASTER OF SCIENCE

Major: Aerospace Engineering

Program of Study Committee:
Ping Lu, Major Professor
Ran Dai
Peng Wei

Iowa State University

Ames, Iowa

2016

DEDICATION

This thesis is dedicated to my family and friends,

without whom none of this would be possible.

Thank you for keeping me going.

TABLE OF CONTENTS

LIST OF FIGURES

LIST OF TABLES

ACKNOWLEDGEMENTS

ABSTRACT

Aeroassist guidance is concerned with providing steering commands to a vehicle flying through a planetary atmosphere in the form of an aerodynamic roll angle, or bank angle, which results in appropriate direction of the aerodynamic lift force so that the vehicle will safely and accurately reach its designated final condition. Aerocapture guidance is a particular subcategory of aeroassist guidance that involves atmospheric entry from an interplanetary transfer orbit, a guided flight through the atmosphere, and a final condition consisting of a post-atmospheric exit target orbit around the planet. Using aerocapture guidance to establish this target orbit can provide significant propellant mass savings when compared to traditional propulsive maneuvers. No current aerocapture guidance algorithms can ensure truly optimal performance in minimizing post-exit orbit insertion ΔV requirements. This thesis investigates the development of a two-phase optimal aerocapture guidance algorithm. This closed-loop guidance algorithm uses a mathematically optimal bang-bang bank angle profile structure, in which a vehicle first flies with the lift vector pointed straight up, and then flies full lift-down until atmospheric exit. The optimal trajectory is found by determining the switching time between full lift-up and full lift-down flight. Results from testing the algorithm in a high-fidelity NASA simulation environment are presented and compared with results from existing state-of-the-art aerocapture guidance algorithms. These results show that the developed algorithm provides the robustness and adaptability of a numerical predictor-corrector guidance algorithm while demonstrating a significant reduction in ΔV requirements compared to other existing algorithms.

CHAPTER 1. INTRODUCTION

This Chapter provides a definition of the aerocapture guidance problem and the specific challenges it entails. Section 1.2 provides an overview of what has been accomplished in the field to date, while Section 1.3 will compare and contrast the Fully Numerical Predictor-Corrector Aerocapture Guidance algorithm with current approaches. Finally, Section 1.4 delves into the particular accomplishments that will be presented in this thesis.

1.1 Problem Definition and Challenges

Aeroassist guidance is concerned with providing steering commands to a vehicle flying through a planetary atmosphere in the form of an aerodynamic roll angle, or bank angle, which results in appropriate direction of the aerodynamic lift force so that the vehicle will safely and accurately reach its designated final condition. Aerocapture guidance is a particular subcategory of aeroassist guidance that involves atmospheric entry from an interplanetary transfer orbit, a guided flight through the atmosphere, and a final condition consisting of a post-atmospheric exit target orbit around the planet [1]. Using propulsive maneuvers to slow down a spacecraft on an interplanetary orbital transfer requires a large amount of propellant to achieve the desired final condition. This propellant mass requirement can be significantly reduced by entering the atmosphere of the planet and dissipating energy through friction [2].

A major limiting factor in carrying out an interplanetary mission is the mass of the deliverable payload. Because the vast majority of the mass of a rocket is comprised of

propellant, the deliverable mass is relatively small. Any reduction in the propellant needed to insert a spacecraft into its desired post-exit orbit will lead to reduced fuel costs and an increase in payload capacity, allowing for more data-gathering instruments to be included in the mission. The key to reducing these propellant costs and thereby maximizing the available payload mass is minimizing the required ΔV budget to successfully establish the desired final orbit.

The logistical challenges of planning and executing a human mission to Mars are especially unique. Current plans call for a landed mass between 20 and 60 metric tons. Slowing a vehicle of this size enough to allow for a safe atmospheric entry, descent, and landing by using traditional propulsive methods would require an extremely large propellant mass. Because of this, aerocapture guidance is being strongly considered as an alternative to a purely propulsive braking maneuver by NASA's Evolvable Mars Campaign to allow for significant fuel savings and additional room for other mission-critical scientific payloads [3].

1.2 Aerocapture Guidance Algorithm History

The idea of using the atmosphere of a planet or other celestial body to reach a final orbit around that body as an alternative to a traditional propulsive maneuver was proposed as early as 1961 [4]. However, developing a reliable, high-performance aerocapture guidance routine is quite difficult. Because of this difficulty, the implementation of this idea into a usable guidance algorithm began a few years later, starting in the early 1980s [5]. One of the first attempts at developing an aerocapture guidance algorithm was carried out by Hill in 1983 [6]. This algorithm was based on the Apollo skip-entry guidance

routine [7]. The Apollo logic was adapted such that instead of targeting a specific atmospheric-exit condition to allow a brief exit followed by a re-entry, the algorithm would command a specific exit condition to reach a desired orbital condition with a trajectory correction burn applied at apoapsis.

In 1985, Cerimele and Gamble proposed a more advanced two-phase hybrid lifting aeroassist guidance algorithm, using a combination of reference trajectory tracking and a predictor-corrector routine [8]. The first phase, known as the "equilibrium glide" phase, modulates the bank angle to maintain equilibrium glide until shortly after the vehicle reaches its periapsis. The second phase, called the "exit phase," uses a predictor-corrector scheme to hold a constant altitude rate in order to reach the desired condition at atmospheric exit. In addition to the hybrid longitudinal logic, the algorithm also implemented a lateral logic based on a velocity-dependent deadband to manage inclination error at atmospheric exit. This algorithm later became known as the Hybrid Predictor-corrector Aerocapture Scheme, and has been used in multiple trade studies for aerocapture missions [9].

Additional algorithms have been developed building off of the success of HYPAS. In 1998, Bryant, Tigges, and Ives suggested a HYPAS-derived approach using analytical drag control instead of reference dynamic pressure during the equilibrium glide phase [10]. Unlike HYPAS, this method used online computation of drag reference profiles, allowing for a reduction in pre-flight tuning requirements. In 2008, Casoliva, Lyons, Wolf, and Mease combined the drag profile tracking of the equilibrium glide phase with an online reference trajectory generator based on a numerical predictor-corrector for use in gravity assists [11].

Because of their high computational demands, numerical predictor-corrector algorithms did not see extensive use until the last few decades. Because they are frequently updated based on the current state throughout the trajectory, these algorithms tend to provide high degrees of accuracy and adaptability to any dispersions. One of the first numerical predictor-corrector algorithms was developed in 1992 by Braun and Powell [12]. This algorithm used a predictor-corrector to provide bank angle commands for use in aerobraking, and demonstrated superior performance to other approaches [13]. In 2003, a numerical predictor-corrector algorithm was developed by Jits and Walberg for use in Mars aerocapture missions [14]. Both of these algorithms prescribe a constant bank angle magnitude to reach a desired apoapsis altitude after exiting the atmosphere.

All of the above aerocapture guidance algorithms are formulated based on the idea of minimizing post-exit apoapsis altitude errors and performing a single periapsis raise burn to establish a final orbit. In recent years, approaches based explicitly on minimizing post-exit propellant consumption have gained popularity. In 2011, Lafleur suggested that a numerical predictor-corrector algorithm could be used to minimize the sum of two post-exit trajectory correction burns, one performed at an unrestricted apoapsis to raise the periapsis altitude, and a second performed at the new periapsis to establish the final orbit, as seen in Fig. 1.1. This new approach was implemented in an aerocapture algorithm called PredGuid+A. PredGuid+A was adapted from a previously developed numerical predictor algorithm known as PredGuid, which was created for use in skip entry guidance [15].
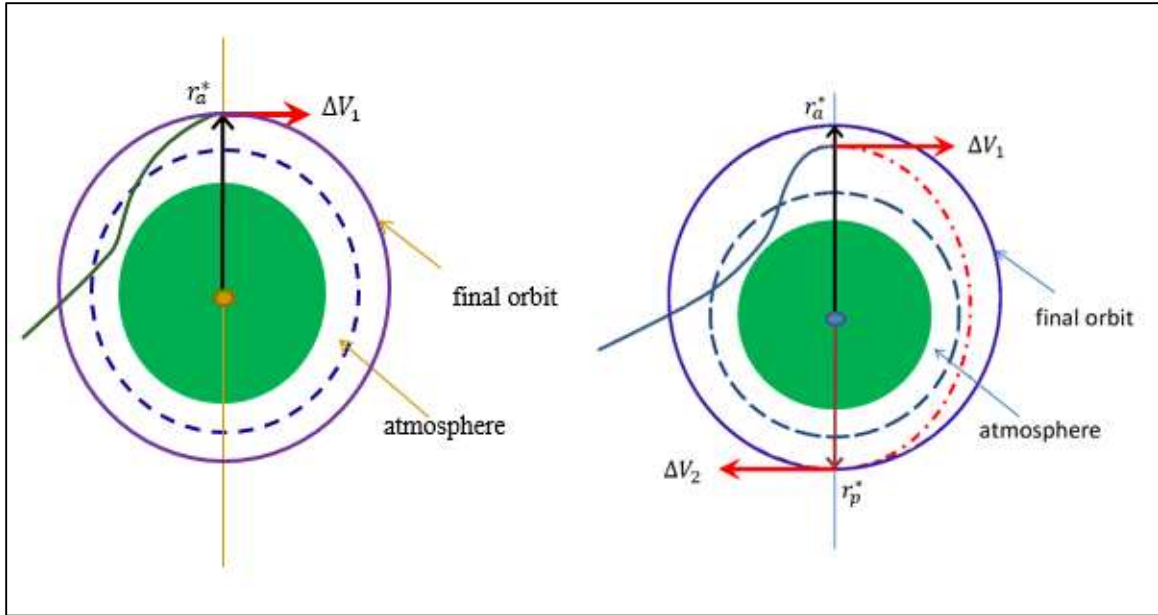
Fig. 1.1. One-burn vs. two-burn aerocapture approaches.

Like the numerical predictor-corrector aerocapture algorithms developed before it, PredGuid+A attempts to find a constant bank angle profile to reach a desired target condition. However, this algorithm allows a user to select between two guidance modes: one that targets a post-exit apoapsis altitude and uses a single burn to establish a final orbit, and one that attempts to minimize the two-burn ΔV requirement, with no explicit post-exit apoapsis altitude constraint. This second mode has been shown to provide significant minimization in propellant consumption for certain trajectories [16].

1.3 Fully Numerical Predictor-Corrector Aerocapture Guidance

The Fully Numerical Predictor-Corrector Aerocapture Guidance algorithm, also known as the FNPAG algorithm, is the focus of this thesis. The framework of this algorithm was created by Lu in 2014 [1]. As shown in Section 1.2, a number of algorithms have been developed that implement numerical predictor-corrector guidance to find a

suitable aerocapture trajectory. However, the FNPAG algorithm differs from existing algorithms by using a novel approach: a formulation that is rooted in the principles of the optimal control theory, and that does not necessarily prescribe a constant bank angle profile.

None of the aerocapture guidance algorithms in existence today explicitly attempt to achieve the best performance in minimizing the post-atmospheric-exit ΔV dictated by the optimal control theory. The optimal aerocapture guidance problem deals with highly sensitive, nonlinear control. Because of this, any brute-force numerical approaches to finding a solution are unlikely to reach the levels of robustness and efficiency required for implementation in an aerocapture guidance algorithm. As a result of its basis in optimal control, the FNPAG algorithm allows for reliable optimal solutions to nonlinear, constrained control problems.

Another significant advantage of the FNPAG algorithm is its applicability to any range of vehicle configurations and lifting capabilities, as well as a variety of different missions from atmospheric entry to aerocapture. In addition, FNPAG requires little to no tuning between missions and vehicles, allowing for quick and easy assessment of vehicles and mission requirements. Because of this, FNPAG is ideal for performing trade studies. For more information on the formulation of the FNPAG algorithm, refer to Chapter 3 of this thesis.

1.4 Thesis Achievements

Significant strides have been made in the development of the FNPAG algorithm, and will be presented as the main topics of discussion for this thesis. The first major

accomplishment was the implementation of the algorithm in an in-house three-degree-of-freedom (3-DOF) simulation. This simulation included inputs for vehicle parameters, the initial conditions, and the final target orbit conditions. Additional capabilities were added for dispersed test cases used in Monte Carlo simulations, allowing for user-defined dispersions in the initial conditions, the vehicle characteristics such as vehicle mass, and atmospheric uncertainties. Modeling of atmospheric dispersions was accomplished by implementing Mars GRAM 2010 code. Thorough testing of the in-house simulation environment was conducted for multiple vehicles, with promising results.

The second major accomplishment took place during a Visiting Technology Experience at NASA Langley Research Center. The FNPAG algorithm was integrated into a 3-DOF simulation using the Program to Optimize Simulated Trajectories II, a high-fidelity environment developed by NASA Langley. The algorithm was tuned and tested for three different vehicles: a Hypersonic Inflatable Aerodynamic Decelerator, the Adaptable, Deployable Entry Placement Technology, and a rigid aeroshell with a moderate lift-to-drag ratio. More information on these vehicles can be found in Chapter 2. Two target orbits, a 1-sol and 5-sol polar orbit, were considered in the testing. The simulation environment, target conditions, and Monte Carlo dispersions will be further discussed in Chapter 4. Results from these simulations were compared with results from a NASA Langley-developed terminal point controller algorithm for the HIAD vehicle and a 1-sol target orbit, where the FNPAG algorithm displayed superior performance in terms of ΔV minimization. These results will be thoroughly analyzed in Chapter 5.

CHAPTER 2. AEROCAPTURE GUIDANCE PROBLEM

This Chapter introduces the formulation of the aerocapture guidance problem, in which a vehicle with a given set of initial conditions flies through the atmosphere of a celestial object such that it reaches a desired post-atmospheric-exit target orbit. Section 2.1 describes the equations of motion used in defining the aerocapture guidance problem, while Section 2.2 introduces the methods used to model planetary atmospheres. Section 2.3 contains a brief description of each of the vehicle models used in testing the aerocapture guidance algorithm and their different properties.

2.1 Equations of Motion

Because most celestial bodies are not perfectly spherical, we begin the problem formulation by defining the three-dimensional equations of motion of a vehicle flying through the atmosphere of an ellipsoidal rotating planet, given by Eqs. (2.1-2.6) [1]:

$$\dot{r} = V \sin \gamma \tag{2.1}$$

$$\dot{\theta} = \frac{V \cos \gamma \sin \psi}{r \cos \Phi} \tag{2.2}$$

$$\dot{\Phi} = \frac{V \cos \gamma \cos \psi}{r} \tag{2.3}$$

$$\begin{aligned}
\dot{V} = \; &-D - g_r \sin \gamma - g_\Phi \cos \gamma \cos \psi \\
&+ \Omega^2 r \cos \Phi \; (\sin \gamma \cos \Phi - \cos \gamma \sin \Phi \cos \psi)
\end{aligned} \tag{2.4}$$

$$\begin{aligned}
\dot{\gamma} = \frac{1}{V} \big[&L \cos \sigma + (V^2/r - g_r) \cos \gamma + g_\Phi \sin \gamma \cos \psi \\
&+ 2\, \Omega V \cos \Phi \sin \psi \\
&+ \Omega^2 r \cos \Phi \; (\cos \gamma \cos \Phi + \sin \gamma \cos \psi \sin \Phi) \big]
\end{aligned} \tag{2.5}$$

$$\dot{\psi} = \frac{1}{V}[\frac{L\sin\sigma}{\cos\gamma} + \frac{V^2}{r}\cos\gamma\sin\psi\tan\Phi + g_\Phi\frac{\sin\psi}{\cos\gamma}$$
$$- 2\Omega V(\tan\gamma\cos\psi\cos\Phi - \sin\Phi)$$
$$+ \frac{\Omega^2 r}{\cos\gamma}\sin\psi\sin\Phi\cos\Phi] \qquad (2.6)$$

where r is the radial distance from the center of the celestial body to the spacecraft, θ and

Φ are the longitude and geocentric latitude, respectively, V is the planet-relative velocity,

γ is the flight-path angle of the planet-relative velocity vector, ψ is the heading angle of

the planet-relative velocity vector, measured clockwise in the horizontal plane from the

north, Ω is the celestial body's rotation rate, and σ is the bank angle, defined as the

rotation angle of the spacecraft about the relative velocity vector, with a positive bank

angle occurring when the right wing is angled downward. It should be noted that the

bank angle is not the same as the body roll angle if the angle of attack is nonzero.

Here, L and D are defined as the aerodynamic lift and drag accelerations and

depend on the lift and drag coefficients C_L and C_d, respectively, which depend on the

angle of attack. For aerocapture, the angle of attack profile is usually defined as a

function of the Mach number, and the trim angle-of-attack profile is often used. In this

case, the inertial velocity vector of the vehicle is given as

$$\boldsymbol{V}_i = \boldsymbol{V}_r + \boldsymbol{\Omega} \times \boldsymbol{r} \qquad (2.7)$$

where $\boldsymbol{V}_r$ is the planet-relative velocity vector and $\boldsymbol{r}$ and $\boldsymbol{\Omega}$ are the position vector of the

vehicle and the planet's rotation rate, respectively, in a Cartesian coordinate frame.

Because the celestial body is not spherical, we must also account for the gravitational acceleration components in the radial and latitudinal directions, g_r and g_Φ, respectively. When only considering J_2 effects, these values are defined as

$$g_r = \frac{\mu}{r^2}\left[1 + J_2\left(\frac{R_0}{r}\right)^2(1.5 - 4.5\,sin^2\Phi)\right] \tag{2.8}$$

$$g_\Phi = \frac{\mu}{r^2}\left[J_2\left(\frac{R_0}{r}\right)^2(3\sin\Phi\cos\Phi)\right] \tag{2.9}$$

where μ is the gravitational parameter of the body and R_0 is its equatorial radius.

2.1.1 Apoapsis-targeting problem

We continue formulating the aerocapture guidance problem with a discussion on two specific problems regarding aerocapture, the first of which is known as the apoapsis-targeting problem. For this problem, given a set of initial conditions at the initial time t_0, a bank angle profile is desired to be found such that the vehicle flies a trajectory that reaches a user-defined post-atmospheric-exit apoapsis radius, denoted by r_a^*. This targeting condition is defined as follows:

$$r_a(r_{exit}, V_{exit}, \gamma_{exit}) - r_a^* = 0 \tag{2.10}$$

where r_a is the apoapsis radius determined by r_{exit}, V_{exit}, and γ_{exit}, the radius, inertial velocity, and flight-path angle at the atmospheric exit interface, respectively. Using two-body orbital mechanics, we can solve for r_a:

$$r_a = a\left(1 + \sqrt{1 - \frac{V_{exit}^2 r_{exit}^2 cos^2(\gamma_{exit})}{\mu a}}\right) \tag{2.11}$$

where a is the semi-major axis of the post-atmospheric-exit orbit, given by

$$a = \frac{\mu}{2\mu/r_{exit} - V_{exit}^2} \tag{2.12}$$

The solution to this problem is called the apoapsis-targeting solution [1]. However, in addition to prescribing the post-exit apoapsis radius, it is often desired to meet user-defined criteria on the orientation of the orbit. This is generally accomplished in one of two ways. The first method involves only targeting a desired orbital inclination:

$$i\left(\boldsymbol{x}(t_f)\right) - i^* = 0 \tag{2.13}$$

where i^* is the targeted inclination of the final orbit, i is the orbital plane at atmospheric exit, and $\boldsymbol{x} = [r\ \theta\ \Phi\ V\ \gamma\ \psi]^T$ is the state vector of the trajectory dynamics given in Eqs. (1-6) at t_f, the time at atmospheric exit. The second method is more complex, and involves minimizing the wedge angle of the final orbit, defined as follows [17]:

$$\boldsymbol{i'} = cos^{-1}[\cos(\Omega - \Omega^*)\sin(i)\sin(i^*) + \cos(i)\cos(i^*) \tag{2.14}$$

where $\boldsymbol{i'}$ is the wedge angle, Ω is the longitude of ascending node of the orbital plane at atmospheric exit, and Ω^* is the targeted longitude of ascending node of the final orbit. These constraints will be discussed in further detail in the following chapters because they are addressed by a lateral logic that is independent of the main aerocapture guidance logic.

2.1.2 Optimal aerocapture problem

The apoapsis-targeting problem has a potentially infinite number of feasible solutions depending on the difficulty of reaching the user-defined post-atmospheric-exit target orbit. However, only one of these solutions will also minimize the required propellant consumed by an engine burn to reach the desired target orbit. This particular trajectory is the solution to what is known as the optimal aerocapture problem [1]. The propellant requirement can be approximated by the in-plane impulsive velocity increment ΔV needed to reach the target orbit. This propellant cost, denoted by P_1, can be found using the following equation:

$$P_1 = \Delta V = \sqrt{2\mu}\left(\sqrt{\frac{1}{r_a^*} - \frac{1}{r_a^* + r_p^*}} - \sqrt{\frac{1}{r_a^*} - \frac{1}{2a}}\right) \tag{2.15}$$

where r_p^* is the user-defined periapsis radius of the target orbit.

Additional improvement in terms of reduction of propellant requirement may be obtained by planning for two in-plane impulsive engine burns, ΔV_1 and ΔV_2, respectively. In this case, instead of enforcing the constraint developed in Eq. 2.10, the first burn is applied at the unconstrained post-atmospheric apoapsis r_a to reach the desired final periapsis radius, r_p^*, and then a second burn is conducted at r_p^* to reach the final apoapsis radius r_a^*. We define the post-exit periapsis radius r_p before the first burn as follows:

$$r_p = a\left(1 - \sqrt{1 - \frac{V_{exit}^2 r_{exit}^2 \cos^2(\gamma_{exit})}{\mu a}}\right) \tag{2.16}$$

It then follows that the propellant cost to be minimized, in this case denoted by P_2, can be represented as

$$P_2 = |\Delta V_1| + |\Delta V_2|$$

$$= \sqrt{2\mu}\left(\left|\sqrt{\frac{1}{r_a} - \frac{1}{r_a + r_p^*}} - \sqrt{\frac{1}{r_a} - \frac{1}{2a}}\right|\right.$$

$$\left. + \left|\sqrt{\frac{1}{r_p^*} - \frac{1}{r_a^* + r_p^*}} - \sqrt{\frac{1}{r_p^*} - \frac{1}{r_a + r_p^*}}\right|\right) \quad (2.17)$$

The solution to the aerocapture guidance problem involves finding the bank angle σ on-board for every call to the guidance algorithm to ensure that the vehicle achieves the user-defined target orbit established by the constraints given in Eq. (2.10), while simultaneously minimizing the lateral targeting errors given by either Eq. (2.13) or Eq. (2.14). This clearly requires a closed-loop guidance algorithm. Finding a feasible apoapsis-targeting solution for every guidance cycle is the basis of the Fully Numerical Predictor Corrector Aerocapture Guidance algorithm. However, the algorithm takes this solution one step further by determining the optimal apoapsis-targeting solution to minimize the cost function formulated in Eq. (2.15). In the case of a two-burn trajectory, FNPAG will find the optimal bank-angle profile to minimize Eq. (2.17). The methodology behind finding these solutions will be further explained in Chapter 3.

2.2 Atmospheric Models

The accuracy of any aerocapture algorithm can be greatly affected by dispersions in atmospheric density. This is especially apparent for planets with relatively thin atmospheres, such as Mars, where small errors in predicted and actual atmospheric density can have a huge impact on targeting accuracy. In fact, dispersions due to factors such as wind and atmospheric dust can cause density magnitude dispersions of more than 100%, as shown in Fig. 2.1. Because of this, an accurate atmospheric model for any planet is absolutely necessary. In recent years, NASA's Marshall Spaceflight Center has developed a Global Reference Atmospheric Model (GRAM) for many celestial bodies, including Earth, Mars, and even Saturn's moon Titan [18]. Development and testing of the FNPAG algorithm was carried out for both Earth and Mars using the 2010 version of GRAM. Because the aerocapture flyoff was conducted on Mars, this section will be focused on the features of Mars GRAM.

Mars GRAM 2010 is a Fortran-based tool developed from data gained from the Mars Orbiter Laser Altimeter and using the Mars General Circulation Model [19]. The code allows users to determine the nominal atmospheric density at any point in the atmosphere. Basic inputs to Mars GRAM include the longitude, latitude, and altitude of a vehicle. The user can also specify the levels of atmospheric dust, the areocentric longitude of the Sun from Mars, wind effects, seasonal atmospheric pressure effects, and even the location and intensity of dust storms.
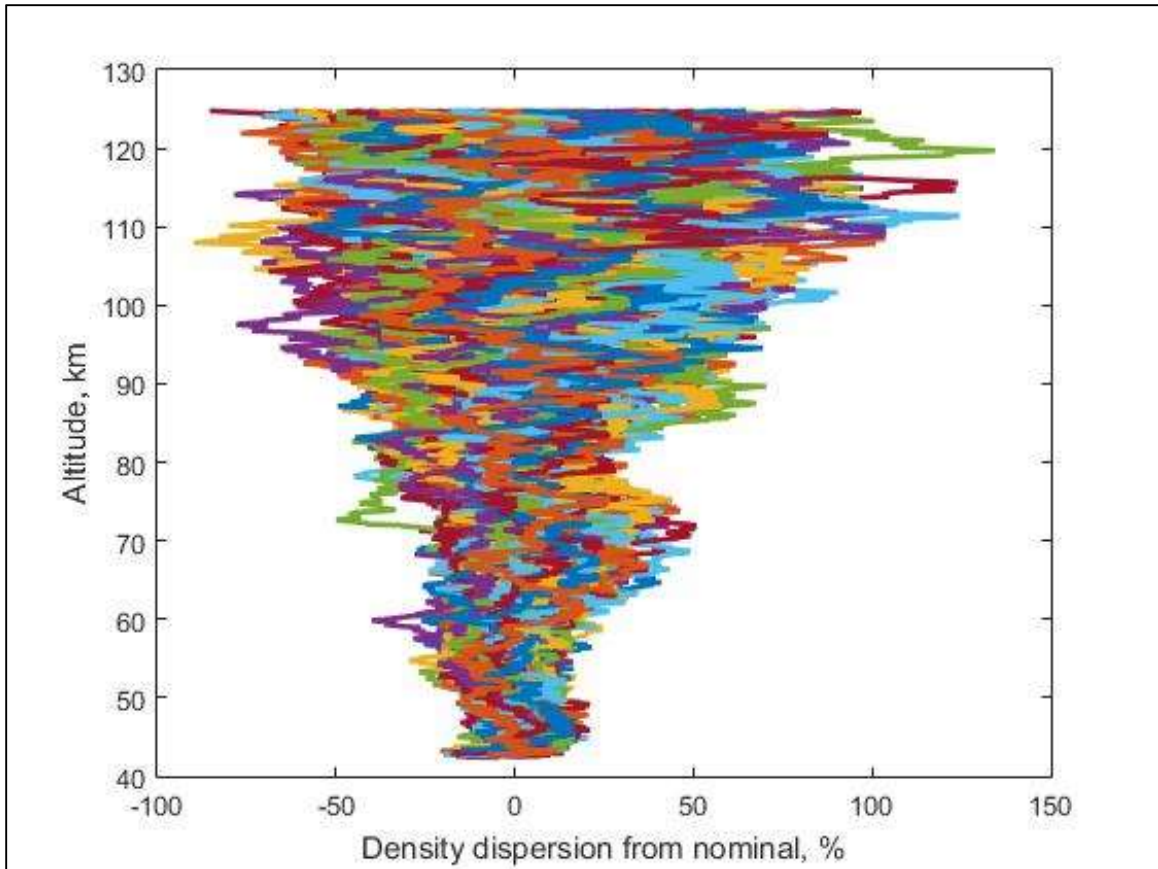
Fig. 2.1. Sample Mars atmospheric density dispersion.

In addition to generating a nominal atmospheric density, Mars GRAM is capable of generating Monte Carlo dispersions based on user-defined scale factors for the density and winds. The effect of the Monte Carlo dispersion generator can be seen in Fig. 2.2, which shows the altitude vs. density profile for 100 dispersed cases, with the nominal density profile shown in red.
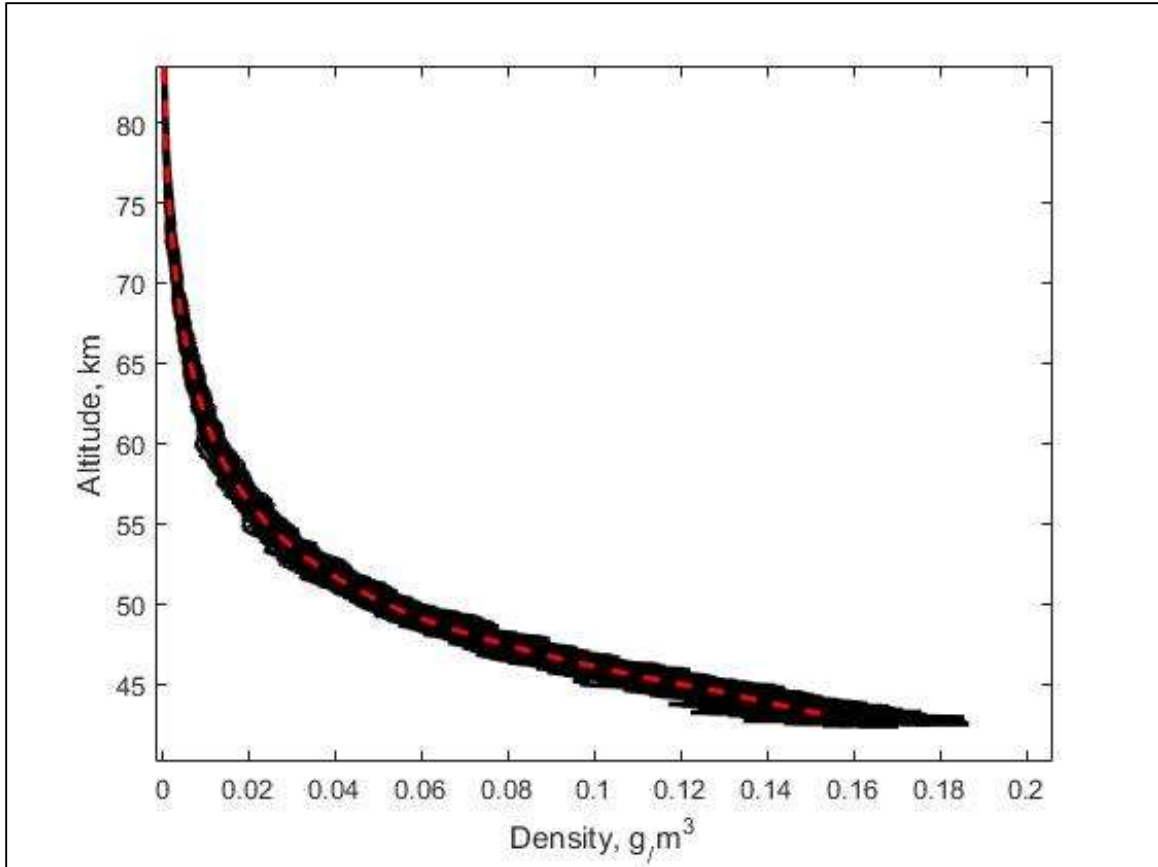
Fig. 2.2. Dispersed Mars GRAM density profiles.

Unlike the atmosphere of Earth, Mars' atmosphere undergoes wild swings in surface pressure as it orbits around the Sun, as seen in Fig 2.3. This is commonly attributed to the condensation and sublimation of carbon dioxide stored in the Martian polar ice caps [20]. This can cause significant changes in the atmospheric density throughout the seasons. In addition, the atmosphere is not uniform, displaying large differences in density at different locations around the planet. For these reasons, it is critical to feed the nominal density at the location and date of the planned mission to an aerocapture algorithm. For the aerocapture guidance flyoff, Mars GRAM was used both inside the algorithm logic and outside in the trajectory model, so this concern was mitigated. However, in the future, a more simplistic atmospheric model will most likely be used in the aerocapture guidance.

A current solution is to develop a curve fit based on the nominal density profile, using a logarithmic scale on the density magnitude. This curve fit should be centered and normalized using a curve fitter such as Matlab's *cftool* suite for best results.
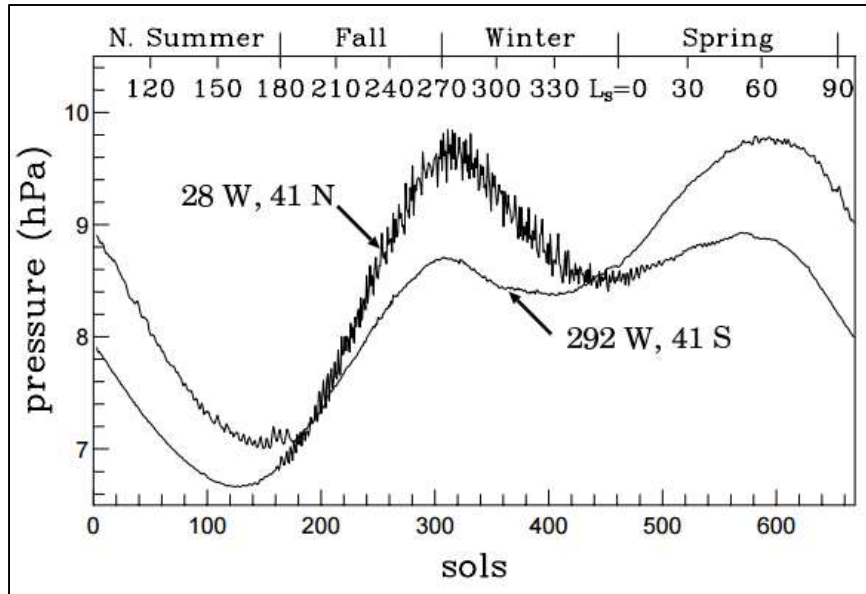
Fig. 2.3. Martian pressure cycle at two surface locations [20].

2.3 Vehicle Models

An advantage unique to the FNPAG algorithm is that it is applicable to a wide variety of spacecraft. FNPAG was specifically designed to work for anything from capsules with an extremely low lift-to-drag ratio to high lift-to-drag experimental hypersonic vehicles, and everything in between. For the aerocapture guidance flyoff, three specific vehicles that are currently being evaluated for NASA's Evolvable Mars Campaign were considered: A low L/D inflatable spacecraft, a slightly higher L/D deployable semi-rigid aeroshell, and a mid L/D rigid aeroshell vehicle.

2.3.1 ADEPT

The first vehicle concept examined was the Adaptable, Deployable Entry Placement Technology, or ADEPT, spacecraft. The ADEPT vehicle consists of a woven carbon fiber thermal protection system (TPS) that is attached to a series of aluminum struts [3]. These struts are commanded to mechanically deploy the TPS around a rigid nose cone before atmospheric entry to form a semi-rigid aeroshell. The ADEPT vehicle modeled in the guidance flyoff included an asymmetrical aeroshell with a diameter of 16 meters and a nominal spacecraft mass of 52,000 kg, with a hypersonic lift-to-drag ratio of 0.27. Figure 2.4 shows a concept of the ADEPT vehicle when deployed.
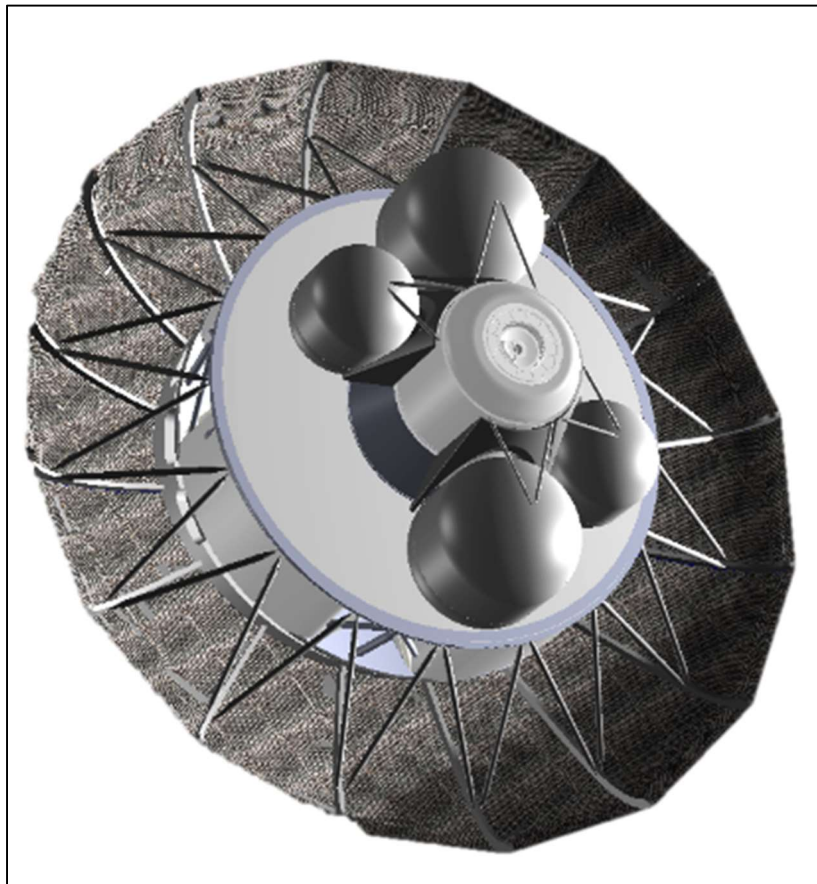
Fig. 2.4. ADEPT vehicle concept.

2.3.2 HIAD

The second vehicle simulated in FNPAG was the Hypersonic Inflatable Aerodynamic Decelerator, or HIAD. The HIAD is a low lift-to-drag vehicle made by lashing together a series of inflatable tori constructed of a Kevlar-like material [3]. The HIAD remains stowed until shortly before atmospheric entry, when it is deployed and inflated to form a protective shield around the vehicle. Mass savings from using an inflatable heat shield could potentially allow for significant cost savings, or could allow vehicles to carry larger scientific payloads. The model used for FNPAG had an 18 meter diameter, a nominal mass of 55,320 kg and a nominal hypersonic lift-to-drag ratio of 0.2, slightly lower than that of the ADEPT vehicle. Fig. 2.5 shows a conceptual HIAD vehicle in its fully-inflated configuration.
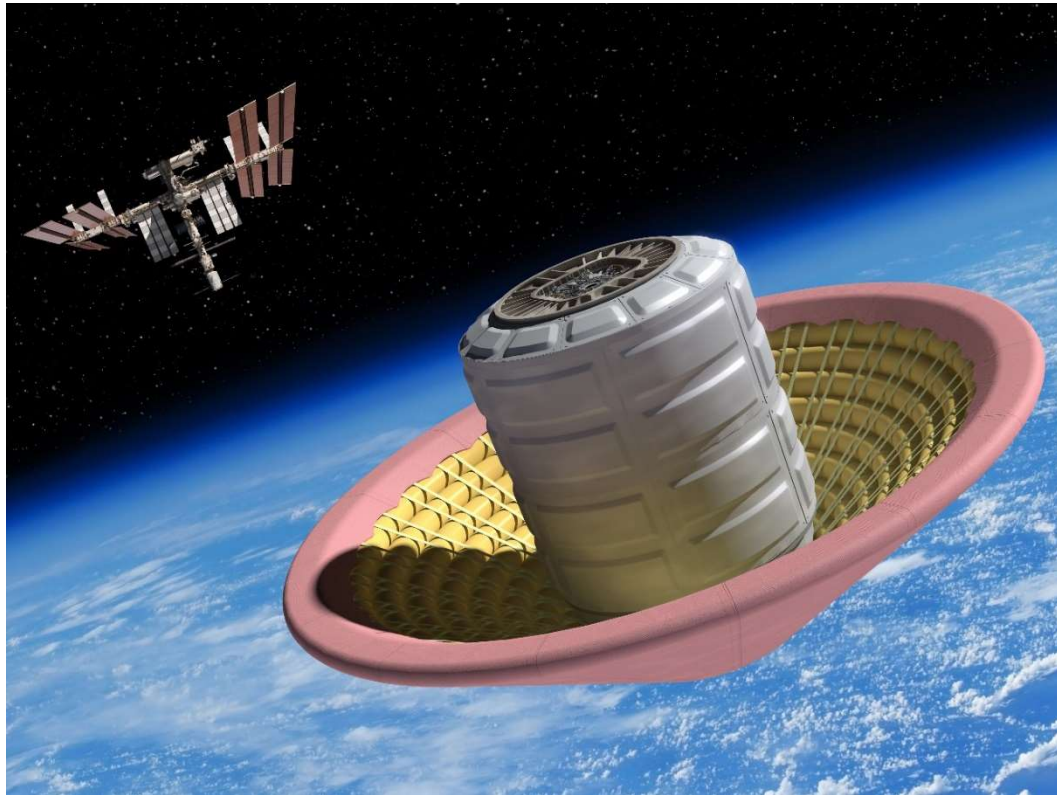
Fig. 2.5. Fully-inflated HIAD spacecraft.

2.3.3 Mid-L/D Rigid Vehicle

The last vehicle considered in the aerocapture guidance flyoff was a more traditional rigid aeroshell spacecraft, similar to the space shuttle. This spacecraft is known as the Mid-L/D Rigid Vehicle, or MRV [3]. The nominal MRV vehicle model used in the simulation had a length of 19.8 meters, a diameter of 8.8 meters, a height of 6.99 meters, a nominal vehicle mass of 60,000 kg, and a middle-of-the-road lift-to-drag ratio of 0.55. A depiction of this vehicle concept can be seen in Fig. 2.6.
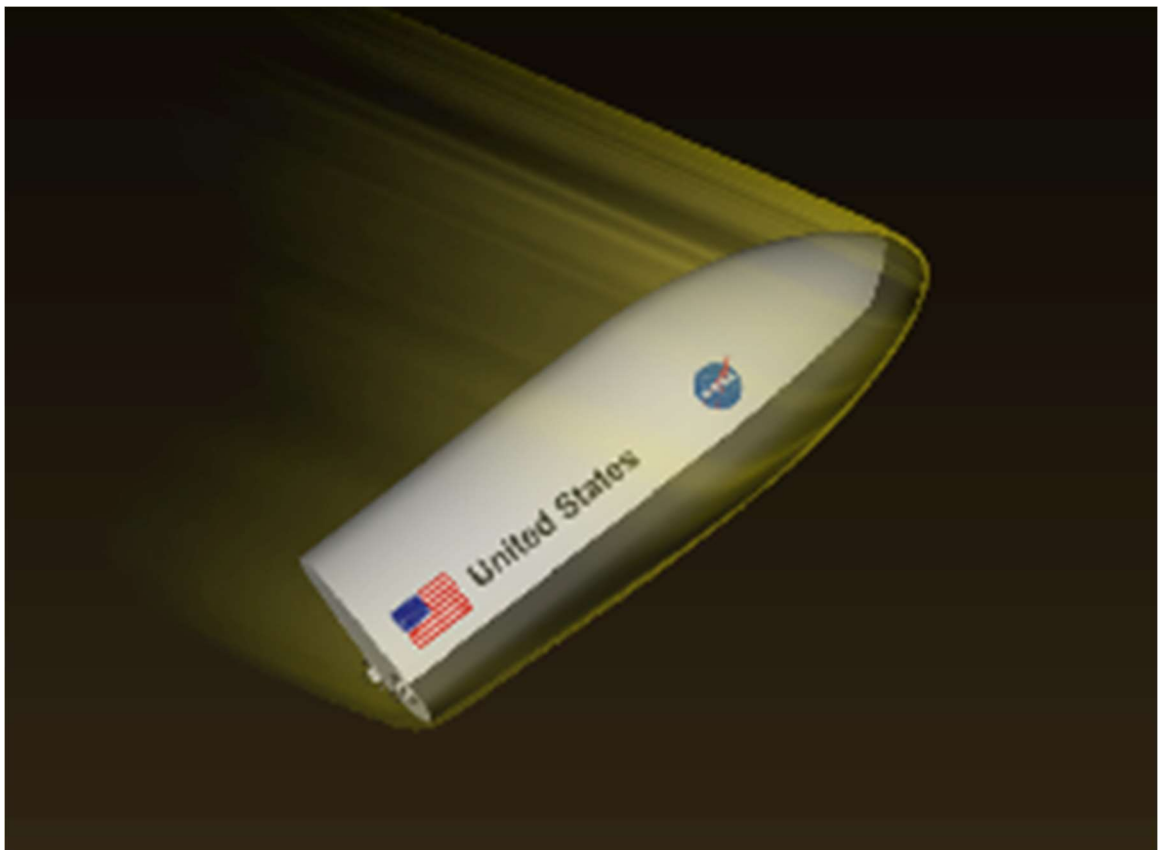
Fig. 2.6. MRV concept.

CHAPTER 3. FULLY NUMERICAL PREDICTOR-CORRECTOR AEROCAPTURE GUIDANCE ALGORITHM OVERVIEW

This Chapter provides an in-depth look into the inner workings of the Fully Numerical Predictor-Corrector Aerocapture Guidance (FNPAG) algorithm, as well as an overview of the three other algorithms tested in the aerocapture guidance flyoff described in Chapter 1. Section 3.1 describes the formulation of FNPAG, while Section 3.2 discusses the Terminal Point Controller (TPC) guidance algorithm, and Section 3.3 presents the Numerical Predictor-Corrector (NPC) algorithm developed at NASA Langley Research Center.

3.1 Fully Numerical Predictor-Corrector Aerocapture Guidance Algorithm

3.1.1 Optimal aerocapture solution

The defining characteristic of the FNPAG algorithm is its basis in the optimal control theory. Specifically, the algorithm is founded to address a subset of optimal aeroassist problems that are rooted in the following two assumptions, as noted by Lu [1]: that the performance index and terminal constraints depend explicitly on the terminal values of the longitudinal motion variables $r(t_f)$, $V(t_f)$, and $\gamma(t_f)$, and that the only control used is modulation of the bank angle, with a pre-determined angle of attack profile. This set of aeroassist problems includes the optimal aerocapture problem discussed in Chapter 2, when the only targeting condition addressed in the solution is Eq. (2.10), and also the two-burn optimal solution where there are no in-plane terminal constraints.

We begin by establishing a vector containing the longitudinal variables, $\boldsymbol{x}_{lon} = (r \ \ V \ \ \gamma)^T$. Using this vector, we can develop a performance index for the optimal control problem:

$$J = \eta(\boldsymbol{x}_{lon}(t_f)) \tag{3.1}$$

For this problem, η becomes either Eq. (2.15) for the one-burn solution or Eq. (2.17) for the two-burn solution. In addition, we denote up to 3 terminal constraints k that the trajectory must satisfy:

$$\boldsymbol{s}[\boldsymbol{x}_{lon}(t_f)] = 0 \tag{3.2}$$

where $t_f > t_0$ is free, and $\boldsymbol{s}: R^3 \rightarrow R^k$, represents a k-dimensional smooth vector function. For example, when solving the one-burn apoapsis-targeting problem, $k = 1$ and Eq. (3.1) takes the form of Eq. (2.10). By further ignoring the relatively small effects of planetary rotation and non-spherical gravity, we can reduce the longitudinal dynamics from Eqs. (2.1), (2.4), and (2.5) to the following:

$$\dot{r} = V \sin\gamma, \qquad r(t_0) = r_0 \tag{3.3}$$

$$\dot{V} = -D - \frac{\mu \sin\gamma}{r^2}, \qquad V(t_0) = V_0 \tag{3.4}$$

$$\dot{\gamma} = \frac{1}{V}\left[L \cos\sigma + \left(V^2 - \frac{\mu}{r}\right)\frac{\cos\gamma}{r}\right], \qquad \gamma(t_0) = \gamma_0 \tag{3.5}$$

where the bank angle σ is used as the control variable, subject to the given magnitude constraints:

$$0 \leq \sigma_{min} \leq |\sigma| \leq \sigma_{max} \leq \pi \tag{3.6}$$

Upon further examination, it is clear that the dynamics in Eqs. (3.3), (3.4), and (3.5) are decoupled from the rest of the three-degree-of-freedom dynamics given in Eqs. (2.2), (2.3), and (2.6). Because of this, we can develop a solution to the optimal control problem by only considering Eqs. (3.3-3.5). Using the Maximum Principle [21], the optimal bank angle is found from the optimality condition and can be seen in Eq. (3.7):

$$\sigma = arg\ max_{\sigma_{min} \leq \sigma \leq \sigma_{max}} \left\{ p_r V \sin \gamma + p_V \left(-D - \frac{\mu \sin \gamma}{r^2} \right) \right.$$
$$\left. + p_\gamma \left[\frac{L}{V} \cos \sigma + \left(V^2 - \frac{\mu}{r} \right) \frac{\cos \gamma}{rV} \right] \right\}$$
(3.7)

where p_r, p_V, and p_γ are the costates of each variable. Furthermore, $\cos \sigma$ is monotonic in $\sigma \in [\sigma_{min}, \sigma_{max}] \in [0, \pi]$, the right-hand side of Eq. (3.7) is linear in $\cos \sigma$, and L/V is always positive. Therefore, the optimal bank angle σ^* will be of the form:

$$\sigma^* = \begin{cases} \sigma_{min}, & if\ p_\gamma > 0; \\ \sigma_{max}, & if\ p_\gamma < 0; \\ \in [\sigma_{min}, \sigma_{max}], & if\ p_\gamma \equiv 0\ in\ [t_1, t_2] \in [t_0, t_f] \end{cases}$$
(3.8)

If p_γ is equal to 0 at any time in the interval t_1, t_2, the optimal bank angle could have any value between σ_{min} and σ_{max}. This phenomenon is known as singular optimal control. However, for the optimal aerocapture problem, singular optimal control has been determined to be impossible.

The Hamiltonian can be developed from Eqs. (3.3-3.5) as follows:

$$H = p_r V \sin \gamma + p_V \left(-D - \frac{\mu \sin \gamma}{r^2} \right) + p_\gamma \left[\frac{L}{V} \cos \sigma + \left(V^2 - \frac{\mu}{r} \right) \frac{\cos \gamma}{rV} \right] \quad (3.9)$$

where the costate variables are described by the following costate equations [21]:

$$\dot{p}_r = -\frac{\partial H}{\partial r} = p_V \left(\frac{\partial D}{\partial r} - \frac{2\mu \sin \gamma}{r^3}\right) - p_\gamma \frac{\partial f_\gamma}{\partial r} \tag{3.10}$$

$$\dot{p}_V = -\frac{\partial H}{\partial V} = -p_r \sin \gamma + p_V \frac{\partial D}{\partial V} - p_\gamma \frac{\partial f_\gamma}{\partial V} \tag{3.11}$$

$$\dot{p}_\gamma = -\frac{\partial H}{\partial \gamma} = -p_r V \cos \gamma + p_V \frac{\mu \cos \gamma}{r^2} - p_\gamma \frac{\partial f_\gamma}{\partial \gamma} \tag{3.12}$$

where f_γ is the right-hand side of Eq. (3.5):

$$f_\gamma = \frac{1}{V}\left[L \cos \sigma + \left(V^2 - \frac{\mu}{r}\right)\frac{\cos \gamma}{r}\right] \tag{3.13}$$

The impossibility of singular control here can be proven by contradiction [1]. If singular optimal control exists on the interval $[t_1, t_2] \in [t_0, t_f]$, it follows that $p_\gamma(t) \equiv 0$ from Eq. (3.8). If this is the case, we set $\dot{p}_\gamma = p_\gamma = 0$ in Eq. (3.12), and we can rearrange the right-hand side with the knowledge that $\cos \gamma \neq 0$ as follows:

$$\mu p_V /_{r^2} - V p_r = 0 \tag{3.14}$$

However, this problem does not have a fixed final time, and the dynamics in Eqs. (3.3-3.5) as well as Eq. (3.2) are autonomous. Using the Maximum Principle [21], the optimal trajectory will be subject to the following:

$$H = 0, \forall t \in [t_0, t_f] \tag{3.15}$$

We can use this to rearrange Eq. (3.9), remembering that $p_\gamma = 0$:

$$p_r V \sin \gamma - p_V D - p_V \frac{\mu \sin \gamma}{r^2} = 0 \tag{3.16}$$

If we substitute Eq. (3.14) into the above, noting that D is always positive, we get:

$$-p_V D = 0 \quad \rightarrow \quad p_V = 0 \tag{3.17}$$

If we substitute this solution back into Eq. (3.14), we find that $p_r = 0$. As a result, the entire costate vector $\boldsymbol{p} = \begin{pmatrix} p_r & p_V & p_\gamma \end{pmatrix}^T = 0$ over the interval $[t_1, t_2]$. Since the costate equations are affine in $\boldsymbol{p}$, and $\boldsymbol{p}$ is continuous over the interval $[t_0, t_f]$, then $\boldsymbol{p}(t)$ is 0 over the interval $[t_0, t_f]$. However, this contradicts a tenet of the Maximum Principle which requires that the costate vector $\boldsymbol{p}$ is nonzero. This contradiction occurs because a singular arc is assumed to exist in the optimal solution, and therefore, singular optimal control cannot exist as a solution to the optimal aerocapture problem.

Because the existence of singular optimal control is impossible, a guiding principal for the subset of optimal aeroassist problems discussed in this section can be developed [1]: for this subset of problems, the optimal bank angle magnitude profile will always have a bang-bang structure. Even when including the effects of planetary rotation and non-spherical gravity terms, the optimal solution will have a bang-bang bank angle profile as long as no terminal equality constraints dealing with lateral variables are included. This assertion has been backed up by numerical studies including [16], showing that the optimal aerocapture trajectory subject to three-degree-of-freedom dynamics and even final target inclination constraints will fly almost full lift up for the first part of the trajectory, followed by an almost full lift down phase. As shown in [16], this is because the propellant cost given in Eq. (2.15) is minimized by minimizing the flight path angle magnitude at atmospheric exit, and therefore by maximizing the relative velocity at atmospheric exit. Flying full lift up for the first phase of atmospheric flight raises the endo-atmospheric periapsis altitude, minimizing the velocity lost in the first phase. Then, flying full lift down for the second phase minimizes the flight-path angle magnitude at exit.

It should be noted that a flight conducted entirely in the full lift down phase is possible, where the entire trajectory is spent flying at $\sigma^* = \sigma_{max}$. This special case of bang-bang control would be caused by allowing a freely specified entry flight-path angle, and would result in the best performance in terms of ΔV minimization. However, a nominal full lift down trajectory would suffer from a lack of robustness when trajectory dispersions were introduced. For these reasons, it is best to select an entry flight path angle which allows for a true bang-bang optimal bank angle profile. It should also be noted that this analysis is valid for both the one-burn apoapsis targeting problem and for the two-burn ΔV-minimization problem. In both cases, the optimal bank angle profile will display these bang-bang characteristics.

3.1.2 FNPAG formulation

Once we have analyzed the optimal aerocapture problem and developed a solution, we can begin to develop the actual FNPAG algorithm. We have previously determined that for a given entry flight path angle, the optimal bank angle profile is of bang-bang structure, with a full lift up phase followed by a full lift down phase. This is achieved by setting a minimum and maximum bank angle of 0 and 180 degrees, respectively. However, if we set these minimum and maximum bank angles, there is no room to adjust the bank angle when trajectory dispersions and any other uncertainties are encountered. In addition, using 0 and 180 degrees as the respective minimum and maximum bank angles does not allow for any crossrange control, which is needed for the lateral guidance logic to function properly. For these reasons, we must select a larger minimum bank angle magnitude and

a smaller maximum bank angle magnitude to allow for guidance robustness and crossrange control capabilities.

As we discussed in Chapter 2, the optimal aerocapture guidance problem can be solved for both a one-burn apoapsis targeting condition and a two-burn ΔV minimization. FNPAG has two guidance modes to account for this. Mode 1 finds the optimal trajectory to meet the apoapsis targeting condition in Eq. (2.10) while minimizing the ΔV requirement in Eq. (2.15). Mode 2, on the other hand, finds the trajectory to minimize the two-burn ΔV sum in Eq. (2.17), without enforcing an explicit equality constraint.

Each of these guidance modes consists of two phases. Phase 1 begins at the entry interface at time t_0 and lasts until an unspecified time $t_s > t_0$. Phase 2 begins at t_s and lasts until atmospheric exit at time t_f. In accordance with the bang-bank optimal bank angle profile developed in the previous section, Phase 1 flies at a minimum bank angle magnitude of $\sigma_0 = 15$ deg. This magnitude is chosen based on the minimum bank angle flown by the Apollo entry guidance algorithm [7], and its value appears to have a minimal effect on the performance of FNPAG. Phase 2, on the other hand, flies at a relatively large bank angle magnitude, denoted σ_d. The selection of this value turns out to be the most important tuning parameter in finding a balance between excellent ΔV-minimization performance and superior robustness. This tuning process will be examined in more detail in Chapter 5.

Once σ_0 and σ_d are specified, the only unknown parameter in Phase 1 is the switching time t_s to move to Phase 2. This is the case for both guidance modes. The switching time is determined by the fully numerical predictor corrector algorithm developed in [22]. For Mode 1, t_s is found at every call to the guidance algorithm to satisfy the apoapsis targeting condition in Eq. (2.10). By performing an onboard numerical

integration loop, the atmospheric exit condition becomes a function of t_s, and Eq. (2.10) becomes a univariate root finding problem:

$$f(t_s) = r_a - r_a^* = 0 \qquad (3.18)$$

where the post-exit apoapsis radius r_a is a function of switching time t_s in Phase 1. The solution to this equation is found by implementing Brent's method [23]. This method is ideal because it offers the assured solution of the bisection method in combination with the quicker convergence of cubic interpolation. For Mode 2, t_s is found using the golden-section method to minimize the ΔV required in Eq. (2.17) [23]. Throughout Phase 1, the bank angle commanded is always of magnitude σ_0, but the switching time may vary between each guidance cycle, since it is calculated based on the current trajectory condition at each call to FNPAG. Figure 3.1 shows the planned bank angle magnitude profile used in Phase 1.
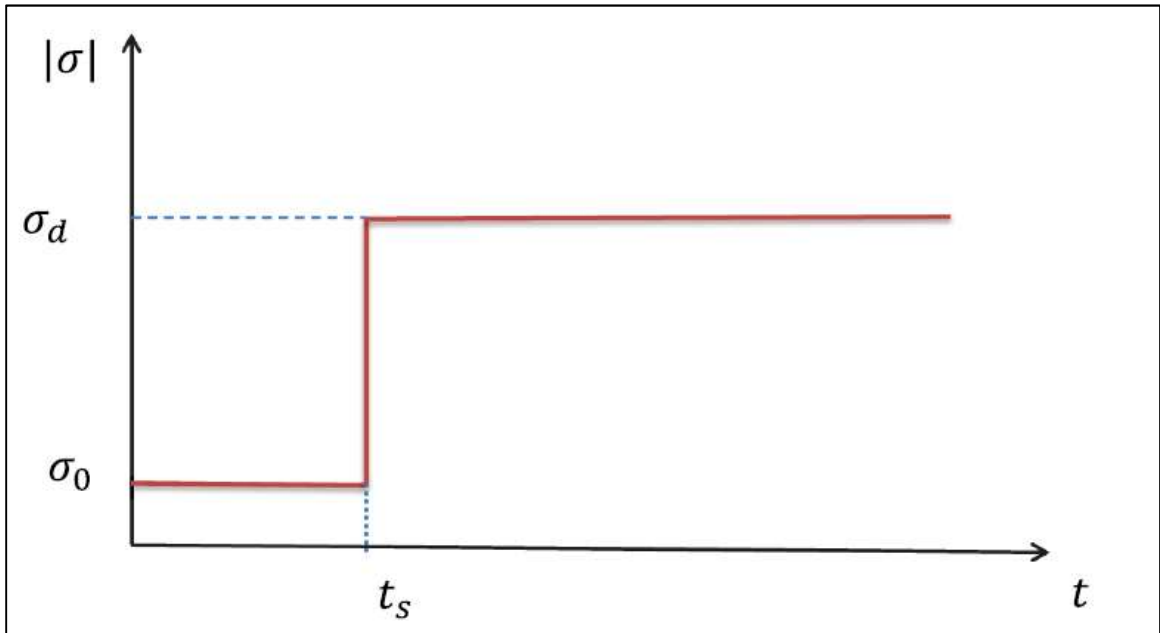
Fig. 3.1. Phase 1 bank angle magnitude profile [1].

As soon as the current time reaches the switching time t_s, FNPAG switches to Phase 2. In this phase, each call to the guidance algorithm involves finding a constant magnitude bank angle profile to either meet the targeting condition given in Eq. (2.10) or to minimize the $\mathit{\Delta V}$ requirement in Eq. (2.17). Once again, Brent's method is used for Mode 1 and the golden-section method is used for Mode 2. This section also uses the fully-numerical predictor corrector guidance algorithm developed in [22], albeit with a shorter time step. The bank angle commanded for each guidance cycle in Phase 2 will not necessarily be identical to σ_d due to trajectory dispersions, but should remain relatively close. This commanded bank angle may also change throughout Phase 2, since each guidance update uses the current trajectory state, making the FNPAG algorithm essentially a closed loop one.

In addition to Mode 1 and Mode 2, FNPAG also offers two additional modes. These two modes follow the same framework as Mode 1 and 2, but instead find a constant bank angle profile to satisfy either Eq. (2.10), used in Mode 3, or Eq.(2.17), used in Mode 4. Essentially, Modes 3 and 4 use the same framework as Modes 1 and 2, but with the switching time t_s equal to 0. This effectively reduces these modes to fly the entire trajectory in Phase 2. Table 3.1 provides an overview of each of the four guidance modes.

Table 3.1. FNPAG guidance modes.

FNPAG Mode	Objective	Number of Phases
Mode 1	Apoapsis-targeting condition (Eq. 2.10)	2
Mode 2	ΔV-minimization (Eq. 2.17)	2
Mode 3	Apoapsis-targeting condition (Eq. 2.10)	1
Mode 4	ΔV-minimization (Eq. 2.17)	1

3.1.3 Trajectory constraints

FNPAG also includes the option of enforcing inequality path constraints on the load

factor n and heating rate $\dot{Q}$, given in Eqs. (3.19) and (3.20):

$$n = \sqrt{L^2 + D^2} \leq n_{max} \tag{3.19}$$

$$\dot{Q} = k_Q\sqrt{\rho}V^{3.15} \leq \dot{Q}_{max} \tag{3.20}$$

where n_{max} is the peak limit in the load factor, $\dot{Q}_{max}$ is the heating rate limit at a stagnation

point on the spacecraft surface, and k_Q is a positive constant [22]. A predictive approach

has been developed in [22] to enforce these constraints by augmenting the bank angle

commanded by FNPAG with an altitude-rate feedback, although it was not used in this

particular guidance flyoff. This can be applied to any of the 4 modes offered in FNPAG,

and has been shown to be effective in simulations [22].

3.1.4 Estimating uncertainties

A number of uncertainties exist when it comes to modeling an aerocapture

trajectory. Perhaps the most impactful are uncertainties in the lift and drag coefficients C_L

and C_D, the pitching moment coefficient C_m, the location of the spacecraft center of gravity,

atmospheric density, and spacecraft mass. These uncertainties combine to have a

cumulative effect on the lift and drag accelerations L and D [1]. As has been demonstrated

in previous entry guidance efforts [22, 24, 25], first-order fading-memory filters are

implemented in FNPAG to estimate the following ratios:

$$\rho_L = \frac{L}{L^*} \tag{3.21}$$

$$\rho_D = \frac{D}{D^*} \tag{3.22}$$

where L and D are the sensed aerodynamic lift and drag accelerations and L^* and D^* are the nominal values of lift and drag acceleration. The scaling factors for the $(n + 1)$-th guidance cycle $\tilde{\rho}_L^{(n+1)}$ and $\tilde{\rho}_D^{(n+1)}$ are found as follows:

$$\tilde{\rho}_L^{(n+1)} = \tilde{\rho}_L^{(n)} + (1 - \beta)\left(\rho_L - \tilde{\rho}_L^{(n)}\right), \quad 0 < \beta < 1 \tag{3.23}$$

$$\tilde{\rho}_D^{(n+1)} = \tilde{\rho}_D^{(n)} + (1 - \beta)\left(\rho_D - \tilde{\rho}_D^{(n)}\right), \quad 0 < \beta < 1 \tag{3.24}$$

where ρ_L and ρ_D are based on current sensor data, $\tilde{\rho}_L^{(n)}$ and $\tilde{\rho}_D^{(n)}$ are the estimated ratios from the previous guidance cycle, and β is the time constant for the filters. Initially, $\tilde{\rho}_L^{(0)}$ and $\tilde{\rho}_D^{(0)}$ are set to 1. Then $\tilde{\rho}_L^{(n+1)}$ and $\tilde{\rho}_D^{(n+1)}$ are used to scale the nominal lift and drag accelerations to find an optimal solution for each guidance cycle. These fading-memory filters are able to accurately account for uncertainties in mass, atmospheric density, and aerodynamic coefficients. They have even shown superior performance when dealing with time-varying uncertainties, as seen in [24, 25].

3.1.5 Lateral logic

FNPAG includes two options for use in controlling lateral motion throughout a trajectory. The first option is a velocity-dependent deadband similar to those utilized in some of the older aerocapture algorithms discussed in Chapter 1. Based on the location in the trajectory, if the current inclination falls too far from the targeted final inclination, a bank reversal will be commanded. The logic is setup such that larger inclination errors are allowed earlier in the trajectory, while the deadband tightens as the vehicle nears the exit interface. While this method is simple and effective, it requires tuning of the deadband

threshold to set the number of bank reversals for a nominal trajectory. In addition, the number of bank reversals for the nominal trajectory may not be the same as the number of reversals commanded when dispersions are applied.

The second lateral logic included in FNPAG uses a technique proposed by Smith which allows the user to specify a number of bank reversals [26]. This predictive logic uses a numerical predictor-corrector loop to integrate the trajectory twice from the current condition to atmospheric exit, one with the current bank sign, and one with the opposite. The crossrange error at the exit interface using the current bank sign is denoted as χ^+, and the error using the opposite sign is denoted as χ^-. As the vehicle travels along the trajectory, it loses velocity and therefore the crossrange capability of the vehicle is lessened. By flying at the same bank sign, χ^+ will increase, while simultaneously the magnitude of χ^- will decrease. Eventually, the magnitude of χ^- will reach 0, meaning even when a bank reversal is performed, the vehicle will not be able to reach the target due to a finite bank rate and acceleration.

The solution to this problem is to command a bank reversal when the magnitude of χ^- is much smaller than that of χ^+. A variable K is denoted to represent the ratio of these magnitudes. When this threshold is reached, a bank reversal is commanded, and the value of χ^+ is set equal to the old value of χ^-. Then, another bank reversal occurs when this new ratio exceeds the value of K. By doing this, the terminal crossrange of the vehicle is reduced by a factor of K for each commanded bank reversal. This is expressed by the following:

$$|\chi_f| = \frac{|\chi_0|}{K^n} \tag{3.25}$$

where n is a specified number of bank reversals, χ_f is the crossrange error at atmospheric exit, and χ_0 is the crossrange error at the initial condition. Given a user-defined crossrange error (the final desired inclination error at atmospheric exit for FNPAG), Eq. (3.25) can be solved for K:

$$K = \left|\frac{\chi_0}{\chi_f}\right|^{\frac{1}{n}} \tag{3.25}$$

This equation is adapted into a closed-loop lateral logic by using the current crossrange error $\chi(t)$ and by specifying the number of bank reversals n left to be performed. When this is established, Eq. (3.25) becomes:

$$K = \left|\frac{\chi(t)}{\chi_f}\right|^{\frac{1}{n}} \tag{3.26}$$

Then, any time the ratio of $\chi(t)$ to χ^- exceeds K, a bank reversal is committed and n is decreased. This is repeated for every guidance call until n reaches 0. Testing has shown this to be a robust and high-performing algorithm, with the same user-specified number of bank reversals remaining constant despite dispersions [22]. For the flyoff, a modified version of this logic was implemented using the wedge angle error instead of crossrange error. This method has also proven to be quite successful, as will be demonstrated in Chapter 5.

3.2 Terminal Point Controller Guidance

One of the other aerocapture guidance algorithms used in the guidance flyoff is known as the Terminal Point Controller, or TPC. TPC guidance was derived from the entry guidance used on the Apollo mission, and was adapted by changing the existing boundary conditions to be applicable to aerocapture trajectories [27]. This algorithm is based on the adjoint state method, and was originally developed for use in the Mars Surveyor Program in 2001.

The TPC guidance algorithm uses a reference trajectory generated offline and includes a feedback guidance loop to target a desired terminal condition. In this algorithm, the equations of motion are also integrated backwards offline along the previously generated reference trajectory from the final target condition and stored for use in the algorithm. From this integration, a set of four controller gains are determined and used in conjunction with an energy table, a velocity table, a drag acceleration profile table, and a bank angle table to determine the required bank angle command given at each guidance cycle. These gains are scheduled by the orbital energy at each guidance call. The control vector $\boldsymbol{u}$ is established using Eq. (3.27):

$$\delta u = \frac{-\boldsymbol{\lambda}^T \delta \boldsymbol{x}|_{t=t_0}}{\int_{t_0}^{t_f} \left(\frac{\delta \boldsymbol{f}}{\delta \boldsymbol{u}}^T \boldsymbol{\lambda} \right) dt} \tag{3.27}$$

where $\boldsymbol{x}$ is the state vector consisting of the downrange s, velocity V, flight path angle γ, and altitude h, $\boldsymbol{\lambda} = [\lambda_s(t) \quad \lambda_V(t) \quad \lambda_\gamma(t) \quad \lambda_h(t)]^T$ are the integrating factors for each state, and $\boldsymbol{f}$ is the state vector using the equations of motion for a vehicle flying through the atmosphere. An illustration of the TPC guidance routine is shown in Fig. 3.2.
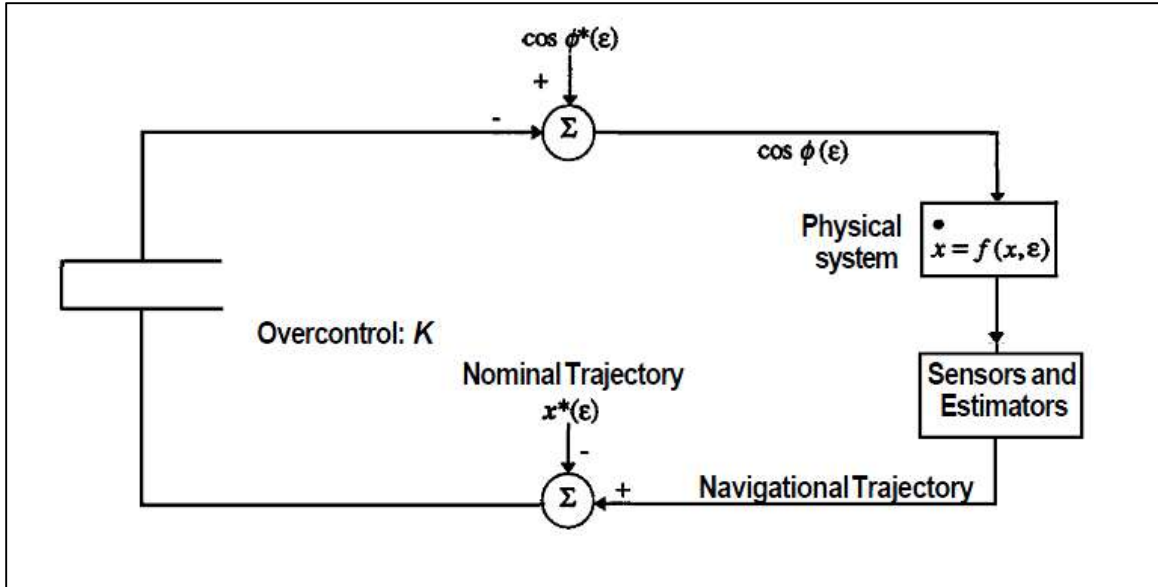
Fig. 3.2. TPC feedback guidance loop [27].

The TPC guidance algorithm uses a deadband controller to determine when to perform a
bank reversal. This deadband is based on the difference between the current inclination of
the vehicle and the desired inclination of the final orbit.   The width of the deadband
decreases as the vehicle nears the end of the atmospheric flight.   For more detailed
information on the development of the TPC algorithm, see [27].

3.3 Numerical Predictor-Corrector Guidance

Like the TPC guidance algorithm, the Numerical Predictor-Corrector Guidance, or
NPC, algorithm was developed at NASA Langley in support of the 2001 Mars Surveyor
Program. The NPC algorithm was also originally developed for entry guidance, and an
aerocapture guidance mode was later developed.

The NPC algorithm uses a roll reversal numerical predictor-corrector to generate a
bank angle command [28]. This involves an algorithm consisting of two guidance loops.
The inner loop contains the numerical predictor-corrector logic, in which the equations of

motion are integrated forward throughout the entire trajectory to find a bank angle command with a constant magnitude. The outer loop then adjusts the commanded bank angle in real time based on the current state of the vehicle. It should be noted that no optimization routine is performed to minimize the post-atmospheric exit propellant mass required to reach the target orbit.

Although not identical to the predictive lateral logic implemented in FNPAG, the NPC algorithm does use some form of predictive logic to determine when to perform a bank reversal. This logic is nested in the inner loop of the algorithm. It should be noted that the specified bank reversal times cannot be adjusted by the outer loop guidance like the bank angle magnitude [28]. Bank reversals are determined by a deadband controller using inclination as the criteria for reversal. For more information on the development of the NPC guidance algorithm, see [28].

CHAPTER 4. SIMULATION ENVIRONMENT

This Chapter discusses the simulation environment used in conducting the aerocapture guidance flyoff described in the previous chapters. FNPAG and the other guidance algorithms were implemented and simulated in a high-fidelity simulation environment at NASA Langley Research Center. This environment is known as the Program to Optimize Simulated Trajectories II, or POST2. An overview of POST2 is given in Section 4.1. Section 4.2 introduces the gravity model, the navigation models, and the pseudocontroller developed for use in POST2, respectively. Section 4.3 introduces the initial conditions and post-atmospheric-exit target conditions that were selected for the guidance flyoff, and section 4.4 provides a description of the dispersions used in executing the Monte Carlo simulations for each algorithm, vehicle, and target orbit. Finally, Section 4.5 introduces the figures of merit used in evaluating the performance of each algorithm.

4.1 Program to Optimize Simulated Trajectories II Overview

The Program to Optimize Simulated Trajectories II, or POST2, is a high-fidelity simulation environment developed by NASA Langley Research Center. The original POST software was created in the 1970s to simulate space shuttle trajectories [29]. POST2 was adapted from the original POST code beginning in 1995, and additional functionality has been added throughout the years. POST2 is capable of compiling code written in both C and FORTRAN, giving users a great deal of flexibility in running simulations.

While the original POST simulation restricted users to a single vehicle, POST2 allows users to select and optimize orbital trajectories simultaneously for a plurality of

vehicles orbiting any oblate celestial body. These vehicles may be powered, such as a launch vehicle for a lunar orbit, or unpowered, as in the case of an aerocapture trajectory. The source code offers a multitude of models for use in simulating trajectories, including atmospheric, propulsion, gravity, and controller models, among others. POST2 also boasts both 3 and 6 degree-of-freedom simulation capabilities. Moreover, these can be run simultaneously, i.e. one vehicle can be run in a 3DOF trajectory at the same time as another vehicle in a 6DOF trajectory. In fact, a single vehicle trajectory can be divided into multiple segments, with each individual segment being 3DOF or 6DOF [29].

Perhaps the most useful improvements developed for POST2 are its Monte Carlo simulation capabilities. These types of simulations are invaluable for trade studies such as the aerocapture guidance flyoff performed in this thesis. Because it allows vehicle models created by the user to be integrated into the simulation, any vehicle can be used to conduct a trajectory analysis. In addition, POST2 contains dispersion capabilities for a number of variables that allow for large-scale dispersed trajectory simulations. Moreover, POST2 allows users to optimize these trajectories based on user-defined constraints, and although this feature was not used for the guidance flyoff, it has the potential to be applied in future trade studies.

4.2 Gravity, Navigation, and Controller Models

POST2 has a wide variety of models that can be included in running trajectory simulations. One such model is the planetary gravitational model. POST2 includes the capability of simulating a simple spherical planetary gravity field all the way up to a harmonic field with hundreds of perturbing effects. For the aerocapture guidance flyoff, an 85x85 spherical harmonic gravity field developed by JPL was selected, requiring inputs for the Martian rotation rate, equatorial and polar radii, mean radius, and gravitational constant.

POST2 also includes an in-depth navigational toolbox that allows users to introduce anomalies such as biases and uncertainties in inertial measurement units and other sensors. Because of the preliminary nature of the guidance flyoff, perfect navigation was used to create a baseline of expected performance from each algorithm, although in the future these capabilities may be utilized.

The last notable model used in the flyoff was a pseudo-controller that simulated the effects of controller limits on the commanded bank angle. For this flyoff, the maximum bank rate was limited to 20 deg/s, and the maximum bank acceleration was capped at 5 deg/s^2. Limiting changes in the commanded bank angle to a finite rate allows for more realistic performance from the guidance algorithms.

4.3 Initial Conditions and Target Orbit Parameters

Each vehicle was run using the same set of initial conditions, simulating an entry near the north pole of Mars on a north-south trajectory. For consistency, all runs were conducted with the same starting date, in this case an entry time of midnight on May 10, 2033, a date in the lower part of the Martian pressure cycle. The vehicle state was initialized at a point in space such that it would reach the atmospheric entry interface at a velocity of 6200 m/s after flying for thirty seconds. The entry interface was set at an altitude of 126 km. Table 4.1 displays a full list of the vehicle state used to initialize each trajectory. It should be noted that the initial flight path angle was free to be chosen by the user, so a different entry flight path angle was used for each of the three vehicles. This will be further explored in the results of the nominal runs presented in Chapter 5.

Table 4.1. Nominal POST2 initial conditions.

B-plane angle	270 deg
Geodetic altitude	185.4 km
Mars-relative velocity	6.1782 km/s
Hyperbolic excess velocity	3.76 km/s
Orbital inclination	90 deg
Geocentric latitude	84.5 deg
Longitude	90 deg
Heading angle	180 deg
Julian date	2463727.5 days

To test the capabilities of each algorithm used in the flyoff, two final target orbits were suggested, a 1-sol and a 5-sol elliptical orbit. Although both orbits share the same periapsis altitude, inclination, and ascending node, the 5-sol orbit has a much higher apoapsis altitude, which means it requires a smaller propellant mass to establish the orbit after exiting the atmosphere. However, because it is so eccentric, any small errors at atmospheric exit have a much more profound effect on the algorithm's performance than when attempting to reach the 1-sol orbit. Table 4.2 displays the characteristics of both of these target orbits.

Table 4.2. Post-atmospheric-exit target orbits.

Parameter	1-sol orbit	5-sol orbit
Periapsis altitude	250 km	250 km
Apoapsis altitude	33793 km	112400 km
Inclination	90 deg	90 deg
Longitude of ascending node	270 deg	270 deg
Argument of periapsis	90 deg	90 deg

4.4 Monte Carlo Dispersions

Each vehicle was simulated for both a 1-sol orbit and a 5-sol orbit, with 8,000 dispersed cases being run for each target orbit. Dispersions applied to the nominal state included aerodynamic uncertainties in the vehicle, uncertainties in the Martian atmospheric density, mass uncertainties, and a dispersed initial condition applied through a state covariance matrix based on the initial state covariance matrix used in simulating the Mars Science Laboratory entry guidance [30]. Vehicle aerodynamic dispersions were applied through NASA-provided model databases, using normal dispersions to alter the lift and drag coefficients of each vehicle. Atmospheric dispersions were applied using Mars GRAM 2010 with the *rpscale* variable set to 1.0. This places a normal dispersion on the atmospheric density. All of the other dispersion types are available for reference in Table 4.3.

Table 4.3. Monte Carlo dispersions.

Variable	Dispersion (3σ bounds for normal distributions)	Distribution
MARS Gram *dusttau*	0.1-0.9	uniform
Vehicle mass bias	+/- 500 kg	normal
C.G. bias, x-direction	+/- 0.05 m	normal

4.4.1 *Dusttau* effects

Of all of the applied Monte Carlo dispersions, the *dusttau* variable has perhaps the most dramatic effect. This variable simulates the effects of dust present in the Martian atmosphere on its density at different points around the planet. Higher values of *dusttau*

lead to more dust and thus higher atmospheric densities, which can cause the vehicle to undershoot its apoapsis target and lead to higher ΔV requirements, with some cases showing a ΔV increase as high as 30 percent. In addition, the relationship between *dusttau* and ΔV performance is nonlinear, as seen in Fig 4.1, conducted using a nominal *dusttau* of 0.5 for the guidance.
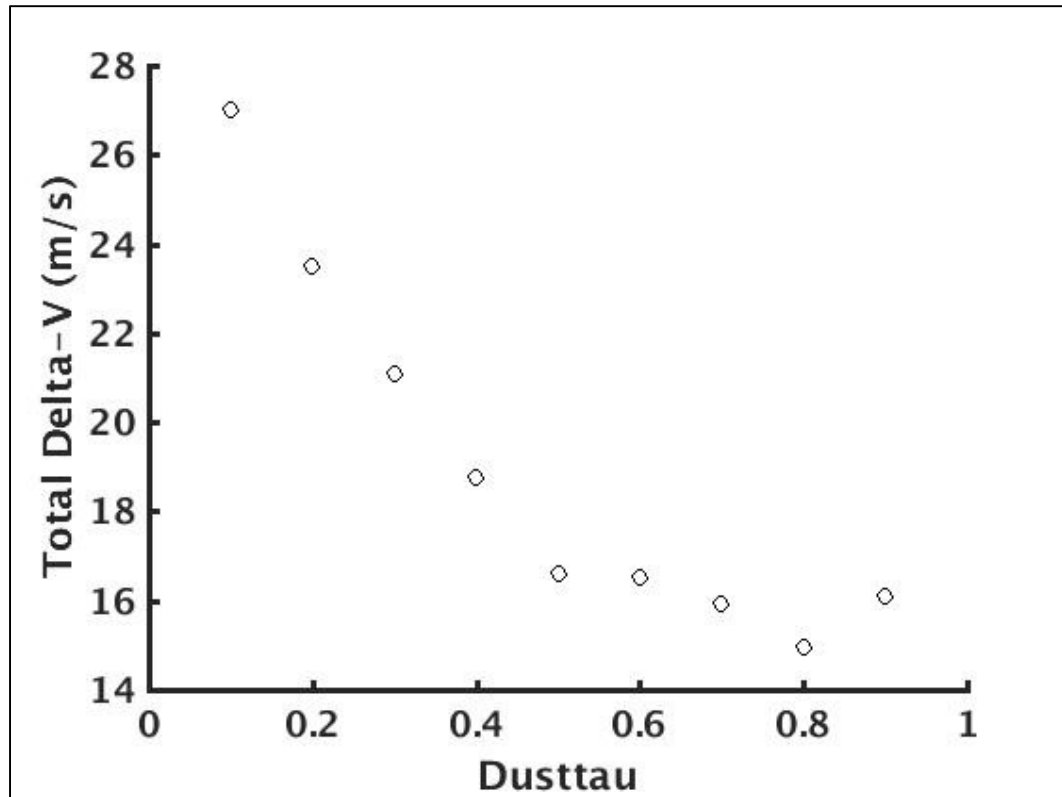
Fig. 4.1. *Dusttau* effect on ΔV requirement.

A simple solution to this problem is to select a guidance *dusttau* value such that the mean ΔV is minimized, as shown in Fig 4.2. Because this value has proven to be vehicle-dependent, the *dusttau* value fed to the guidance algorithm will be discussed further in Chapter 5.
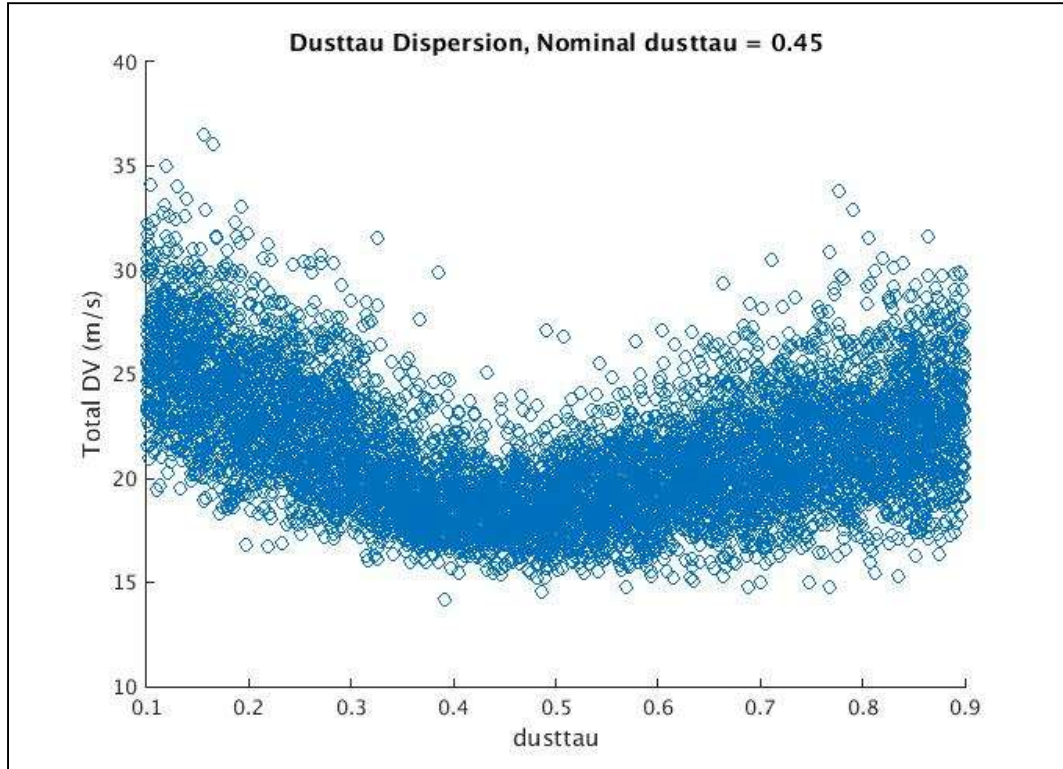
Fig. 4.2. Minimizing *dusttau* effects through nominal *dusttau* selection.

4.5 Figures of Merit

A number of figures of merit were developed for comparing the performance of the algorithms participating in the aerocapture guidance flyoff. The main figure of merit involved the sum of the magnitudes of the three post-atmospheric-exit trajectory correction burns, used to place the vehicle into its final orbit. These burns include a periapsis raise maneuver conducted near the vehicle's post-exit apoapsis, an apoapsis correction burn conducted at the now-raised periapsis, and final propulsive burn to clean up the wedge angle, conducted at the node with the largest altitude to minimize the ΔV cost. The 99th-percentile of the total ΔV budget, meaning the ΔV cost which was greater than or equal to

the cost in 99 percent of the Monte Carlo trials, was used to determine the overall winner of the flyoff.

In addition to the ΔV budget, a few other figures of merit were selected to gain insight on the performance of each algorithm. These included the 99th-percentile value of the projected apoapsis altitude error at atmospheric exit and the 99th-percentile of the projected periapsis altitude at atmospheric exit. Although these values do not explicitly relate to the propulsive cost of reaching the final orbit, they may provide insight into why a certain trajectory had a higher ΔV cost than others. The final figure of merit was the number of bank reversals commanded throughout the trajectory, as each bank reversal requires additional propellant.

A number of variables were output for each simulation to provide a basis of comparison between the algorithms. At the atmospheric entry interface, the inertial flight path angle and velocity were selected. At the periapsis of the atmospheric flight, the altitude and wedge angle were analyzed. Finally, at atmospheric exit, the predicted apoapsis altitude, periapsis altitude, the maximum g-load, the maximum stagnation heat rate, the maximum stagnation total heat load, and the wedge angle were all recorded. This data was gathered to give a more in-depth picture of the differences between the guidance algorithms. The results of the flyoff and the data gathered from these variables are presented in Chapter 5.

CHAPTER 5. SIMULATION RESULTS

This Chapter presents the results of the aerocapture guidance flyoff conducted at NASA Langley Research Center. Results for FNPAG and TPC guidance using the ADEPT vehicle will be compared in Section 5.1. Additional FNPAG results for the HIAD vehicle are shown in Section 5.2. Section 5.3 displays the results from simulating the Mid-L/D rigid aeroshell vehicle. A table comparing the results from all simulations can be found in Section 5.4, while Section 5.5 discusses results of a comparison between FNPAG and NPC.

5.1 ADEPT Simulation Results

As discussed in Chapter 4, the entry flight path angle and the value of the *dusttau* Mars GRAM variable to be used by FNPAG were free to be chosen by the user. For the ADEPT vehicle, the value chosen for the inertial entry flight path angle was -11.3 degrees, and the nominal *dusttau* value passed into the guidance was 0.45. The following subsections will present the data gathered from these simulations. FNPAG was run using Mode 2 (minimizing the two-burn in-plane ΔV magnitude) for all sections in Chapter 5, using predictive lateral logic and commanding two bank reversals for all cases.

5.1.1 1-sol nominal results

Due to time constraints, the only two algorithms able to complete the simulations required for the flyoff were FNPAG and the TPC algorithm. For the nominal case, FNPAG outperformed the TPC guidance in terms of total ΔV requirements, with a three-burn ΔV magnitude of 18.67 m/s vs. 23.51 m/s for TPC. This translates to a 20% reduction in

propellant required to reach the final target orbit. Figure 5.1 shows the bank angle profiles for the nominal representative case, with FNPAG guidance in red and TPC guidance in blue. This color scheme will be used throughout the algorithm comparison.
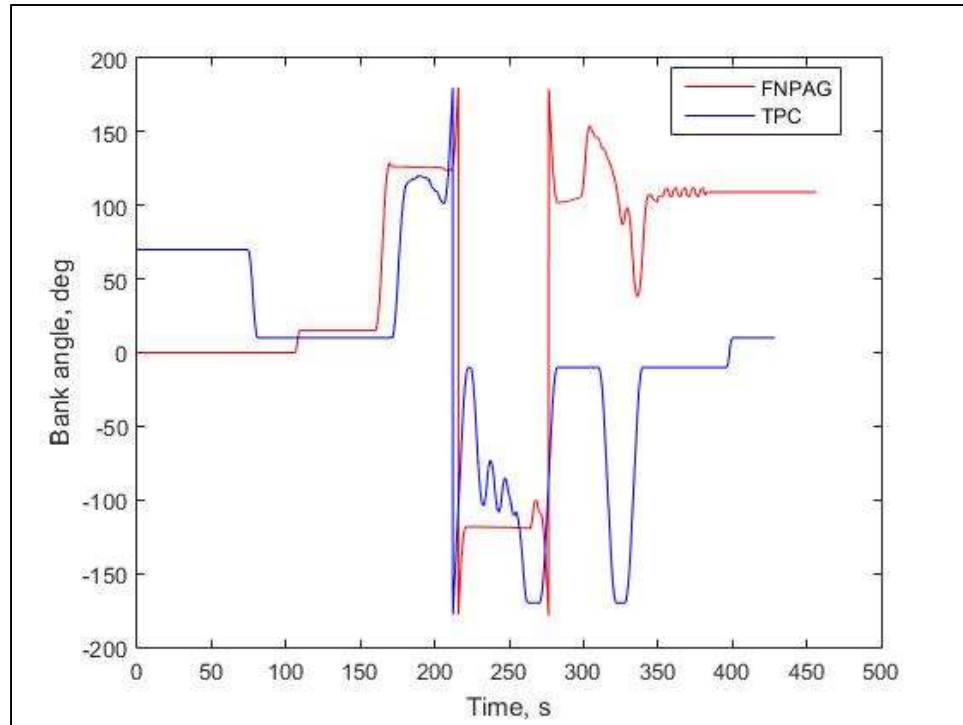
Fig. 5.1. ADEPT nominal bank angle vs. time, 1-sol orbit.

It can be seen that through extensive tuning of the TPC algorithm, the bank angle profiles turn out to be fairly similar. However, FNPAG better maintains the bang-bang profile described in Chapter 3, and this causes the additional reduction in ΔV requirements. In addition, FNPAG flies a trajectory that experiences a lower load on the vehicle, as seen in Fig. 5.2. This could prove useful for future manned missions to Mars, when load factor on a human crew is much more limited than that of an unmanned vehicle. In addition, FNPAG allows for a lower maximum convective heat rate on the vehicle than TPC guidance as shown in Fig. 5.3, causing less stress on the heat shielding of the ADEPT vehicle.
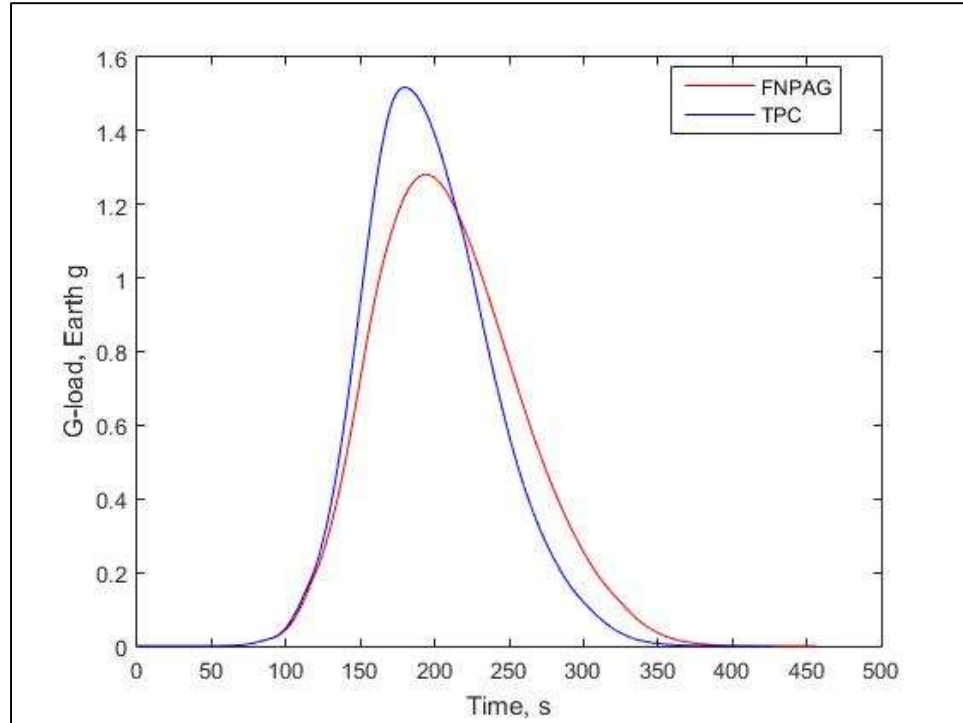
Fig. 5.2. ADEPT nominal g-load vs. time, 1-sol orbit.
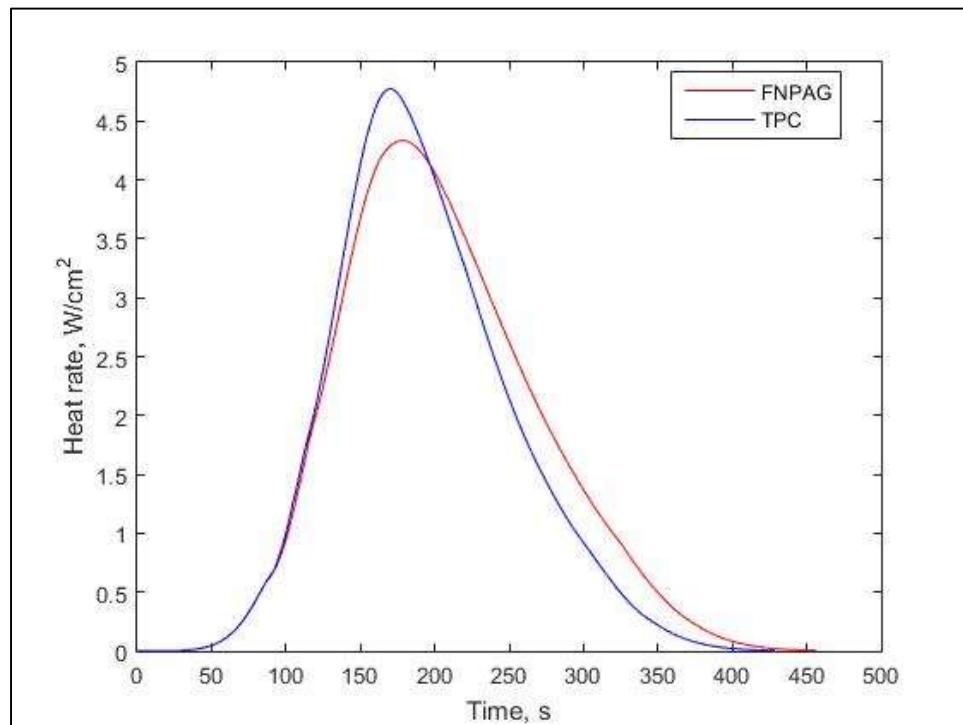
Fig. 5.3. ADEPT nominal heat rate vs. time, 1-sol orbit.

Figure 5.4 shows the nominal planetodetic altitude profile for each of the guidance algorithms, and Fig. 5.5 displays the relative velocity profile. At first glance, both of these figures seem quite similar. In fact, the exit velocity for TPC is only 6.2 m/s higher than that of the FNPAG trajectory. This would appear to give the TPC algorithm the upper hand. However, in addition to velocity at the exit interface, the required propellant budget also depends significantly on the exit flight path angle, with a shallower angle at atmospheric exit leading to a lower ΔV requirement. As can be seen in Fig. 5.6, the FNPAG trajectory exits the atmosphere at a flight path angle that is approximately 0.33 degrees shallower than the TPC trajectory, and this is the primary factor that leads to a 20% difference in propellant mass budget.
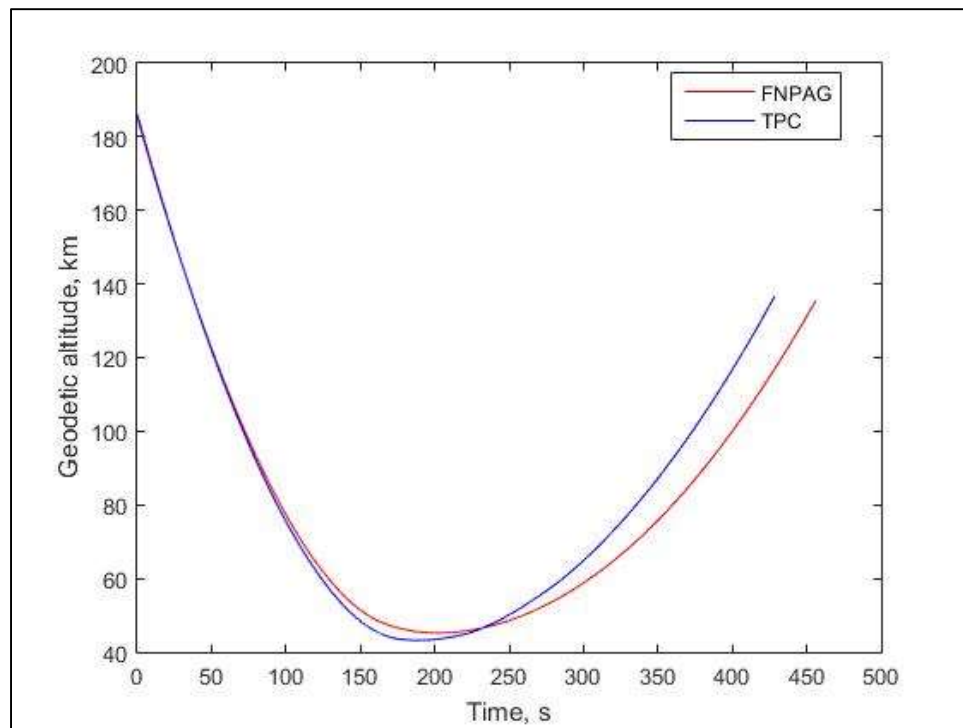
Fig. 5.4. ADEPT planetodetic altitude vs. time, 1-sol orbit.
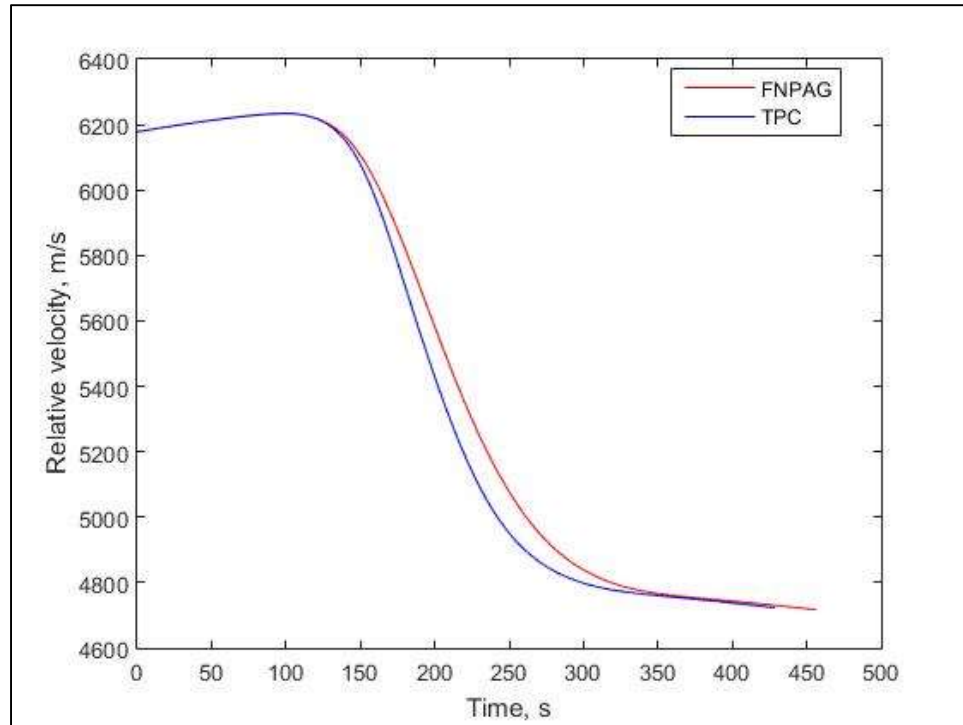
Fig. 5.5. ADEPT relative velocity vs. time, 1-sol orbit.
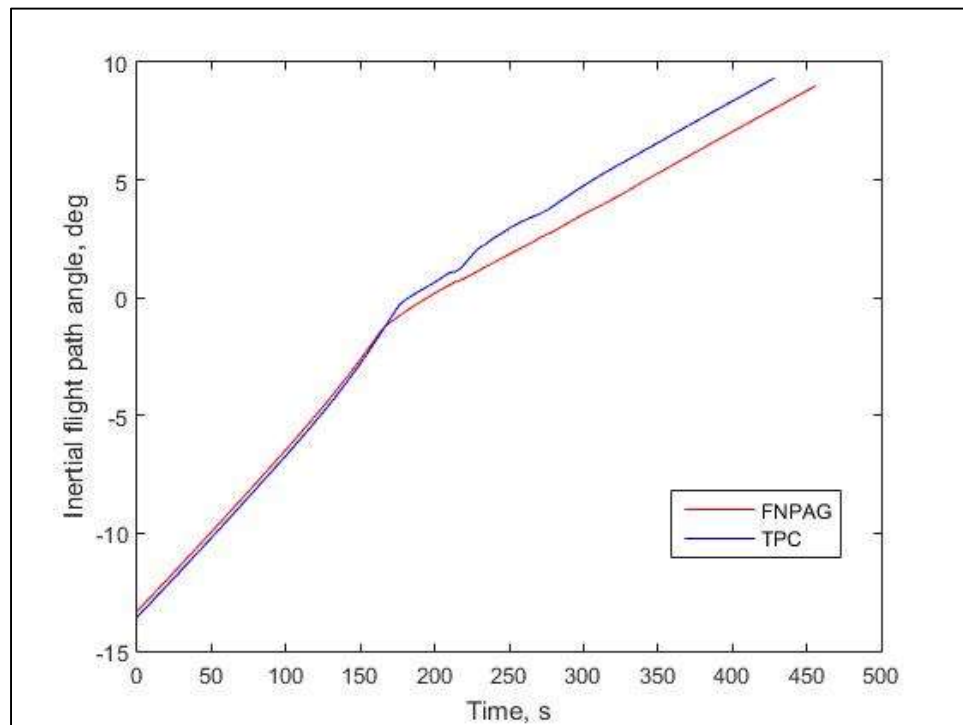
Fig. 5.6. ADEPT inertial flight path angle vs. time, 1-sol orbit.

5.1.2 1-sol Monte Carlo results

Chapter 4 described the simulation environment and setup for the aerocapture

guidance flyoff, including the Monte Carlo dispersions and figures of merit. The flyoff

consisted of 8,000 dispersed trajectories using the ADEPT vehicle and a 1-sol target

orbit. The main figure of merit was the 99th percentile value of the total ΔV requirement

to reach the final orbit. FNPAG had a 99th percentile value of 29.91 m/s, while the TPC

algorithm had a slightly higher 99th percentile value of 31.09 m/s. Detailed statistics on

the algorithm performance are given in Table 5.1. In addition, Fig. 5.7 displays a

histogram of the ΔV requirement for each algorithm. Clearly, FNPAG shows more cases

with a smaller propellant requirement than TPC.

Table 5.1. ADEPT total ΔV required (m/s), 1-sol target orbit.

	FNPAG	TPC
Mean	21.21	21.67
3-sigma	9.32	10.37
Min	14.16	15.40
5.00-percentile	17.09	16.89
50.00-percentile	20.67	21.30
95.00-percentile	26.98	27.89
99.00-percentile	29.91	31.09
Max	36.50	49.93
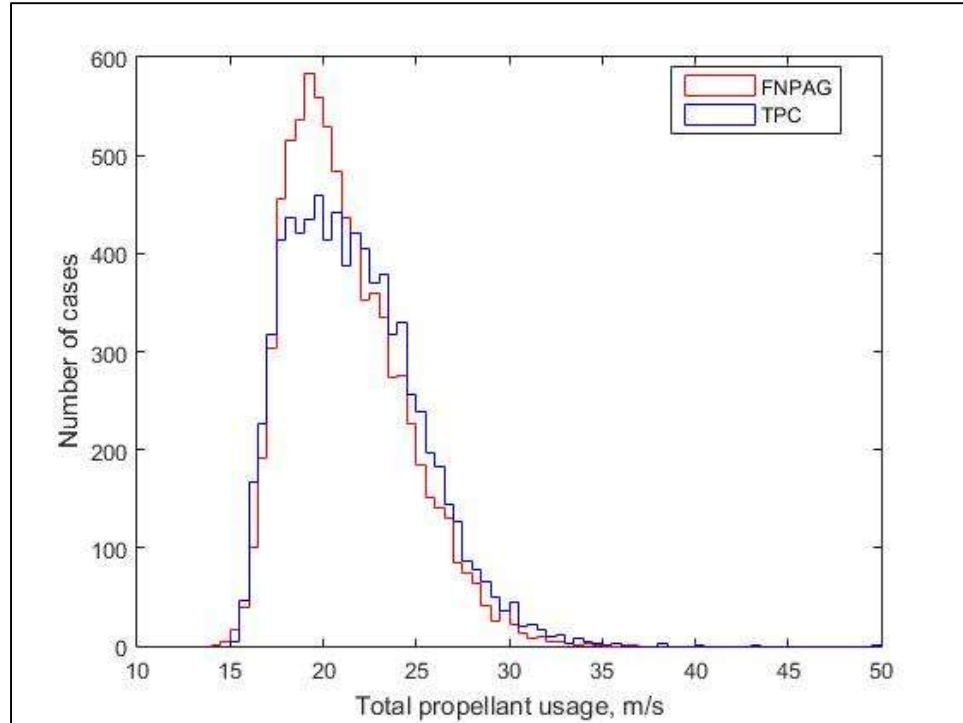
Fig. 5.7. ADEPT histogram of ΔV performance, 1-sol orbit.

To gain insight into the reasons for FNPAG's performance advantage over TPC, data for a number of other variables will be presented as well. First, trajectories flown using FNPAG guidance tended to have a higher planetodetic altitude at the periapsis point during atmospheric flight. This is shown in Table 5.2 as well as in Fig. 5.8. Because trajectories flown using FNPAG do not fly as low into the Martian atmosphere, they are able to follow a longer, flatter profile that allows them to exit the atmosphere at a shallower flight path angle, which leads to less post-exit propellant consumption, as discussed in Section 5.1.1.

Table 5.2. ADEPT periapsis altitude (km) for aerocapture trajectory, 1-sol orbit.

	FNPAG	**TPC**
Mean	45.28	43.56
3-sigma	2.14	1.54
Min	43.44	42.14
5.00-percentile	44.12	42.77
50.00-percentile	45.37	43.55
95.00-percentile	46.31	44.42
99.00-percentile	46.54	44.73
Max	47.01	45.24
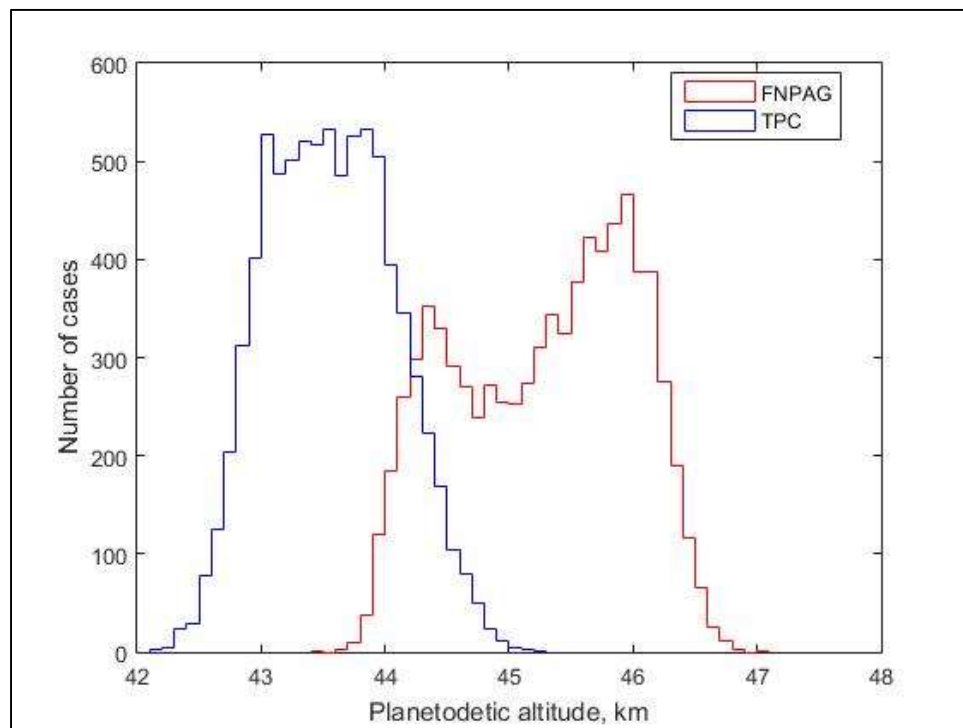
Fig. 5.8. ADEPT histogram of periapsis altitudes, 1-sol orbit.

The next variable to examine is the predicted apoapsis altitude at atmospheric exit, at which the first trajectory correction burn is to occur. It can be seen in Table 5.3 and Fig. 5.9 that FNPAG displays superior performance in reaching the target apoapsis of 33,793 km for the 1-sol case. This occurs despite the fact that FNPAG is being run in Mode 2, which does not explicitly target an apoapsis altitude. It turns out that even though this constraint is not enforced, it happens to be the most effective method of minimizing propellant costs.

Table 5.3. ADEPT predicted apoapsis altitude (km) at atmospheric exit, 1-sol orbit.

	FNPAG	TPC
Mean	34154.65	34324.13
3-sigma	2923.60	3139.15
Min	31486.97	29534.14
5.00-percentile	32821.74	32651.59
50.00-percentile	33954.24	34284.70
95.00-percentile	35939.81	35987.84
99.00-percentile	36609.10	36579.50
Max	37939.77	37988.60
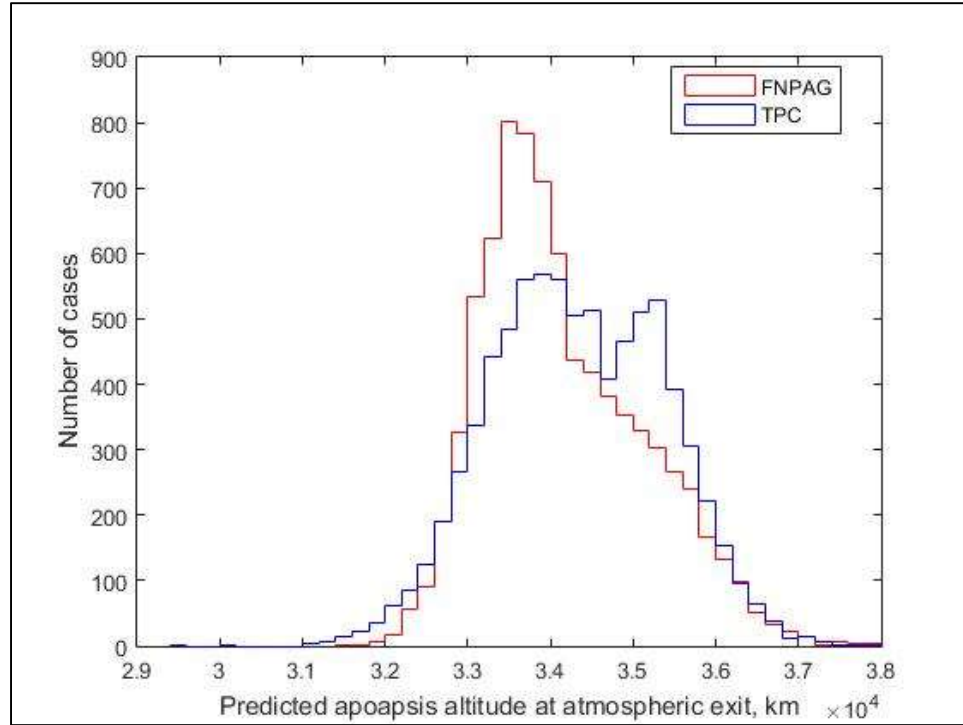
Fig. 5.9. ADEPT histogram of predicted apoapsis altitudes, 1-sol orbit.

The last variable we will delve into is the predicted periapsis altitude at atmospheric exit. This is the periapsis altitude that the vehicle would reach after passing through apoapsis if a periapsis raise burn were not to occur. When the vehicle exits the atmosphere, its trajectory is such that it will re-enter the atmosphere and potentially crash into the surface. To raise the final periapsis altitude to the target of 250 km, a burn must be carried out at apoapsis. Clearly, from Table 5.4 and Fig. 5.10, FNPAG has a higher predicted periapsis altitude at atmospheric exit. This means that less propellant will be required to raise the periapsis altitude to 250 km, and is another reason for the FNPAG algorithms performance advantage over TPC guidance.

Table 5.4. ADEPT predicted periapsis altitude (km) at atmospheric exit, 1-sol orbit.

	FNPAG	**TPC**
Mean	29.30	22.19
3-sigma	5.47	7.67
Min	22.33	16.22
5.00-percentile	26.00	18.45
50.00-percentile	29.63	21.89
95.00-percentile	31.75	26.60
99.00-percentile	32.30	27.47
Max	33.34	28.63
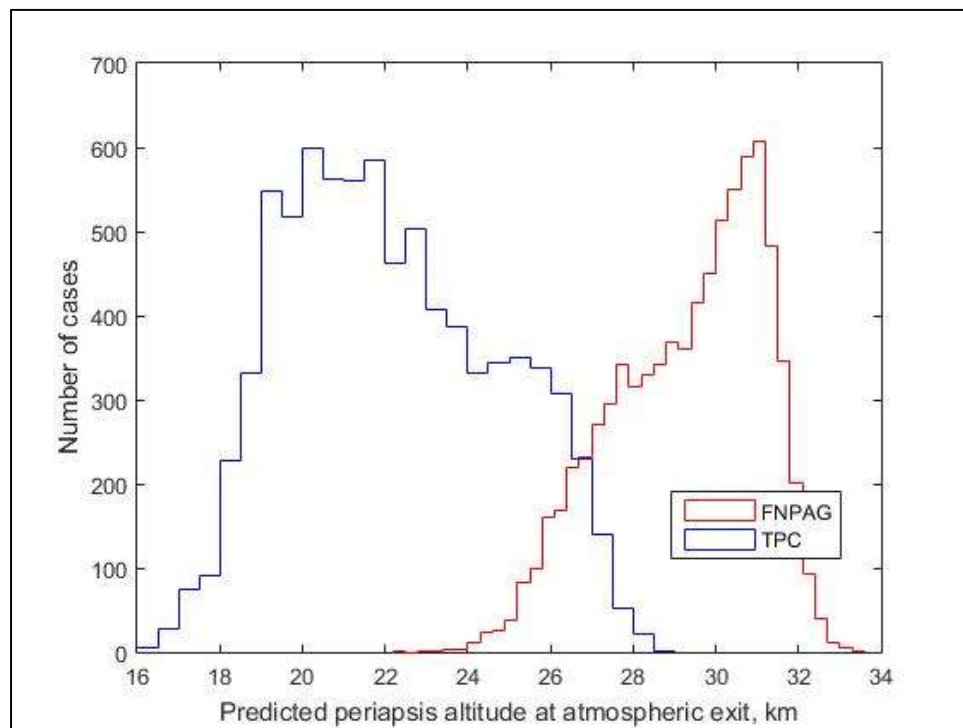
Fig. 5.10. ADEPT histogram of predicted periapsis altitudes, 1-sol orbit.

5.1.3 5-sol nominal results

Because no other algorithms were able to complete Monte Carlo simulations of vehicles other than the ADEPT 1-sol target orbit test case, the 5-sol FNPAG results will be compared with the 1-sol FNPAG results to give insight into the different approaches in finding an optimal solution between the two cases. The 5-sol case used an entry flight path angle of -11.25 degrees and a nominal *dusttau* of 0.45. For the nominal 5-sol orbit, the FNPAG algorithm required a ΔV budget of 7.70 m/s, which is almost 60% less than the requirement to reach the 1-sol orbit. The main reason for this is that the apoapsis altitude of the 5-sol orbit is much larger than the 1-sol, so the propellant cost of the periapsis raise burn applied at the apoapsis is significantly reduced. Figure 5.11 shows the bank angle profiles for the nominal case, with the 1-sol profile in red and the 5-sol profile in blue. Again, this color scheme will be consistent throughout this subsection.
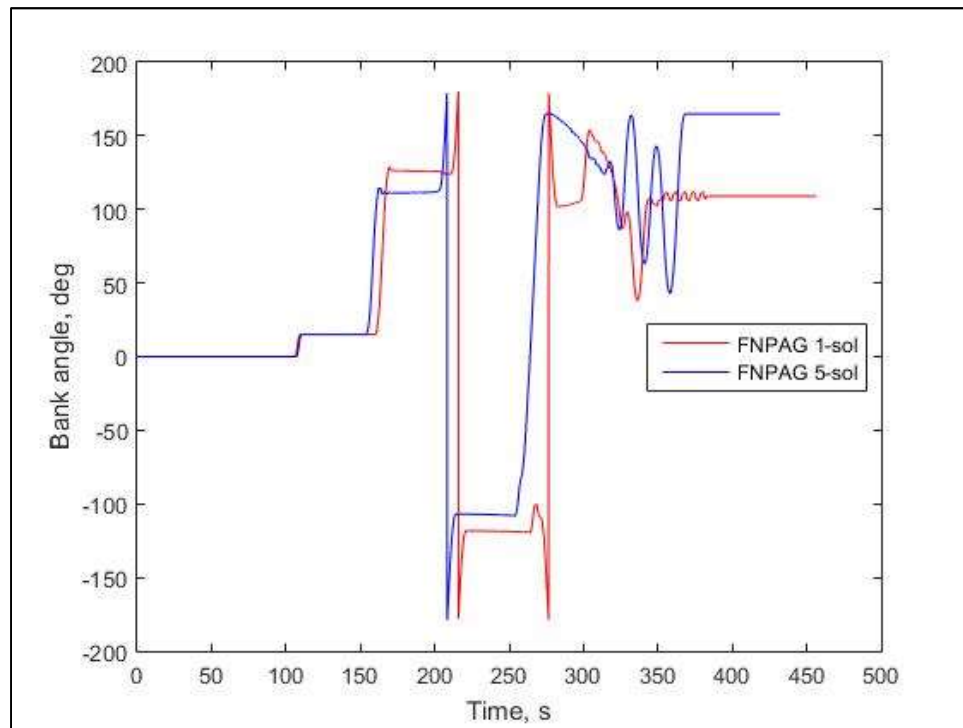
Fig. 5.11. ADEPT nominal bank angle vs. time, 1-sol vs. 5-sol orbit.

The main difference between these two bank angle profiles occurs in the second phase of flight. For targeting the 5-sol orbit, the second phase is flown at a smaller bank angle magnitude. This choice was made to allow for greater robustness when facing trajectory dispersions, as errors in the exit condition tend to have a much more significant effect on algorithm performance for the much larger 5-sol target orbit. If these magnitudes were the same, the 5-sol trajectory case would stay in Phase 1 for longer than the 1-sol trajectory case. However, since Phase 2 is flown at a smaller magnitude here, it is necessary to switch sooner into the flight in order to avoid overshooting the target.

Figures 5.12 and 5.13 show the nominal load and heat rates seen by the vehicle throughout each trajectory. The 5-sol orbit experiences slightly lesser load forces and heat rates than the 1-sol, mostly because it must fly a higher altitude trajectory to conserve energy needed to reach the much higher apoapsis target altitude.
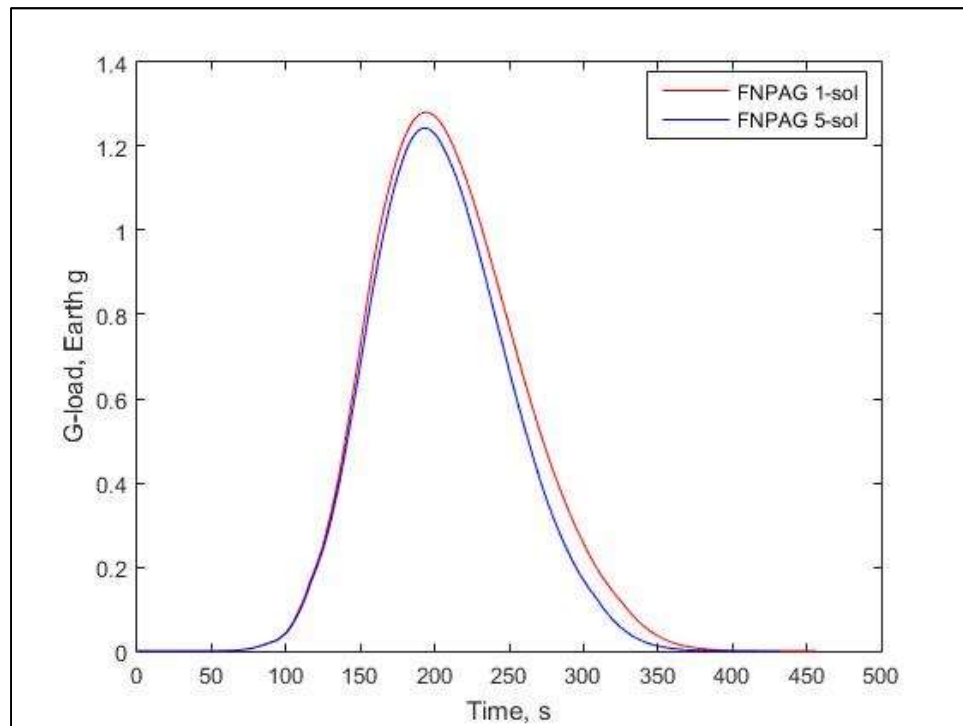
Fig. 5.12. ADEPT nominal g-load vs. time, 1-sol vs. 5-sol orbit.
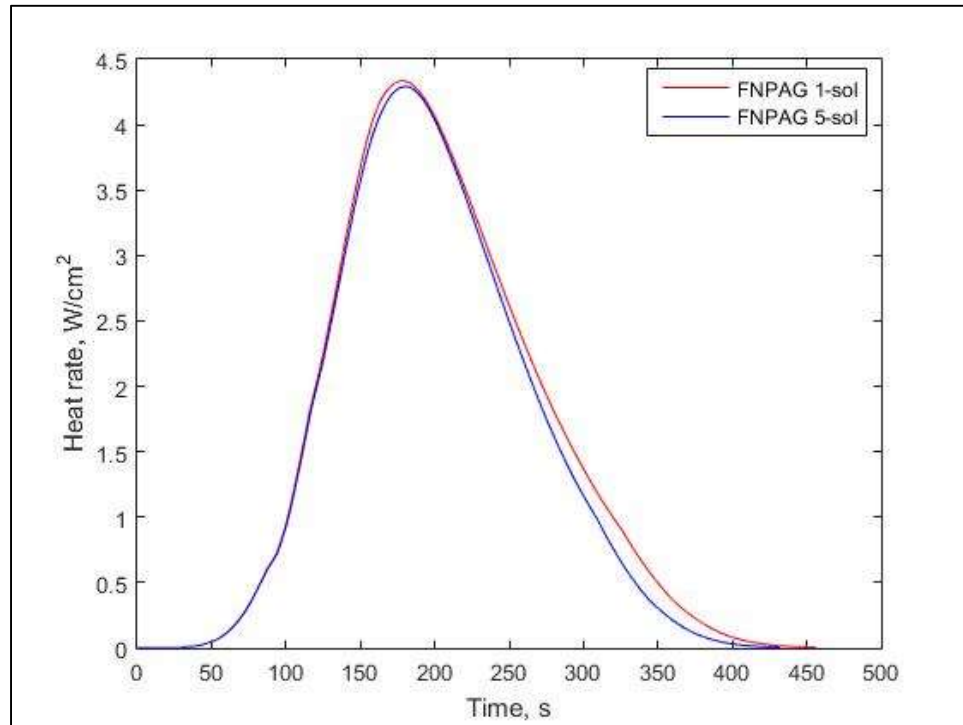
Fig. 5.13. ADEPT nominal heat rate vs. time, 1-sol vs. 5-sol orbit.

Figure 5.14 compares the nominal planetodetic altitude profile for the 1-sol ADEPT test case with the 5-sol case. The 5-sol nominal trajectory has an atmospheric periapsis of just under 46 km, a little less than a kilometer higher than that of the 1-sol. Again, this is because Phase 2 of the 5-sol case flies at a smaller bank angle magnitude than the 1-sol case.
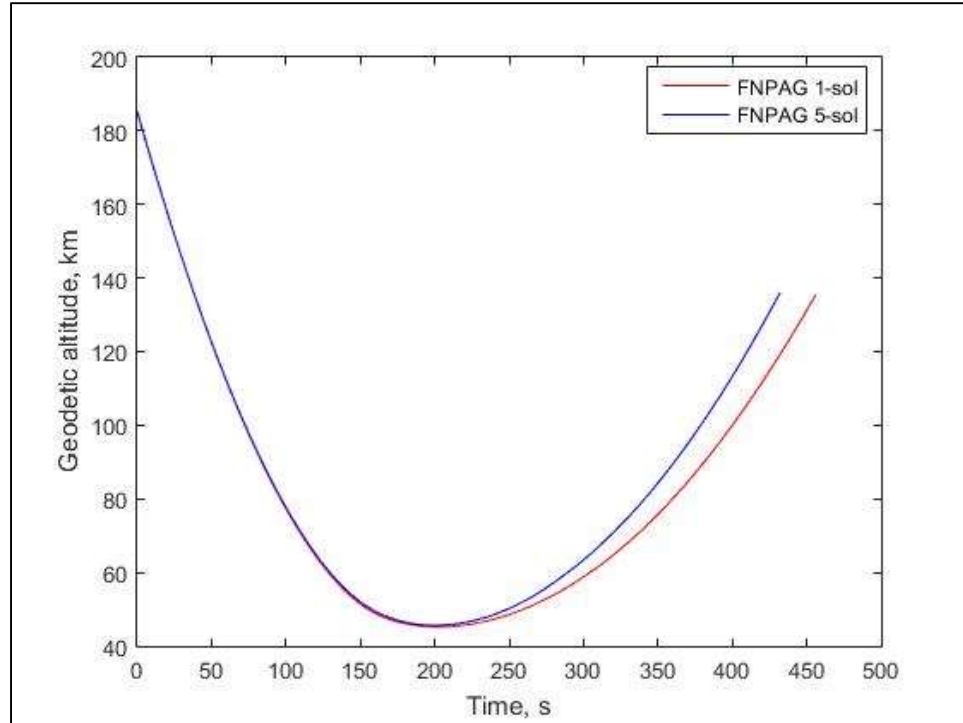
Fig. 5.14. ADEPT planetodetic altitude vs. time, 1-sol vs. 5-sol orbit.

Another effect of this bank angle difference is that the vehicle spends less time in the atmosphere for the 5-sol case, reaching the exit interface about 25 seconds before the 1-sol case. This allows it to exit the atmosphere at a higher velocity and a slightly larger flight path angle, as seen in Figs. 5.15 and 5.16, respectively. The extra velocity and steeper exit flight path angle are crucial for reaching the much higher final apoapsis altitude of the 5-sol target orbit.
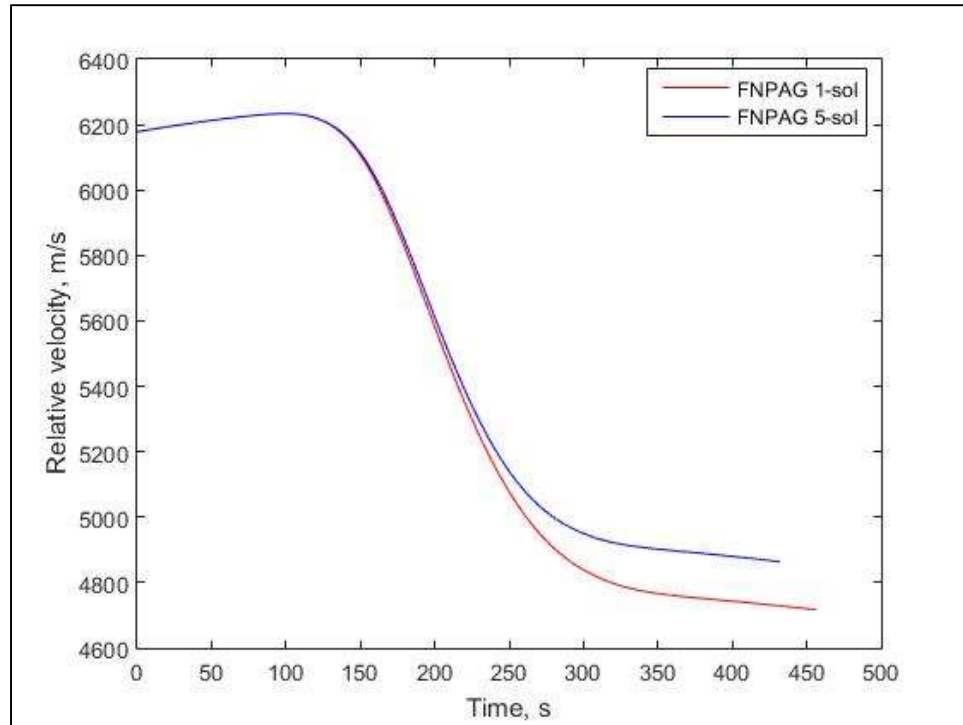
Fig 5.15. ADEPT relative velocity vs. time, 1-sol vs. 5-sol orbit.
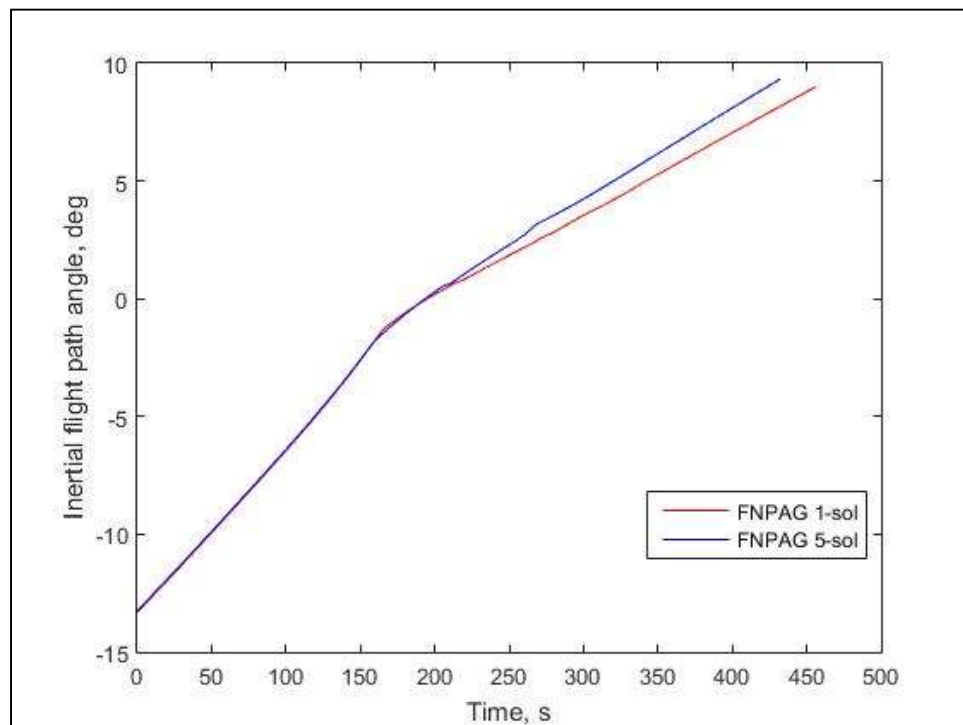
Fig. 5.16. ADEPT inertial flight path angle vs. time, 1-sol vs. 5-sol orbit.

5.1.4 5-sol Monte Carlo results

Once again, results are unavailable for the ADEPT vehicle and the 1-sol target orbit, so we will use the FNPAG 1-sol orbit results as a basis for comparison for the 5-sol target orbit results. We begin with the 99th percentile value of the total ΔV budget, as seen in Table 5.5. The 5-sol profiles had a 99th propellant requirement of 21.12 m/s, a reduction of about 30% compared to the 1-sol. However, the mean ΔV requirement of the 5-sol orbit is 57% less than that of the 1-sol, and the maximum propellant cost of the 5-sol is actually higher than that of the 1-sol. This is because it is inherently more difficult to reach a high energy target orbit from a low energy entry condition. Since the target apoapsis altitude is so large, any small errors at the exit interface have a much larger effect on algorithm performance than they do for lower energy targets such as the 1-sol orbit. This difficulty is reflected in the spread of the histograms in Fig. 5.17.

Table 5.5. Total ΔV required (m/s), 1-sol target orbit vs. 5-sol target orbit.

	FNPAG 1-sol	FNPAG 5-sol
Mean	21.21	12.07
3-sigma	9.32	9.86
Min	14.16	5.82
5.00-percentile	17.09	7.61
50.00-percentile	20.67	11.67
95.00-percentile	26.98	17.87
99.00-percentile	29.91	21.12
Max	36.50	43.07
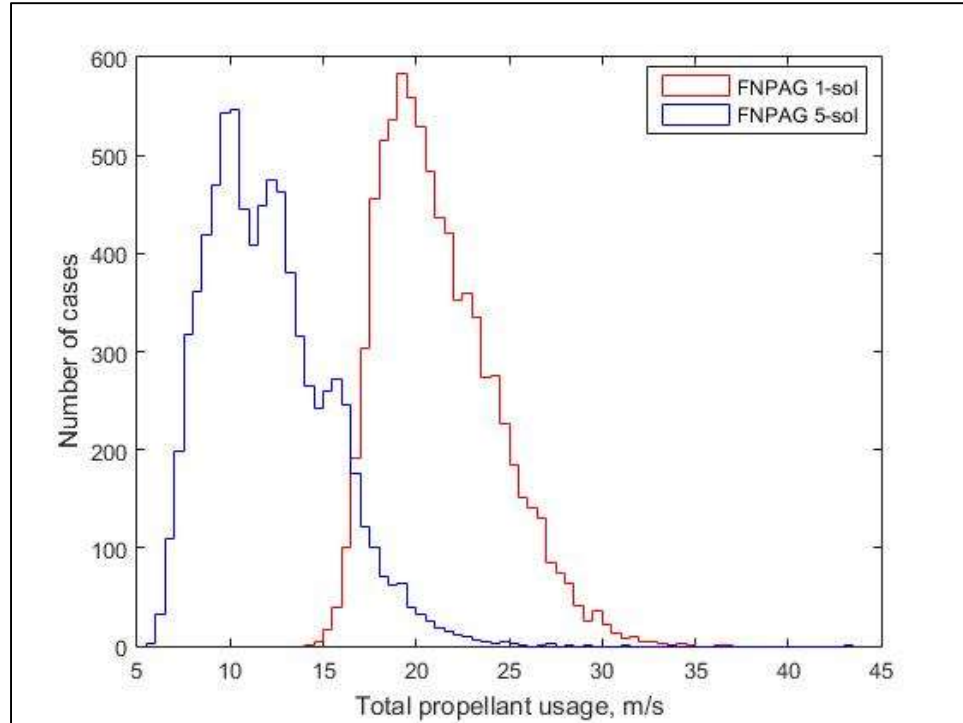
Fig. 5.17. ADEPT histogram of ΔV performance, 1-sol vs. 5-sol orbit.

First, we will examine the planetodetic periapsis altitude from the atmospheric flight for each test case, where the periapsis raise burn occurs. From Table 5.6 and Fig. 5.18, it is apparent that the 5-sol orbit profiles maintain a slightly higher periapsis altitude. This makes sense intuitively, since they need to bleed less energy to reach their target orbits.

Table 5.6. Periapsis altitude (km) for aerocapture trajectory, 1-sol vs. 5-sol target orbit.

	FNPAG 1-sol	FNPAG 5-sol
Mean	45.28	45.77
3-sigma	2.14	2.31
Min	43.44	44.06
5.00-percentile	44.12	44.53
50.00-percentile	45.37	45.87
95.00-percentile	46.31	46.86
99.00-percentile	46.54	47.07
Max	47.01	47.55
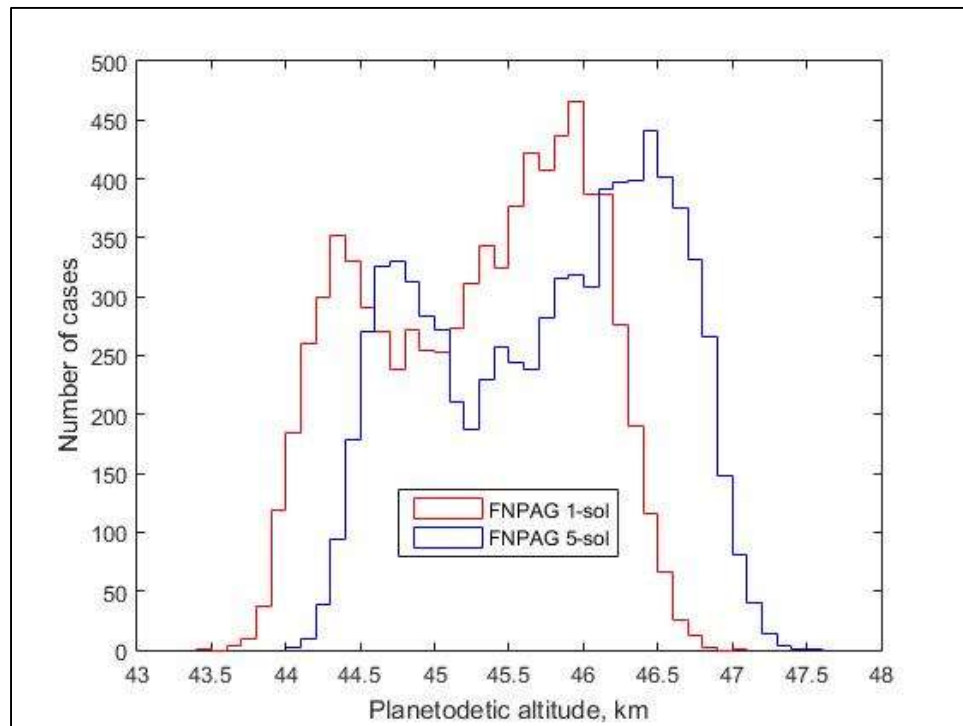
Fig. 5.18. ADEPT histogram of periapsis altitudes, 1-sol vs. 5-sol orbit.

Again, we will compare the predicted apoapsis altitude at atmospheric exit to shed light on the differences in algorithm performance. From Table 5.7 and Fig. 5.19, it is immediately apparent that there is a much wider error band for the 5-sol target orbit than the 1-sol. This highlights the effect that small errors in the vehicle state caused by dispersions has a much more pronounced effect on the 5-sol orbit. In fact, the worst-case trajectory overshoots the target apoapsis by over 100,000 km! However, the high energy orbit also means that correction burns are much less expensive. An apoapsis error of over 100,000 km vs. the 1-sol error of around 4,000 km only leads to a ΔV increase of about 7 m/s.

Table 5.7. Predicted apoapsis altitude (km) at exit interface, 1-sol vs. 5-sol target orbit.

	FNPAG 1-sol	FNPAG 5-sol
Mean	34154.65	115290.41
3-sigma	2923.60	27512.84
Min	31486.97	89911.79
5.00-percentile	32821.74	103399.20
50.00-percentile	33954.24	113399.30
95.00-percentile	35939.81	132083.79
99.00-percentile	36609.10	139323.42
Max	37939.77	234796.53
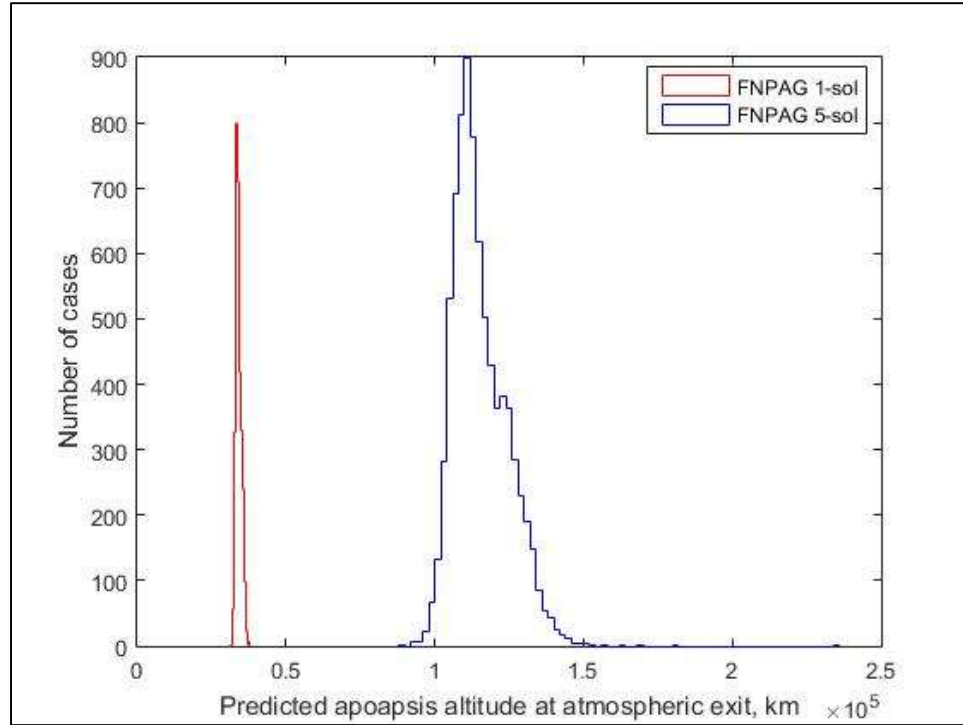
Fig. 5.19. ADEPT histogram of predicted apoapsis altitudes, 1-sol vs. 5-sol orbit.

The last variable we will compare and contrast is the predicted periapsis altitude at atmospheric exit, as shown in Table 5.8 and Fig. 5.20. Surprisingly enough, these values are almost identical. Despite the large difference in apoapsis altitudes, both the 1-sol and 5-sol profiles risk capture and crashing into the surface if a periapsis raise maneuver is not performed. However, even though the periapsis is raised to 250 km in both cases, the cost of conducting a correction burn at 112,400 km is much less than performing the burn at 33,793 km. This is the driving force behind the cost reduction of exiting into a 5-sol orbit when compared to a 1-sol final orbit.

Table 5.8. Predicted periapsis altitude (km) at exit interface, 1-sol vs. 5-sol target orbit.

	FNPAG 1-sol	FNPAG 5-sol
Mean	29.30	28.50
3-sigma	5.47	4.80
Min	22.33	23.17
5.00-percentile	26.00	25.68
50.00-percentile	29.63	28.71
95.00-percentile	31.75	30.74
99.00-percentile	32.30	31.33
Max	33.34	32.51
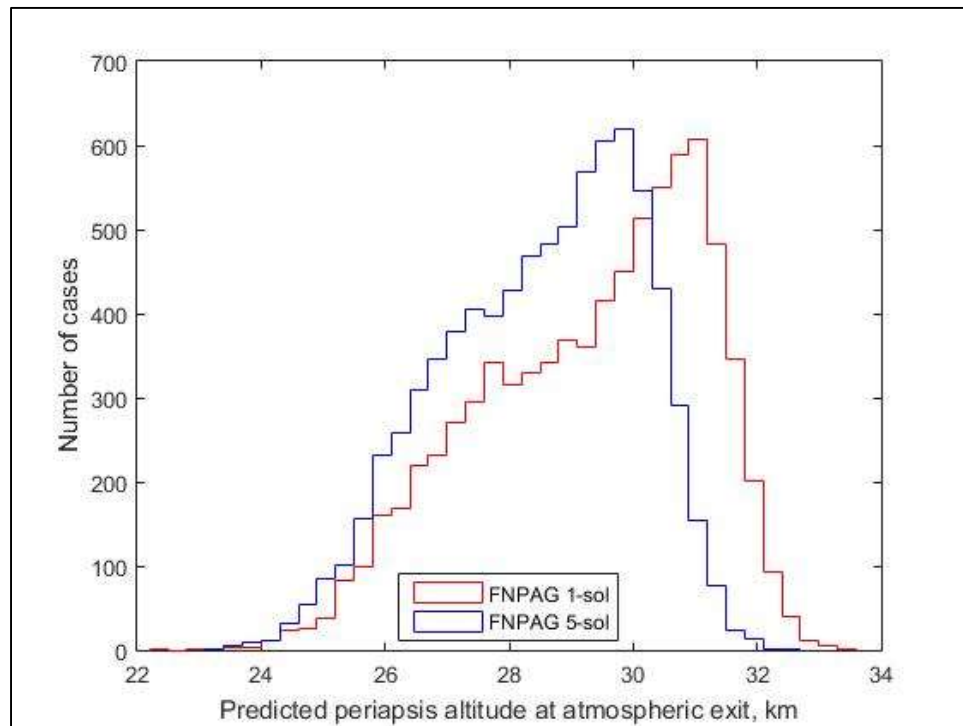
Fig. 5.20. ADEPT histogram of predicted periapsis altitudes, 1-sol vs. 5-sol orbit.

5.2 HIAD Simulation Results

The HIAD vehicle is slightly more massive than the ADEPT vehicle, and has a slightly lower lift-to-drag ratio, coming in at 0.2 instead of 0.27. The inertial entry flight path angle was chosen to be -11.12 degrees for the 1-sol target orbit, and a slightly shallower -11.07 degrees for the 5-sol target orbit. The 1-sol Monte Carlo trajectories were run using a *dusttau* value passed to FNPAG of 0.45, while the 5-sol trajectories used a *dusttau* value of 0.4.

5.2.1 HIAD nominal results

Since no other algorithm data is available for the HIAD simulations, and in the interest of saving paper, the 1-sol and 5-sol HIAD results will be presented together and used in a comparison to highlight the differences between the orbits. For the nominal case, the 1-sol HIAD required a ΔV of 15.64 m/s to reach the target orbit, while the 5-sol case required about half as much propellant, coming in at 7.41 m/s. A comparison of the bank angle profiles can be seen in Fig. 5.21. From the figure it is apparent that the 5-sol nominal case switches to Phase 2 earlier than the 1-sol case. This is because the 5-sol case enters the atmosphere at a shallower flight path angle, and must switch to lift-down flight to avoid overshooting the target orbit.
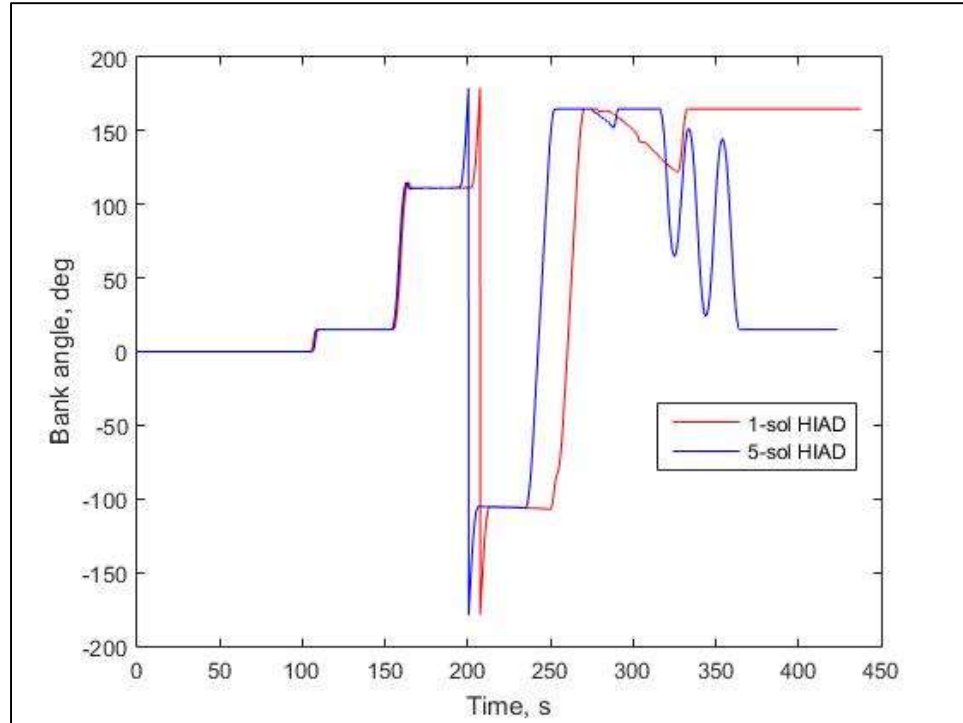
Fig. 5.21. Nominal bank angle vs. time, HIAD.

The next variables to consider are the load factor and heating rate applied to the HIAD vehicle throughout the trajectory. These values are shown in Fig. 5.22 and Fig. 5.23 below. It is clear from these figures that the 5-sol trajectory is subjected to lower loads and lower heat rates than the 1-sol orbit. This is most likely because the shallower 5-sol trajectory tends not to dive as deep into the Martian atmosphere as the steep 1-sol trajectory does.
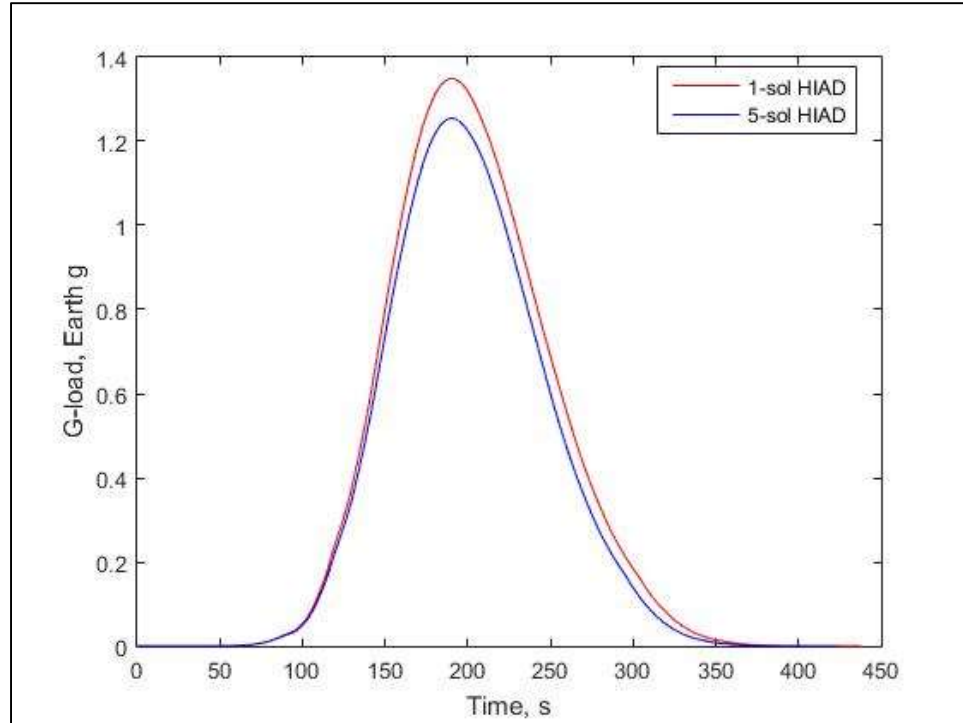
Fig 5.22. HIAD nominal g-load vs. time.
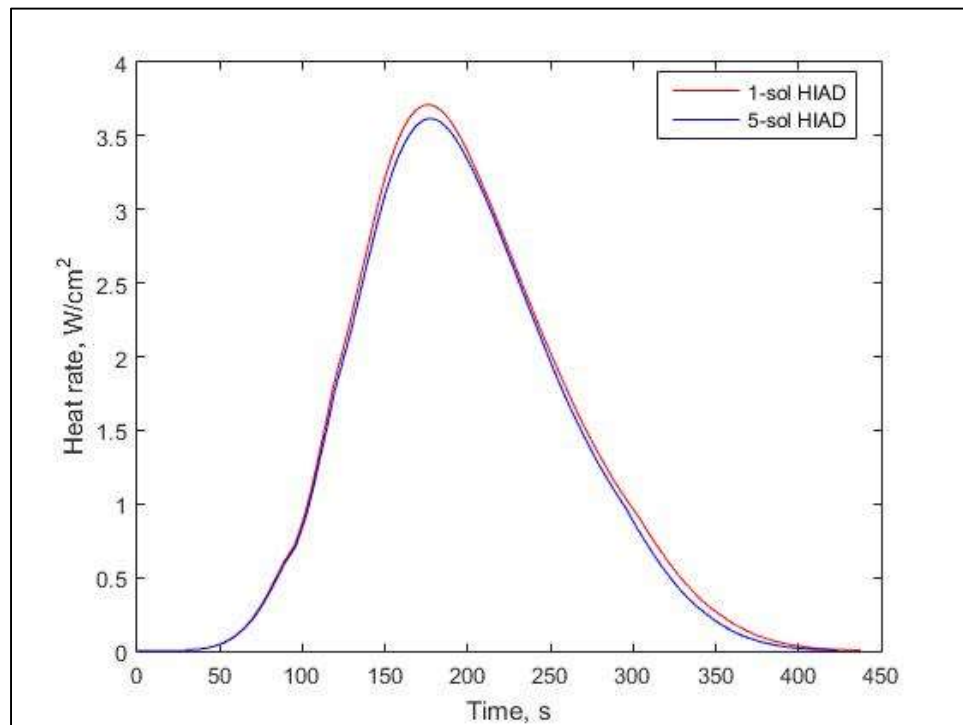
Fig. 5.23. HIAD nominal heat rate vs. time.

Figure 5.24 displays the nominal planetodetic altitude profile for both the 1-sol and 5-sol trajectories, while Figure 5.25 shows their respective relative velocity profiles. We can in fact see that the 5-sol orbit remains higher in the atmosphere than the 1-sol nominal orbit, as was indicated by the load and heat rates on the vehicle. The 5-sol target case also has a shorter trajectory, which allows it to exit at the higher velocity needed to reach a much larger apoapsis altitude. The final nominal plot, Fig. 5.26, shows that the 5-sol trajectory exits the atmosphere at a slightly shallower flight path angle than the 1-sol trajectory.
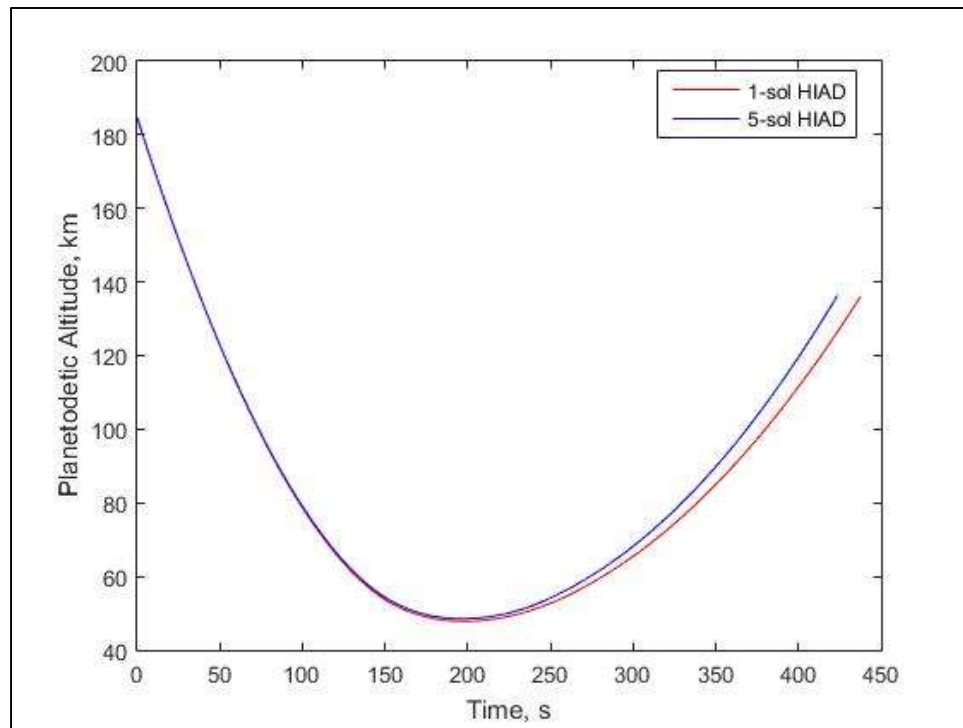
Fig 5.24. HIAD planetodetic altitude vs. time.
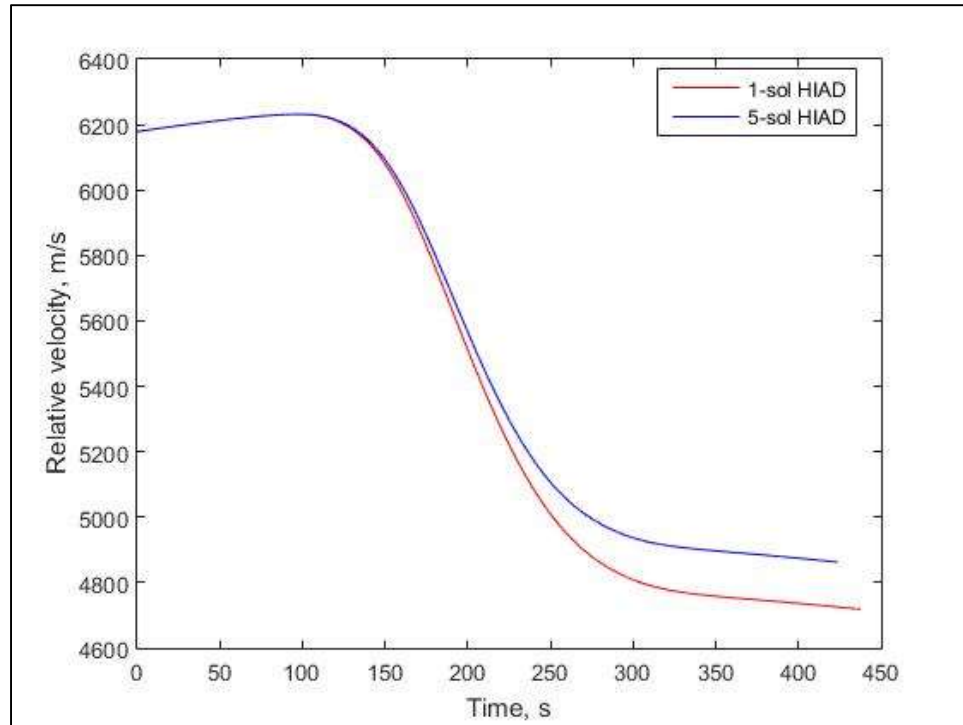
Fig. 5.25. HIAD relative velocity vs. time.
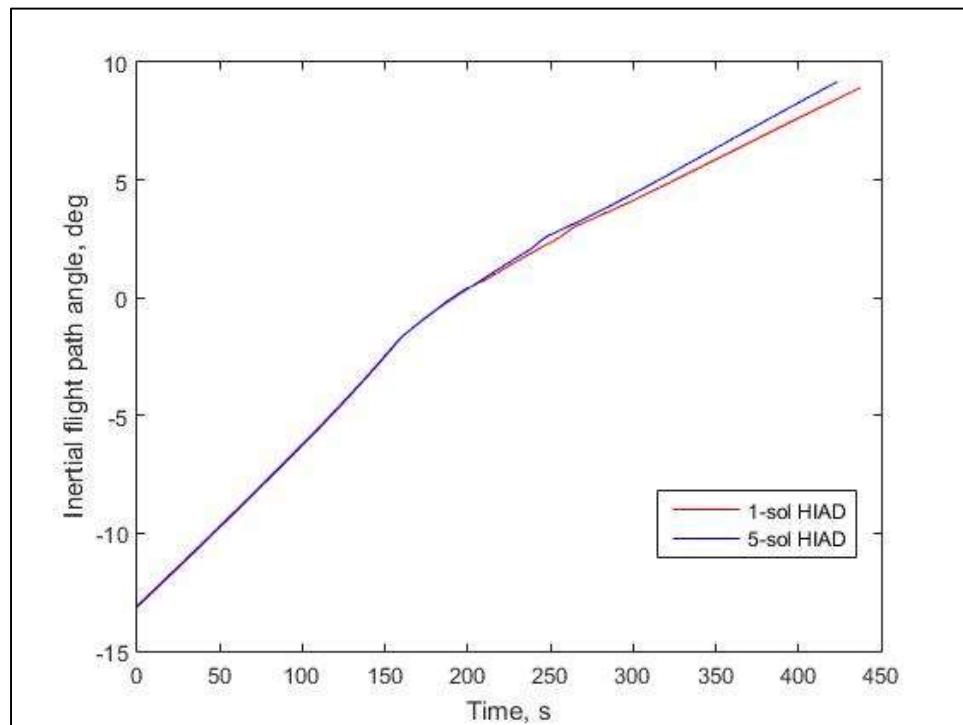
Fig. 5.26. HIAD inertial flight path angle vs. time.

5.2.2 HIAD Monte Carlo results

     As was the case with the ADEPT simulations, the HIAD vehicle was tested using 8,000 dispersed trajectories for each target orbit. Similar statistics will be analyzed for HIAD to provide a basis for comparison between the two vehicles. The figure of merit used will once again be the 99th percentile value of the total ΔV requirement to reach the desired target orbit. For additional comparison benefits, the 1-sol results will be compared side-by-side with the 5-sol trajectories, as can be seen in Table 5.9 and in Fig. 5.27. As expected, the 5-sol target orbit displays an approximately 25% reduction in required ΔV. Unlike the ADEPT case, however, the worst 5-sol case is still better than the worst 1-sol case.

Table 5.9. HIAD total ΔV required (m/s), 1-sol vs. 5-sol target orbit.

	HIAD 1-sol	**HIAD 5-sol**
Mean	20.47	10.87
3-sigma	10.77	11.79
Min	13.28	4.39
5.00-percentile	15.86	5.93
50.00-percentile	19.91	10.07
95.00-percentile	27.10	18.32
99.00-percentile	30.62	22.77
Max	45.26	36.81
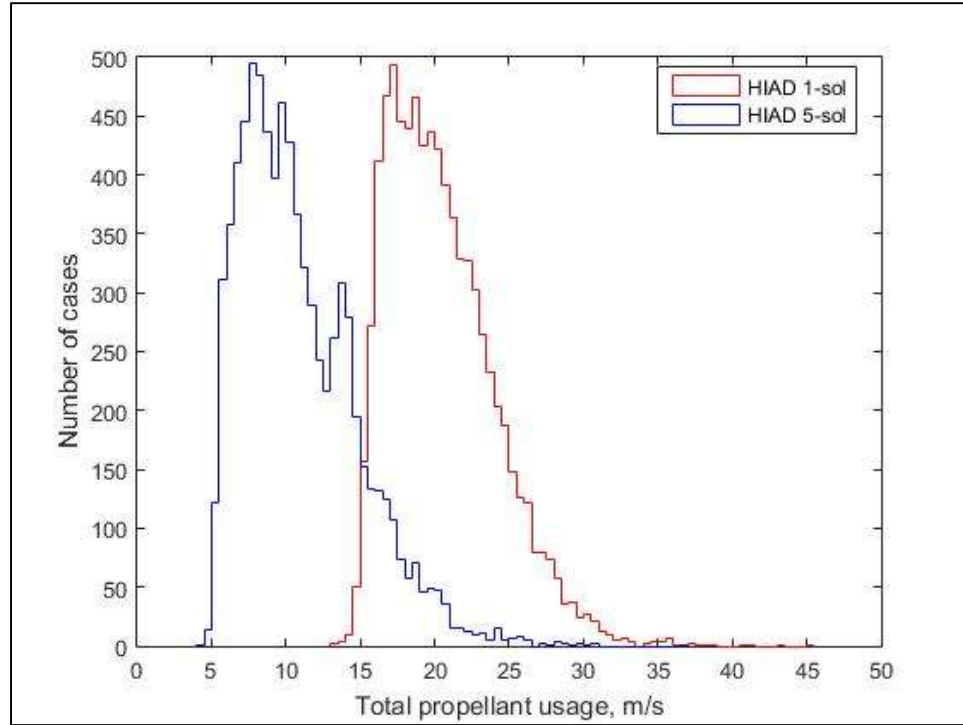
Fig. 5.27. Histogram of ΔV performance, HIAD 1-sol vs. 5-sol target orbit.

From Table 5.10 and Fig. 5.28, it can be seen that the 5-sol orbit cases have a higher periapsis altitude than the 1-sol orbit cases. Additionally, the HIAD cases have higher periapsis altitudes than the corresponding 1-sol and 5-sol ADEPT cases. This is likely due to the lower lift-to-drag ratio of the HIAD vehicle compared to the ADEPT vehicle, as it experiences larger drag accelerations at the same altitudes.

Table 5.10. HIAD periapsis altitude (km) for trajectory, 1-sol vs. 5-sol target orbit.

	HIAD 1-sol	**HIAD 5-sol**
Mean	47.96	48.82
3-sigma	2.49	2.50
Min	46.09	46.91
5.00-percentile	46.62	47.46
50.00-percentile	48.09	48.95
95.00-percentile	49.12	49.99
99.00-percentile	49.36	50.24
Max	49.80	50.84
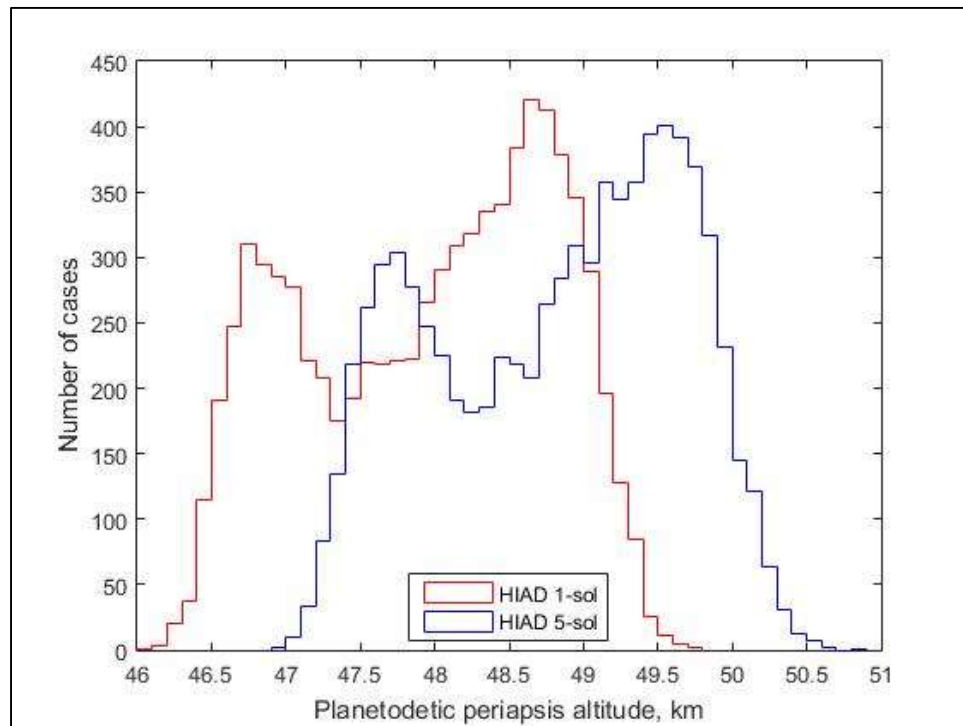
Fig. 5.28. Histogram of HIAD periapsis altitudes, 1-sol vs. 5-sol target orbit.

The next step in analyzing the results is comparing the predicted apoapsis altitude at atmospheric exit for the 1-sol and 5-sol target orbit cases. These data can be seen in Table 5.11 and Fig. 5.29. Once again, the 5-sol cases have a larger spread of apoapsis error. However, although the maximum altitude for the 1-sol case is actually farther off than the corresponding maximum for the ADEPT vehicle, the HIAD 5-sol maximum altitude is actually closer to the target than the ADEPT 5-sol case. This is why the worst case scenario for the 5-sol HIAD in terms of propellant consumption is still better than the worst case scenario for the 1-sol HIAD case.

Table 5.11. HIAD predicted apoapsis altitude (km) at exit, 1-sol vs. 5-sol target orbit.

	HIAD 1-sol	HIAD 5-sol
Mean	34102.50	113832.12
3-sigma	3280.31	31476.36
Min	30792.89	85883.26
5.00-percentile	32543.69	99914.77
50.00-percentile	33920.74	112047.99
95.00-percentile	36076.72	132903.91
99.00-percentile	36921.03	146381.21
Max	40314.59	215775.86
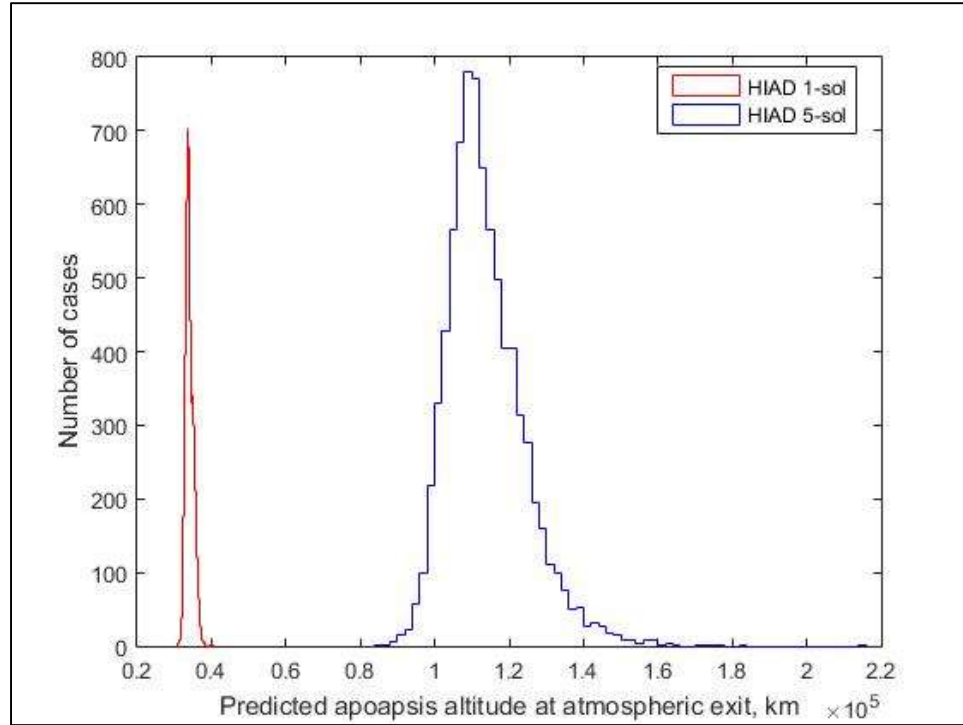
Fig. 5.29. Histogram of HIAD predicted apoapsis altitudes, 1-sol vs. 5-sol target orbit.

The last variable to gain insight on the performance of the FNPAG algorithm is the predicted periapsis altitude at atmospheric exit, shown in Table 5.12 and Fig. 5.30. Again, these values come out remarkably similar, with the 5-sol cases having a slightly higher predicted periapsis altitude. And like the atmospheric flight periapsis, the HIAD displays a higher predicted periapsis altitude than the corresponding ADEPT test cases, although the values are still quite close.

Table 5.12. HIAD predicted periapsis altitude (km) at exit, 1-sol vs. 5-sol target orbit.

	HIAD 1-sol	HIAD 5-sol
Mean	30.32	30.78
3-sigma	4.59	4.19
Min	24.99	26.35
5.00-percentile	27.63	28.43
50.00-percentile	30.51	30.87
95.00-percentile	32.52	32.92
99.00-percentile	33.20	33.67
Max	34.27	36.47
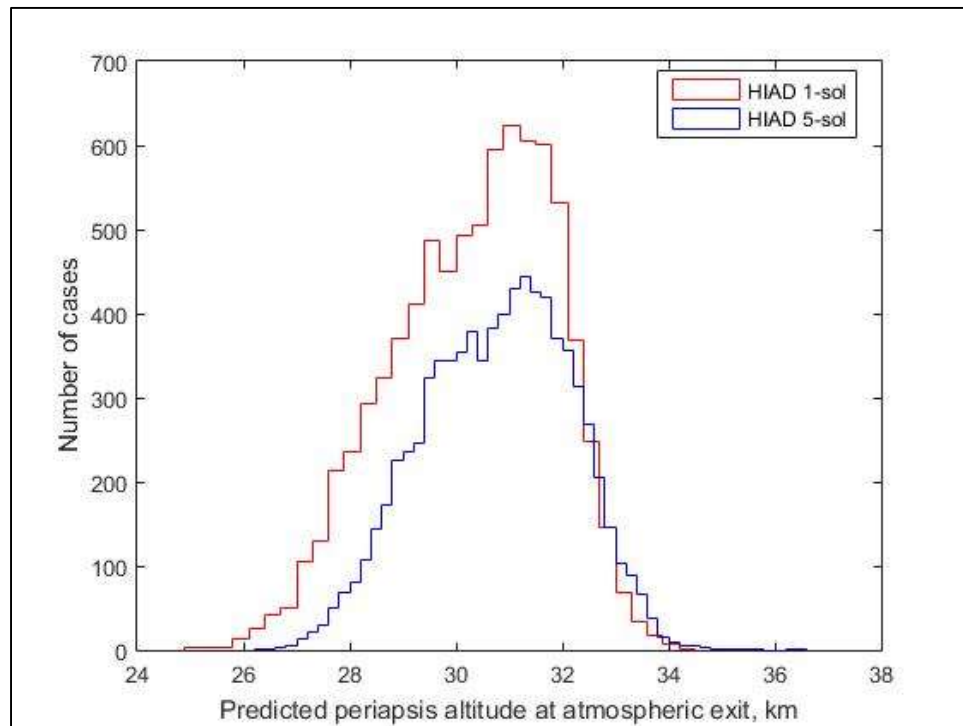
Fig. 5.30. Histogram of HIAD predicted periapsis altitudes, 1-sol vs. 5-sol target orbit.

5.3 Mid-L/D Simulation Results

The final vehicle that was used to test the capabilities of the FNPAG algorithm was the Mid-L/D rigid aeroshell. Although this vehicle has a similar mass of 60,000 kg, it has a much higher lift-to-drag ratio than the HIAD or ADEPT vehicles. Because of this, the aeroshell is a perfect vehicle to showcase the versatility of the FNPAG algorithm. For these simulations, the Mid-L/D vehicle used an inertial entry flight path angle of -12.4 degrees for the 1-sol target orbit and -11.7 degrees for the 5-sol target orbit. Both suites of trajectories were run with the internal FNPAG *dusttau* value set at 0.525, slightly higher than the HIAD and ADEPT cases.

5.3.1 Mid-L/D nominal results

The 1-sol and 5-sol results for the mid-lift-to-drag ratio aeroshell will be presented concurrently and compared both between each other and against the HIAD and ADEPT results. For the nominal case, the 1-sol Mid-L/D vehicle needed a ΔV of 20.81 m/s to reach the final target orbit, while the 5-sol trajectory required 17.51 m/s. The majority of the ΔV budget for these cases was utilized to perform the wedge angle correction burn, the cause of which will be discussed in Section 5.4. In this case the 5-sol nominal trajectory switches to Phase 2 after the 1-sol case, implying that the guidance is trying to preserve enough energy to reach the higher apoapsis target.
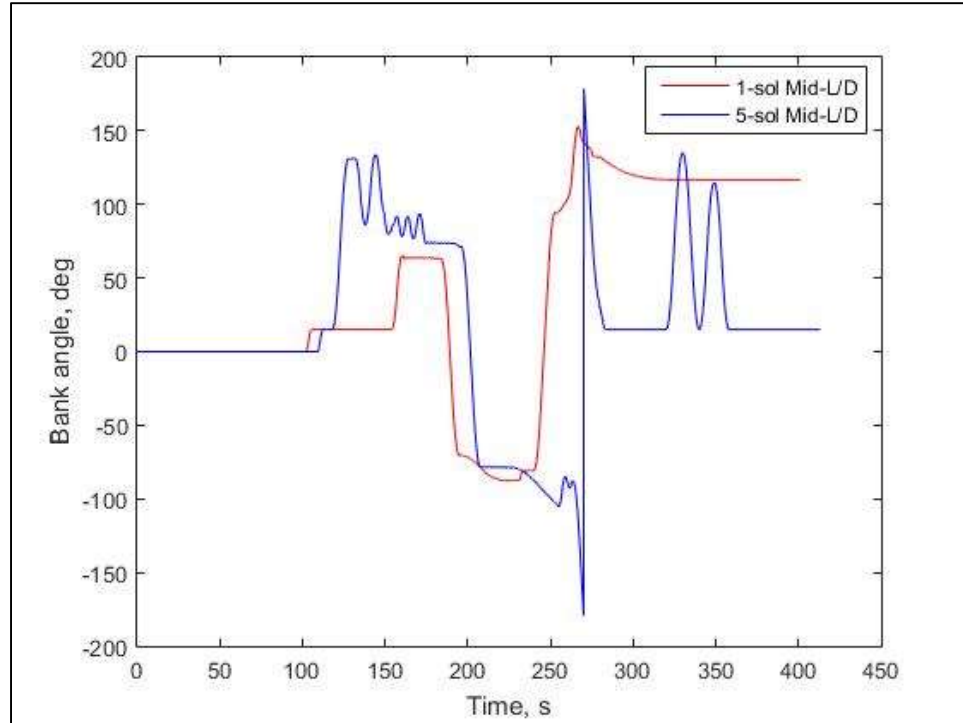
Fig. 5.31. Nominal bank angle vs. time, Mid-L/D.

The next variables presented are the load factor and heating rates, shown in Fig. 5.32 and Fig. 5.33, respectively. It can be seen that the 1-sol nominal profile experiences higher maximum g-loads and heat rates than the 5-sol, and both profiles undergo higher loads and rates than the 1-sol HIAD or ADEPT. This occurs because the aeroshell vehicle experiences a larger lift acceleration at a given altitude than the other, lower lift-to-drag ratio vehicles.
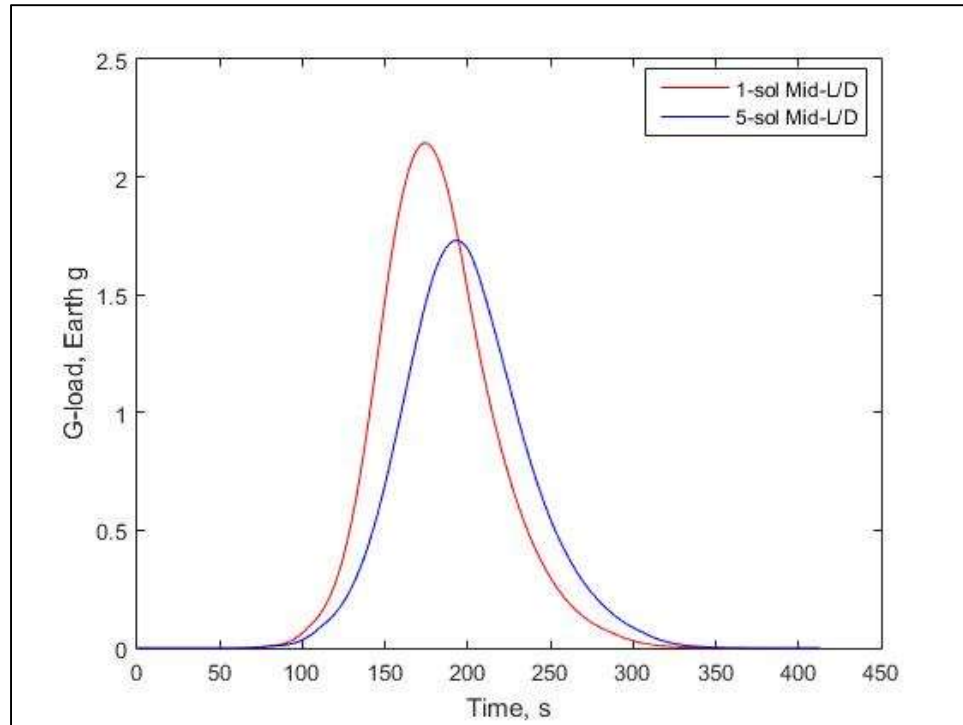
Fig. 5.32. Nominal g-load vs. time, Mid-L/D.
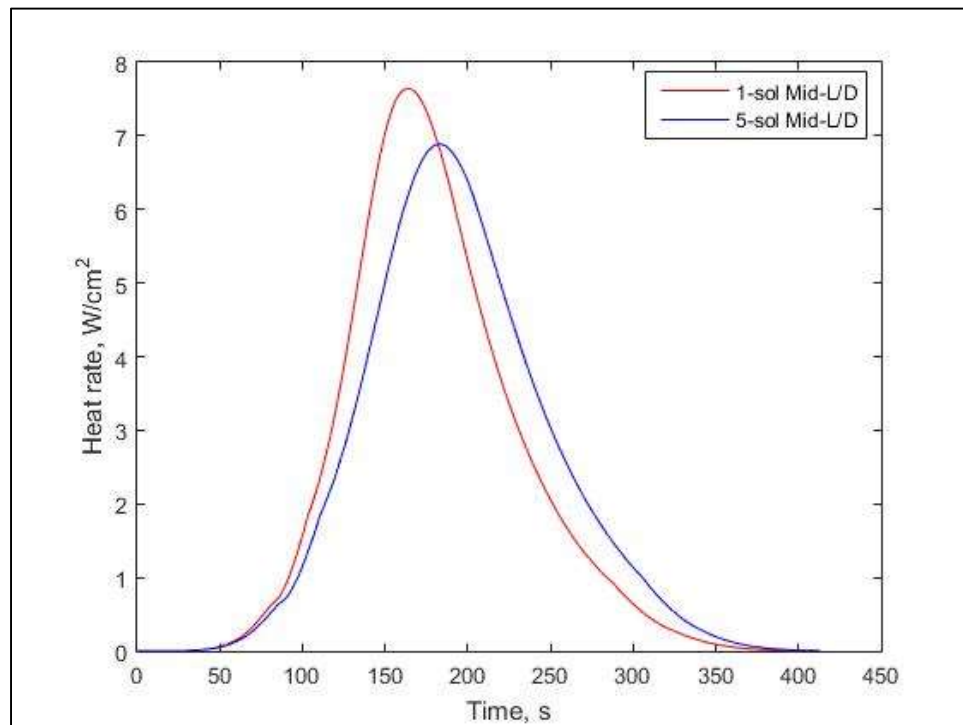
Fig. 5.33. Nominal heat rate vs. time, Mid-L/D.

Fig. 5. 34 shows the nominal planetodetic altitude profile for each of the 1-sol and 5-sol trajectories, and Fig. 35 shows their respective relative velocity profiles. The 5-sol trajectory maintains a slightly higher trajectory until periapsis, and then flattens out into a longer trajectory until exit, which occurs at a higher velocity to reach the higher apoapsis demanded by the 5-sol target orbit. In addition, like the HIAD and ADEPT cases, the Mid-L/D vehicle exits with a slightly shallower flight path angle for the 5-sol trajectory than the 1-sol case, as seen in Fig. 5.36.
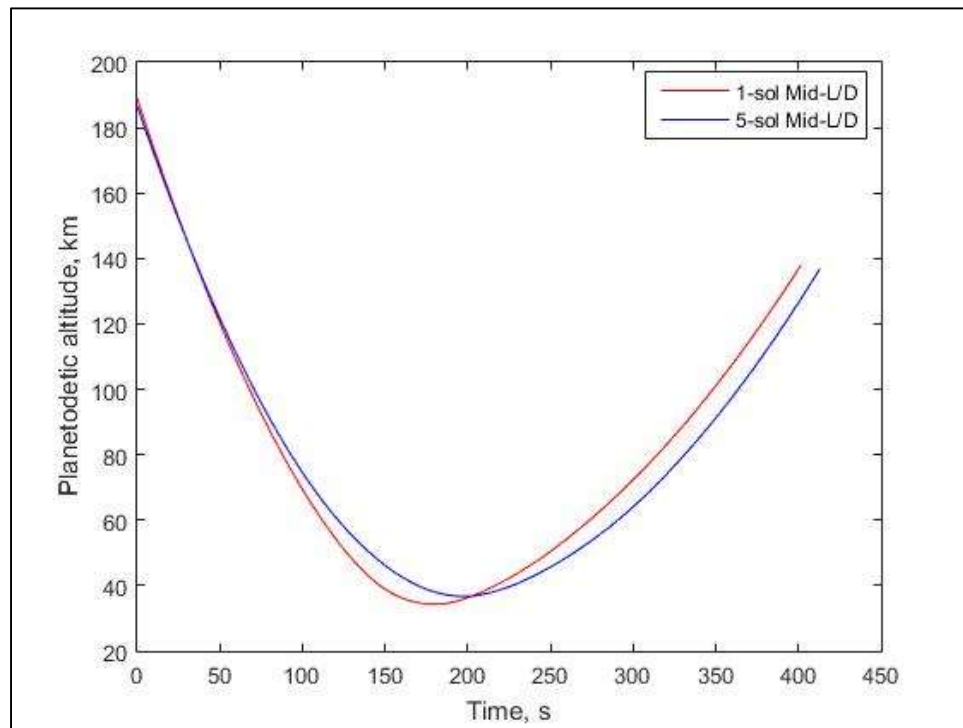
Fig. 5.34. Nominal planetodetic altitude vs. time, Mid-L/D.
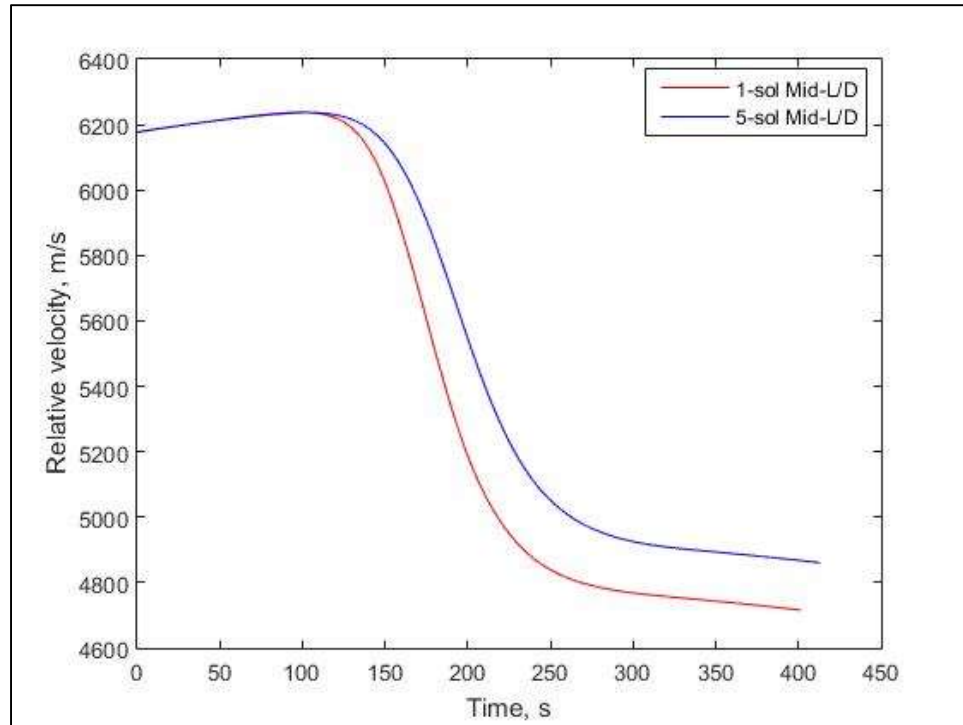
Fig. 5.35. Nominal relative velocity vs. time, Mid-L/D.
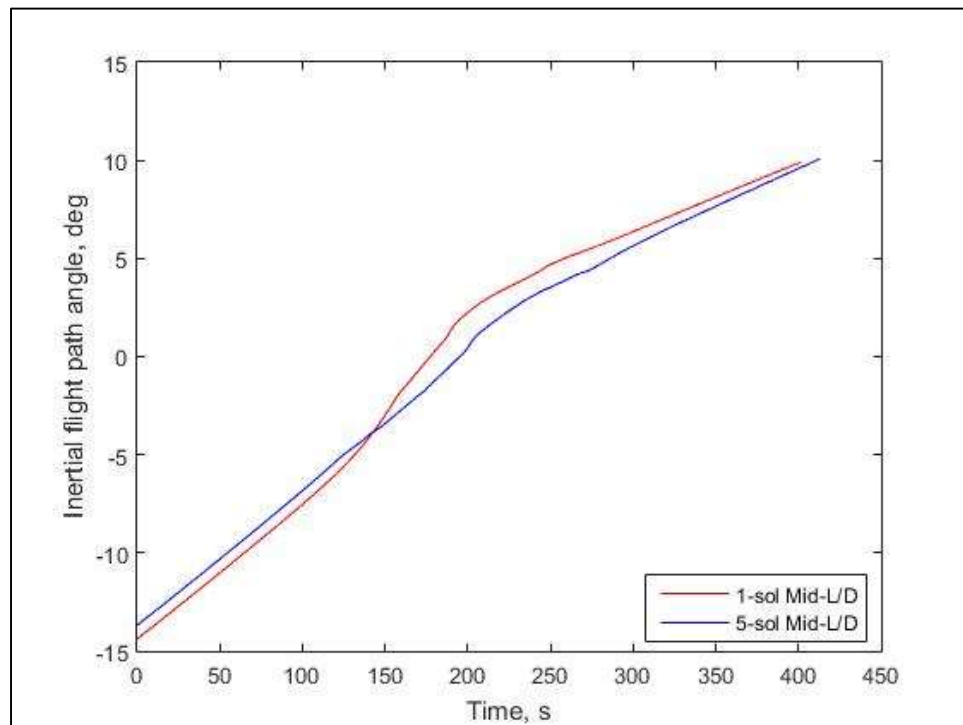
Fig. 5.36. Nominal inertial flight path angle vs. time, Mid-L/D.

5.3.2 Mid-L/D Monte Carlo results

The Mid-L/D Monte Carlo simulations were run in the same manner as the ADEPT and HIAD test suites. A similar set of figures will be developed to compare and contrast the results from the three spacecraft. Again, the 1-sol results will be presented concurrently with the 5-sol trajectories to examine the different approaches each entails. Table 5.13 and Fig. 5.37 contain the data on the 99th percentile ΔV performance of the Mid-L/D vehicle. These numbers are slightly higher than the performance of the HIAD and ADEPT vehicles, although they are still reasonably low. Like the HIAD trajectories, the worst 5-sol case is better in terms of ΔV minimization than the worst 1-sol case.

Table 5.13. Mid-L/D total ΔV required (m/s), 1-sol vs. 5-sol target orbit.

	Mid-L/D 1-sol	**Mid-L/D 5-sol**
Mean	24.88	14.80
3-sigma	10.12	13.41
Min	16.58	5.09
5.00-percentile	20.21	7.62
50.00-percentile	24.53	14.91
95.00-percentile	30.74	22.00
99.00-percentile	33.57	24.82
Max	57.29	54.05
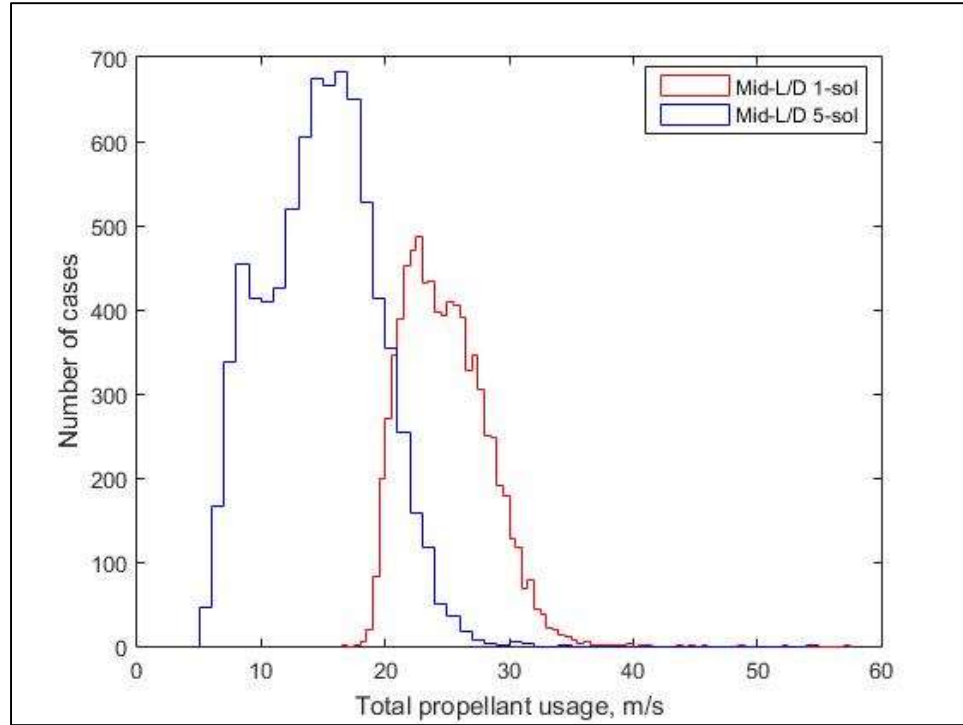
Fig. 5.37. Histogram of ΔV performance, Mid-L/D 1-sol vs. 5-sol target orbit.

Table 5.14 and Fig. 5.38 contain data on the atmospheric flight periapsis altitude. Although the periapsis altitudes of the 5-sol trajectories are higher than those of the 1-sol cases, they are still both much lower than either the HIAD or the ADEPT cases. Since the Mid-L/D vehicle has a much higher lift-to-drag ratio, it must fly lower in the atmosphere to dissipate the energy necessary to reach its target.

Table 5.14. Mid-L/D periapsis altitude (km) for trajectory, 1-sol vs. 5-sol target orbit.

	Mid-L/D 1-sol	Mid-L/D 5-sol
Mean	34.42	36.70
3-sigma	0.79	1.49
Min	33.58	35.27
5.00-percentile	34.00	35.85
50.00-percentile	34.42	36.67
95.00-percentile	34.85	37.55
99.00-percentile	35.05	37.83
Max	35.74	42.12
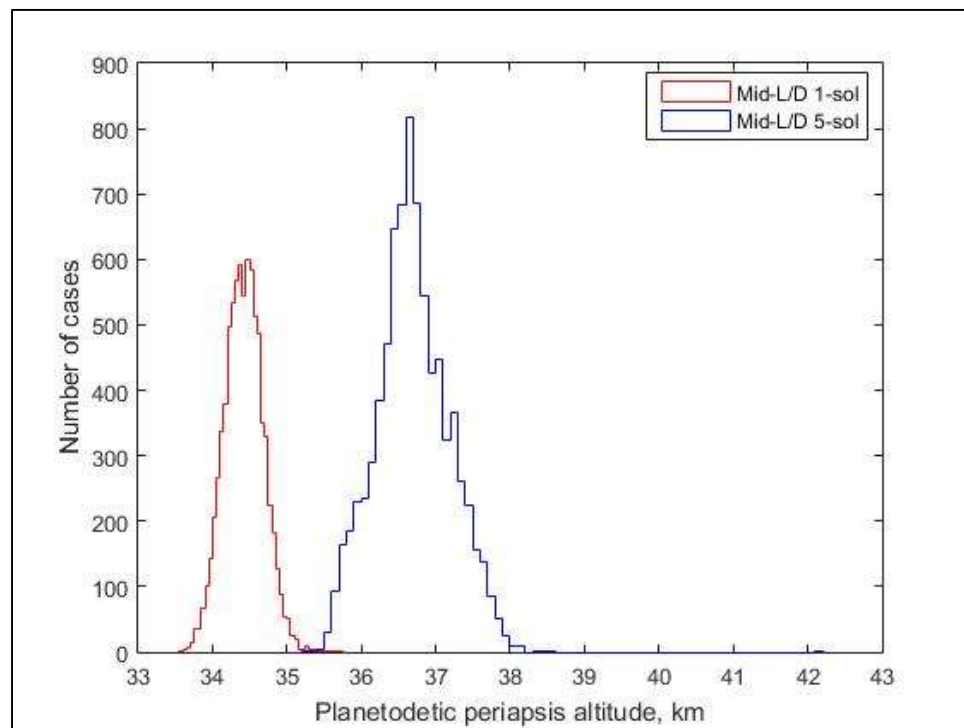
Fig. 5.38. Histogram of ΔV performance, Mid-L/D 1-sol vs. 5-sol target orbit.

The predicted apoapsis altitude at the atmospheric exit interface is shown in Table 5.15 and Fig. 5.39. Here, the 1-sol and 5-sol cases both show improvement over the HIAD 1-sol and 5-sol trajectories in terms of 99th percentile apoapsis error. The maximum apoapsis error for the 5-sol Mid-L/D vehicle is even more improved than the maximum 5-sol HIAD case. Once again, the low cost of conducting the periapsis raise burn at a higher apoapsis allows the worst 5-sol case to perform better than the worst 1-sol case, despite having a larger apoapsis altitude error.

Table 5.15. Mid-L/D predicted apoapsis altitude (km) at exit, 1-sol vs. 5-sol target orbit.

	Mid-L/D 1-sol	Mid-L/D 5-sol
Mean	34203.79	115341.07
3-sigma	3345.48	26739.71
Min	31364.96	70862.87
5.00-percentile	32757.63	103616.80
50.00-percentile	33925.40	113266.08
95.00-percentile	36230.74	131674.50
99.00-percentile	36784.14	137599.44
Max	43492.16	149208.86
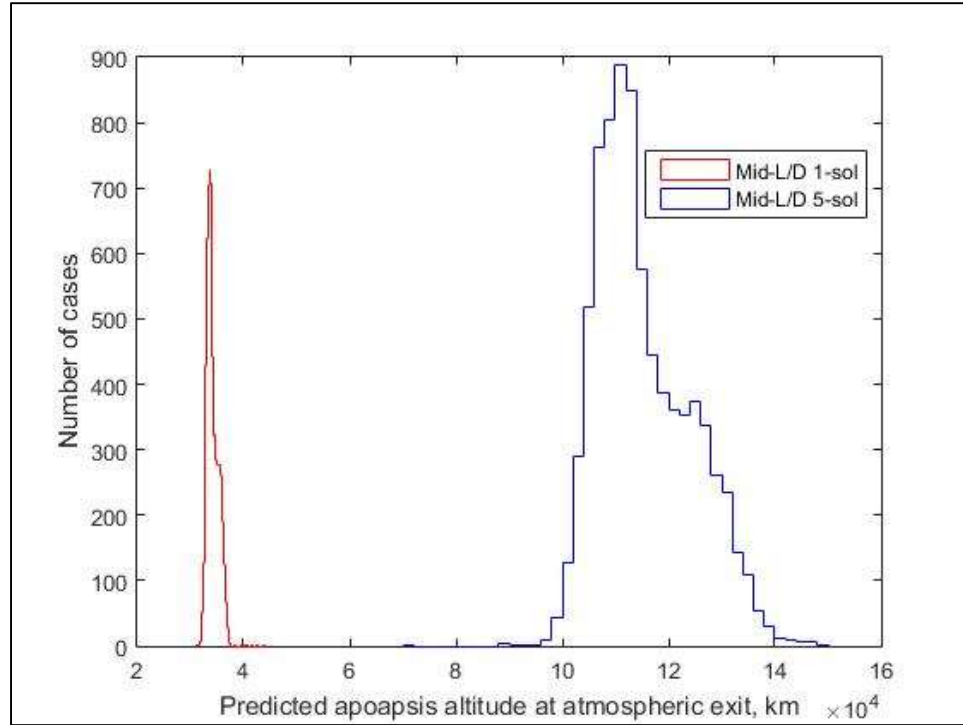
Fig. 5.39. Histogram of predicted apoapsis altitude, Mid-L/D 1-sol vs. 5-sol target orbit.

The last variable to be discussed in this section is the predicted periapsis altitude at atmospheric exit, the data for which is located in Table 5.16 and Fig. 5.40. The predicted periapsis altitudes for the 1-sol and 5-sol test cases are similar as well, but they are markedly lower than the ADEPT or HIAD values. This suggests that the cost to raise the periapsis altitude to the desired 250 km mark will be higher.

Table 5.16. Mid-L/D predicted periapsis altitude (km) at exit, 1-sol vs. 5-sol target orbit.

	Mid-L/D 1-sol	Mid-L/D 5-sol
Mean	11.47	14.75
3-sigma	16.80	13.25
Min	-3.71	1.22
5.00-percentile	2.54	7.42
50.00-percentile	12.02	14.83
95.00-percentile	18.87	21.48
99.00-percentile	20.21	22.43
Max	30.33	30.50
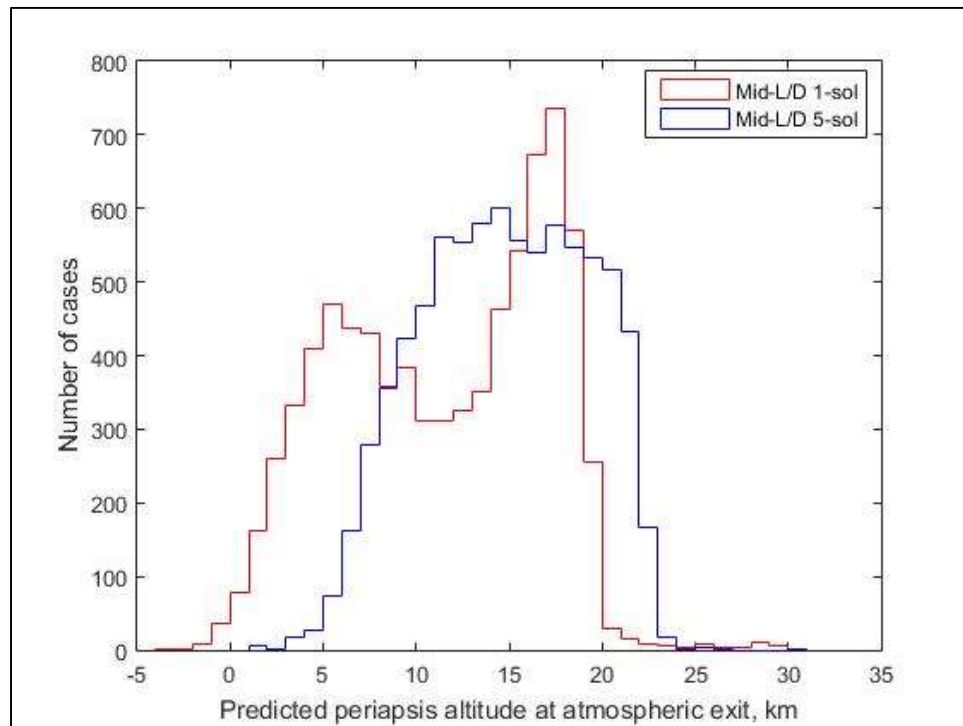
Fig. 5.40. Histogram of predicted periapsis altitude, Mid-L/D 1-sol vs. 5-sol target orbit.

5.4 Overall Algorithm Performance

While it may be helpful to delve deeper into the data to determine the reasons behind differences in algorithm performance, an equally effective approach is to break down the main figure of merit, in this case the 99th percentile total ΔV budget, into its components. This value is a summation of three individual burns: a periapsis raise burn performed at apoapsis, and apoapsis correction burn performed at the newly raised periapsis, and a wedge angle correction burn performed at the node at the highest altitude, and by extension the lowest velocity. To start, Table 5.17 contains the overall ΔV cost for each vehicle using a 1-sol target orbit. In theory, a vehicle with a higher lift-to-drag ratio should exhibit better performance in terms of ΔV minimization. If this is the case, why does the Mid-L/D vehicle have the highest propellant cost?

Table 5.17. Total 1-sol propellant cost (m/s).

	ADEPT	HIAD	Mid-L/D
Mean	21.21	20.47	24.88
3-sigma	9.32	10.77	10.12
Min	14.16	13.28	16.58
5.00-percentile	17.09	15.86	20.21
50.00-percentile	20.67	19.91	24.53
95.00-percentile	26.98	27.10	30.74
99.00-percentile	29.91	30.62	33.57
Max	36.50	45.26	57.29

The answer to this question lies in the data for the individual burns. Table 5.18 contains the data for the periapsis raise burn for each vehicle. The Mid-L/D vehicle has a slightly higher propellant cost here, mostly due to its increased mass.

Table 5.18. Periapsis raise burn propellant cost (m/s), 1-sol orbit.

	ADEPT	**HIAD**	**Mid-L/D**
Mean	12.66	12.60	13.62
3-sigma	1.08	1.12	1.90
Min	11.52	10.86	10.29
5.00-percentile	12.06	11.98	12.66
50.00-percentile	12.68	12.62	13.64
95.00-percentile	13.20	13.17	14.54
99.00-percentile	13.35	13.37	14.73
Max	13.64	13.80	15.03

Next, we will look at the data for the apoapsis correction burn conducted for each vehicle, as shown in Table 5.19. Note that this is the absolute value of the apoapsis correction burn, as the actual value may be negative if the vehicle misses the target on the high side. Again, except for the outliers, these values are very close.

Table 5.19. Apoapsis correction burn propellant cost (m/s), 1-sol orbit.

	ADEPT	HIAD	Mid-L/D
Mean	4.37	4.84	4.96
3-sigma	8.89	10.40	10.08
Min	0.00	0.00	0.00
5.00-percentile	0.43	0.43	0.54
50.00-percentile	3.94	4.26	4.48
95.00-percentile	9.91	11.27	10.96
99.00-percentile	12.74	14.84	13.90
Max	18.62	28.80	42.55

Finally, we will examine the wedge angle correction burn data, as seen in Table 5.20. Clearly, this is where the main discrepancy in the total ΔV budget originates. Although the vehicle with the highest lift-to-drag ratio should be able to have the best response to dispersions in the longitudinal direction, it appears to be the worst performer in terms of crossrange dispersion management. This makes sense intuitively, since a higher lift-to-drag ratio will cause a larger acceleration in the presence of a dispersion.

Table 5.20. Wedge angle correction burn propellant cost (m/s), 1-sol orbit.

	ADEPT	**HIAD**	**Mid-L/D**
Mean	4.19	3.03	6.29
3-sigma	3.05	2.58	3.05
Min	0.56	0.20	2.10
5.00-percentile	2.55	1.71	5.05
50.00-percentile	4.17	2.96	6.17
95.00-percentile	5.87	4.54	8.00
99.00-percentile	6.42	5.12	9.76
Max	8.19	6.66	14.01

A similar trend may be seen in the results from the cases run with a 5-sol final target orbit. Data for the 99th percentile total ΔV budget are presented in Table 5.21 below. Just like 1-sol total propellant costs, the ADEPT vehicle displays superior performance in terms of 99th percentile ΔV minimization, in part because it has the smallest mass. It appears that this lower mass, combined with a slightly higher lift-to-drag ratio than the HIAD, gives the ADEPT vehicle a slight edge.

Table 5.21. Total 5-sol propellant cost (m/s).

	ADEPT	HIAD	Mid-L/D
Mean	12.07	10.87	14.80
3-sigma	9.86	11.79	13.41
Min	5.82	4.39	5.09
5.00-percentile	7.61	5.93	7.62
50.00-percentile	11.67	10.07	14.91
95.00-percentile	17.87	18.32	22.00
99.00-percentile	21.12	22.77	24.82
Max	43.07	36.81	54.05

We can look deeper into the individual burns for the 5-sol target orbit to try and find the reasons behind these performance differences. The periapsis raise burn propellant requirements for each of the tested vehicles can be seen in Table 5.22. These values are all extremely close in magnitude. This is because the periapsis raise burn is performed at such a high altitude that the ΔV cost is quite small, so differences due to post-exit apoapsis altitude are essentially negligible.

Table 5.22. 5-sol periapsis raise burn propellant cost (m/s).

	ADEPT	HIAD	Mid-L/D
Mean	4.38	4.38	4.63
3-sigma	1.11	0.99	1.17
Min	2.30	2.17	3.51
5.00-percentile	3.75	3.81	3.99
50.00-percentile	4.42	4.42	4.67
95.00-percentile	4.94	4.86	5.21
99.00-percentile	5.17	5.06	5.39
Max	5.70	5.51	7.38

Next, we will examine the data for the apoapsis correction burn for each of the 5-sol target cases. These results are shown in Table 5.23. It is clear that the majority of the total propellant cost for the 5-sol orbit comes from this burn. This backs up the earlier assertion that small errors in the exit condition can cause large errors in terms of reaching the 5-sol target apoapsis. Additionally, the Mid-L/D vehicle displays superior performance when looking at the 99th percentile ΔV cost, which is due to its higher lift-to-drag ratio allowing for better response to trajectory dispersions.

Table 5.23. 5-sol apoapsis correction burn propellant cost (m/s).

	ADEPT	HIAD	Mid-L/D
Mean	4.39	5.09	4.41
3-sigma	9.12	11.35	8.65
Min	0.00	0.00	0.00
5.00-percentile	0.42	0.44	0.48
50.00-percentile	3.93	4.35	4.05
95.00-percentile	9.74	12.09	9.39
99.00-percentile	12.81	16.61	11.68
Max	35.61	32.27	42.64

The last variable to inspect is the wedge angle correction burn cost, shown below in Table 5.24. These data seem to back up the suggestion from the 1-sol data that the higher lift-to-drag vehicles tend to display worse performance in terms of lateral errors. However, despite these effects, the algorithm still displays superior performance against existing aerocapture algorithms, and exceptional performance compared to traditional fully-propulsive maneuvers.

Table 5.24. 5-sol wedge angle correction burn propellant cost (m/s).

	ADEPT	HIAD	Mid-L/D
Mean	3.30	1.39	5.75
3-sigma	3.26	2.20	10.21
Min	0.18	0.00	0.02
5.00-percentile	1.65	0.47	0.71
50.00-percentile	3.23	1.23	6.29
95.00-percentile	5.16	2.89	10.21
99.00-percentile	5.82	3.44	11.70
Max	7.98	4.83	17.85

5.5 NPC Guidance Comparison

Although full results of the NPC algorithm performance were not available at the time this thesis was written, an older set of Monte Carlo runs was conducted for the 1-sol and 5-sol target orbits using the ADEPT vehicle. However, unlike the results presented above, these simulations did not include a uniform dispersion on the *dusttau* variable discussed earlier, and were run using an earlier initial date of November 3, 2010. To provide a basis of comparison, two Monte Carlo simulations were run using the FNPAG algorithm and the same initial conditions, target orbits, and dispersions.

Because of the limited availability of the NPC data, the only results compared in this section are the total propellant cost statistics for each target orbit. However, because this was the main figure of merit for the aerocapture flyoff, the results still give insight onto

the advantages enjoyed by the FNPAG algorithm over traditional numerical predictor-corrector approaches. Table 5.25 contains the overall ΔV cost for each algorithm using a 1-sol target orbit and the ADEPT vehicle. Clearly, FNPAG displays a significant improvement over NPC guidance in terms of total ΔV requirements, with a 56% reduction in mean propellant required and a 50% reduction in the 99th percentile ΔV budget. This advantage is due to the use of a bang-bang bank angle magnitude profile instead of the constant profile prescribed by other state-of-the-art predictor-corrector approaches in use today.

Table 5.25. Total 1-sol propellant cost (m/s), FNPAG vs. NPC guidance.

	FNPAG	NPC
Mean	18.60	42.79
3-sigma	4.39	3.82
Min	15.67	36.54
5.00-percentile	16.72	40.64
50.00-percentile	18.33	42.84
95.00-percentile	21.34	44.71
99.00-percentile	23.04	45.64
Max	27.54	48.26

The results for the 5-sol target orbit display a pattern similar to the data from the 1-sol target orbit, as seen in Table 5.26. Although both of the algorithms perform better in the 5-sol case than the 1-sol case due to the nature of the target orbits, the FNPAG algorithm still enjoys a 42% reduction in mean ΔV requirement and a 21% reduction in the 99th

percentile ΔV budget compared to the NPC guidance approach. Clearly, the foundation of the FNPAG algorithm in optimal control theory provides significant benefits is terms of propellant cost reduction.

Table 5.26. Total 5-sol propellant cost (m/s), FNPAG vs. NPC guidance.

	FNPAG	NPC
Mean	8.29	14.38
3-sigma	4.70	2.87
Min	5.67	12.44
5.00-percentile	6.29	12.91
50.00-percentile	8.07	14.29
95.00-percentile	11.21	16.11
99.00-percentile	13.46	17.05
Max	19.39	18.63

CHAPTER 6. CONCLUSIONS

This thesis has explored the feasibility of the Fully Numerical Predictor-Corrector Aerocapture Guidance algorithm for use in conducting trade studies of a Mars aerocapture mission with multiple vehicle models and post-atmospheric-exit target orbits. A review of past and present aerocapture algorithm was conducted, the formulation of the algorithm was explored, and the simulation environment and vehicle characteristics were identified. This algorithm is the first to solve the optimal aerocapture guidance problem based directly on the optimal control theory. A rigorous set of testing has been completed, demonstrating the algorithm's superior performance and robustness over two existing state-of-the-art aerocapture algorithms.

In addition to offering the best performance in terms of post exit propellant consumption minimization, the FNPAG algorithm also enjoys a relative lack of tuning required to obtain satisfactory results. Because of its unique formulation, FNPAG can be tuned for any mission scenario and vehicle model quickly and easily, as evidenced by its completion of the entire suite of test cases for the aerocapture guidance flyoff, an accomplishment achieved by none of the other algorithms. The algorithm shows great promise for use in future missions to Mars and beyond.

REFERENCES

[1] Lu, Ping. "Entry Guidance: A Unified Method," *Journal of Guidance, Control, and Dynamics*, Vol. 37, No. 3, 2014.

[2] Hall, J. L., Noca, M. A., and Bailey, R. W., "Cost-Benefit Analysis of the Aerocapture Mission Set," *Journal of Spacecraft and Rockets*, Vol. 42, No.2, 2005, pp. 309-320.

[3] Dwyer Cianciolo, Alicia. "EDL Architecture Study: Technical Interchange Meeting Introduction," NASA Langley Research Center, Hampton, VA, April 2016.

[4] Walberg, G.D., "A Survey of Aeroassisted Orbital Transfer," *Journal of Spacecraft and Rockets*, Vol. 22, No.1, 1985, pp. 3-18.

[5] Mease, K.D., "Optimization of Aeroassited Orbital Transfer: Current Status," *Journal of Optimization Theory and Applications*, Vol. 36, Nos. 1-2, 1988, pp. 7-33.

[6] Hill, O., "An Adaptive Guidance Logic for an Aeroassisted Orbital Transfer Vehicle," *AAS/AIAA Astrodynamics Special Conference*, AAS Paper 1983-357, Aug. 1983.

[7] Moseley, P.E., "The Apollo Entry Guidance: A Review of the Mathematical Development and Its Operational Characteristics," TRW, Note 69-FMT-791, Houston, TX, Dec. 1969.

[8] Cerimele, C.J., and Gamble, J.D., "A Simplified Guidance Algorithm for Lifting Aeroassist Orbital Transfer Vehicles," AIAA Paper 1985-0348, Jan. 1985.

[9] Masciarelli, J. P., and Queen, E. M., "Guidance Algorithms for Aerocapture at Titan," AIAA Paper 2003-4822, July 2003.

[10] Bryant, L. E., Tigges, M. A., and Ives, D. G., "Analytical Drag Control for Precision Landing and Aerocapture," AIAA Paper 1998-4572, Aug. 1998.

[11] Casoliva, J., Lyons, D. T., Wolf, A. A., and Mease, K. D., "Robust Guidance via a Predictor-Corrector Algorithm with Drag Tracking for Aero-Gravity Assist Maneuvers," AIAA Paper 2008-6816, Aug. 2008.

[12] Braun, R. D., and Powell, R. W., "Predictor-Corrector Guidance Algorithm for Use in High-Energy Aerobraking System Studies," *Journal of Guidance, Control, and Dynamics*, Vol. 15, No. 3, 1992.

[13] Evans, S. W., and Dukeman, G. A., "Examination of a Practical Aerobraking Guidance Algorithm," *Journal of Guidance, Control, and Dynamics*, Vol. 18, No. 3, 1995, pp. 471-477.

[14] Jits, R. Y., and Walberg, G. D., "Blended Control, Predictor-Corrector Guidance Algorithm: an Enabling Technology for Mars Aerocapture," *Acta Astronautica*, Vol. 54, No. 6, 2004, pp. 385-398.

[15] Putnam, Z. R., Bairstow, S. H., Braun, R. D., and Barton, G. H., "Improving Lunar Return Entry Range Capability Using Enhanced Skip Trajectory Guidance," *Journal of Spacecraft and Rockets*, Vol. 45, No. 2, 2008, pp. 309-315.

[16] Lafleur, J. M., "The Conditional Equivalence of ΔV Minimization and Apoapsis Targeting in Numerical Predictor-Corrector Aerocapture Guidance," NASA TM-2011-216156, Johnson Space Center, Houston, TX, Aug. 2011.

[17] O'Connor, B., and Korsmeyer, D., "A Control Methodology for Low-Thrust Orbital Transfers," AIAA Paper 90-2959, 1990.

[18] Justus, C. G., Duvall, A. L., and Keller, V. W., "Atmospheric Models for Aerocapture," AIAA Paper 2004-3844, Jul. 2004.

[19] Justh, H.L., "Mars Global Reference Atmospheric Model 2010 Version: Users Guide," NASA TM-2014-217499, Marshall Space Flight Center, Huntsville, AL, 2014.

[20] Hourdin, F., Le Van, P., Forget, F., and Talagrand, O., "Meteorological Variability and the Annual Surface Pressure Cycle on Mars," *Journal of Atmospheric Sciences*, Vol. 50, pp. 3625-3640, 1993.

[21] Pontryagin, L. S., Boltyanskii, V. G., Gramkreledze, Q. V., and Mishchenko, E.F., *The Mathematical Theory of Optimal Processes*, Intersciences, New York, 1962, Chap. 2.

[22] Lu, P., "Entry Guidance: A Unified Method," *Journal of Guidance, Control, and Dynamics*, Vol. 37, No. 3, 2014, pp. 713-728.

[23] Brent, R.P., *Algorithms for Minimization Without Derivatives*, Prentice-Hall, Englewood Cliffs, NJ, 1973, Chaps. 4 and 5.

[24] Brunner, C., and Lu, P., "Skip Entry Trajectory Planning and Guidance," *Journal of Guidance, Control, and Dynamics*, Vol. 31, No. 5, 2008, pp. 1210-1219.

[25] Brunner, C., and Lu, P., "Comparison of Fully Numerical Predictor-Corrector and Apollo Skip Entry Guidance Algorithms," *Journal of the Astronautical Sciences*, Vol. 59, No. 3, 2012, pp. 517-540.

[26] Smith, K., "Predictive Lateral Logic for Numerical Entry Guidance Algorithms," AAS Paper 2016-1182, Feb. 2016.

[27] Ro, T. U., and Queen, E. M., "Study of Martian Aerocapture Terminal Point Guidance," AIAA Paper 98-4571, Aug. 1998.

[28] Powell, R. W., "Numerical Roll Reversal Predictor-Corrector Aerocapture and Precision Landing Guidance Algorithms for the Mars Surveyor Program 2001 Missions," AIAA Paper 98-4574, Aug. 1998.

[29] Striepe, S. "Program to Optimize Simulated Trajectories II," Mar. 2016. Retrieved from http://post2.larc.nasa.gov/index.html.

[30] Way, D. W., Powell, R. W., Chen, A., Steltzner, A. D., Martin, A. M. S., Burkhart, P. D., and Mendeck, G. F., "Mars Science Laboratory: Entry, Descent, and Landing System Performance," IEEE Paper 1095-323X, Mar. 2006.